CENTRO INTERNACIONAL DE ESTUDOS
DE DOUTORAMENTO E AVANZADOS
DA USC (CIEDUS)

Tese de Doutoramento

Development of antenna arrays for terrestrial and satellite applications: Feasibility study of different solutions to monitoring the atmospheric pollution, determination of electromagnetic fields in urban scenarios and calculation of their dosimetry in small animals.

Aarón Ángel Salas Sánchez

ESCOLA DE DOUTORAMENTO INTERNACIONAL

PROGRAMA DE DOUTORAMENTO EN MÉTODOS MATEMÁTICOS E SIMULACIÓN NUMÉRICA EN ENXEÑARÍA E CIENCIAS APLICADAS

SANTIAGO DE COMPOSTELA

2017

USC
UNIVERSIDADE
DE SANTIAGO
DE COMPOSTELA

CENTRO INTERNACIONAL DE ESTUDOS DE DOUTORAMENTO E AVANZADOS DA USC (CIEDUS)

Declaración do autor da Tese

D. Aarón Ángel Salas Sánchez

Presento miña tese, seguindo o procedemento adecuado ao Regulamento, e declaro que:

1. A tese abarca os resultados da elaboración do meu traballo.
2. No seu caso, na tese se fai referencia as colaboracións que tivo este traballo.
3. A tese é a versión definitiva presentada para a súa defensa e coincide ca versión enviada en formato electrónico.
4. Confirmo que a tese non incorre en ningún tipo de plaxio de outros autores nin de traballos presentados por min para a obtención de outros títulos.

En Santiago de Compostela, 10 de outubro de 2017

Aarón Ángel Salas Sánchez

USC
UNIVERSIDADE
DE SANTIAGO
DE COMPOSTELA

CENTRO INTERNACIONAL DE ESTUDOS DE DOUTORAMENTO E AVANZADOS DA USC (CIEDUS)

Francisco José Ares Pena, Catedrático de Electromagnetismo do Departamento de Física Aplicada da Universidade de Santiago de Compostela,

Juan Antonio Rodríguez González, Profesor Titular de Universidade do Departamento de Física Aplicada da Universidade de Santiago de Compostela,

INFORMAN:

Que a presente tese, titulada **Development of antenna arrays for terrestrial and satellite applications: Feasibility study of different solutions to monitoring the atmospheric pollution, determination of electromagnetic fields in urban scenarios and calculation of their dosimetry in small animals** correspóndese co traballo realizado por

Aarón Ángel Salas Sánchez

baixo a miña dirección, e autorizo a súa presentación, considerando que reúne os requisitos esixidos no Regulamento de Estudos de Doutoramento da USC, e que como director desta non incorre nas causas de abstención establecidas na Lei 40/2015.

E para que así conste, asinan en Santiago de Compostela, a 10 de outubro de 2017.

Francisco José Ares Pena

Juan Antonio Rodríguez González

V. e pr.

M. Pilar Salgado Rodríguez
En calidade de titora do programa de doutoramento

USC
UNIVERSIDADE
DE SANTIAGO
DE COMPOSTELA

Agradecimientos

Quiero expresar mi más sincero agradecimiento a todas las personas que han hecho posible, tanto directa como indirectamente, la realización de esta Tesis Doctoral:

- A *Francisco José Ares Pena*, por todo el tiempo invertido en el trabajo aquí desarrollado, prestándome su apoyo, sus consejos, sus mejores ideas y su comprensión.
- A *Juan Antonio Rodríguez González*, por su inestimable ayuda. Sin él esta tesis no hubiera sido posible. Por sus acertados comentarios para mejorar mi trabajo y por tener siempre un hueco para hablar.
- A la profesora *Elena López Martín*, por ofrecerme la oportunidad de participar en sus investigaciones sobre efectos biológicos de la radiación no ionizante, por sus amables palabras y sus consejos.
- A todos los que han ido formando a mi lado el Grupo de Sistemas Radiantes: *Quela, Javi, Rogelio y Pablo*.
- Al grandísimo *Eduardo Moreno*, al que le profeso un cariño especial desde que me dio Electromagnetismo cuando estudiaba la carrera.
- Al Ministerio de Economía y Competitividad, por financiar este trabajo a través del proyecto TEC2011-24441, mediante una ayuda de Formación de Personal Investigador (FPI) con referencia BES-2012-052627.
- A mis padres *Isabel* y *Ángel*, por enseñarme día a día que en la vida rendirse no es una opción y demostrarme que con el amor de una familia todo se puede conseguir.
- A mi hermana *Ana*: Es un orgullo ser tu hermano, por lo luchadora que eres y por el cariño que me das siempre que lo necesito. En una frase no puedo plasmar todo lo que supones para mi, te adoro.
- A *María González*, por ser como eres, por tu cariño y por tu ayuda en los momentos más difíciles. Nunca podremos agradecer lo suficiente lo que haces por nosotros.
- A *Carlos Vázquez*, porque aquí, en la Física, has sido siempre mi gran apoyo. Desde que te conocí rompiste mis esquemas mentales y siempre (a tu manera) has estado ahí. Nos hemos metido en mil líos y he vivido experiencias que jamás hubiera imaginado, solo por haber compartido espacio-tiempo contigo. Sabes que no comulgo con algunas de tus tesis vitales, aunque en otros casos me has hecho ver lo prejuicioso que puedo llegar a ser y has cambiado mi manera de pensar. Gracias.
- A muchísima gente que está y/o ha estado en la Facultad de Física acompañándome en todo esto siempre interesándose porque esto llegara a buen puerto: *Pepi, Javier Castro, Rafa Fuentes, Charly, Dani, Darío, Sergio, Alba, Cotelo, Diego, Alexis, Manoel, Xavi, Vicente, Pablo Fernández, Pablo Díaz, Sabela, Conchi, Isa, Olga, ...*

- A *Chus y a los BIO VIPS (María, Tomás, Alba y Adrián)*, porque en esta última etapa de mi doctorado ha sido un verdadero placer encontrarme con vosotros, chicos, gracias por dejarme formar parte de vuestra pequeña locura.

- A *David, Pancho, Luis y Sara* por hacerme la vida más agradable en el 215 mientras hacíais vuestros Trabajos Fin de Grado.

- Y finalmente, a vosotros, chiquillos de Electro I! El último par de años de mi doctorado lo habéis llenado de gratos momentos. Ha sido toda una experiencia para mi que no cambiaría por nada. Vuestras sonrisas cuando me saludáis al encontrarnos, tanto en la Facultad como fuera de ella, o saber que os he podido ayudar en algún momento puntual ya hace que haya valido la pena. Os deseo a todos lo mejor, sé que muchos lo conseguiréis. Salud y Rock and Roll!

Acknowledgements

- I would like to thank professor *Giorgio Franceschetti* his support during my stay in Naples and his very interesting talks. It was a really honour for me to discover who is the person behind the scientific prestige.

- Also I would like to express my deep gratitude to professor *Antonio Iodice* for his assistance and his wonderful kindness. My experience in Naples was so amazing in part for his good guidance, help and support. Thank you very much.

- To *Davod*: for your willingness to help me always. Thank you! :)

- To all the people of the *Dipartimento di Ingegneria Elettrica e Tecnologie dell'Informazione* at University Federico II of Naples, specially to *Gerardo, Donato, Giuseppe, Danielle, Stefano, Roberto, Frankie, Veronica and Alessio*. It was a pleasure to meet all of you, I really appreciate our talks and our coffee time.

- To *Anna*: I will never forget our measurements along the city in your car, our time in Pozzuoli or the party after your graduation, thank you.

- To *Farzin*: It was an amazing experience to meet you and you know it. I remember our walks for Mergellina and our conversations. Thank you very much for your friendship.

Limiar

O presente traballo constará de varias partes diferenciadas, que poden resumirse do seguinte xeito: En primeiro lugar, levaranse a cabo diferentes estudos teóricos e numéricos para a mellor das prestacións de agrupacións de antenas que presentan unha alimentación uniforme. Deseguido mostrarase o proceso de deseño de varias antenas conformadas das calse se plantexa a súa inclusión no medio urbano. A continuación, os deseños antes mostrados serán obxecto de diferentes tests gracias á construcción de prototipos e a súa verificación mediante medidas experimentais no laboratorio. Por outra banda, levarase a cabo un estudo sobre a caracterización do comportamento electromagnético en termos de circuitos planos equivalentes. Ademáis diso, e por último, levarase a cabo unha evaluación da influenza electromagnética recíproca de diferentes obxectos que compoñen o escenario urbano: antenas de transmisión e de recepción, sensores, presenza humana, etc.

USC
UNIVERSIDADE
DE SANTIAGO
DE COMPOSTELA

Prólogo

El presente trabajo constará de varias partes diferenciadas, que pueden ser resumidas de la siguiente manera: En primer lugar se llevarán a cabo diferentes estudios teóricos y numéricos para la mejora de prestaciones de agrupaciones de antenas que presenten alimentación uniforme. Seguidamente se mostrará el proceso de diseño de diferentes antenas para ser integrables dentro del entorno urbano. A continuación, estos diseños serán testeados gracias a la construcción de diferentes prototipos y su posterior verificación experimental en laboratorio. Por otro lado, se llevará a cabo un estudio sobre la caracterización del comportamiento electromagnético de las zonas urbanas en términos de circuitos planos equivalentes. Además de ello, y por último, se evaluará la influencia electromagnética recíproca entre objetos presentes en el escenario urbano: antenas de transmisión y de recepción, sensores, presencia humana, etc.

USC
UNIVERSIDADE
DE SANTIAGO
DE COMPOSTELA

Abstract

The present work will have several differenciated parts which can be summarized as it follows: First of all, it will be held different theoretical and numerical studies to improve the performance of antenna arrays that present uniform feed. Then, the design process of different conformal antennas is shown, in order to be integrated within the urban environment. Some of these designs will be tested by building different prototypes with their subsequent laboratory experimental verification. On the other hand, it will conduct a study on the characterization of the electromagnetic behaviour of urban areas in terms of equivalent planar circuits. Moreover and lastly, mutual electromagnetic influence between objects present on the urban scene will be evaluated: trasmission and reception antennas, sensors, human presence, etc.

USC
UNIVERSIDADE
DE SANTIAGO
DE COMPOSTELA

Contents

USC
UNIVERSIDADE
DE SANTIAGO
DE COMPOSTELA

1 Introduction

1.1 Antenna arrays

Nowadays, in satellite communications and radar applications antennas formed by identical radiating elements are used. These elements can be of different types: horns, patches, dipoles, slots, etc. The antennas above mentioned, that are built by two or more elements, are usually known as antenna arrays.

The antenna arrays offer a lot of advantages in front of one element antennas. As they can have a larger size, they can afford a more directive radiation pattern. Also they permit to control the excitation and/or position of each element, in order to produce a desired radiation pattern.

The mathematical model of the radiation of an antenna is notably complex. Even only considering a simply element, a detailed evaluation of different parameters related with its associated electromagnetic field is necessary. By other hand, in the analysis of the array it is also necessary to include the interactions between each element.

Fortunately the array theory offers the tool that permits to develop the main part of the design and synthesis of the arrays without developing the exact electromagnetic models for each element. It will be demonstrated that for an array with identical elements and uniformly oriented, it is possible to calculate the radiation pattern as the product of two quantities, the element factor and the array factor. The element factor is the field produced by one of the array elements and, therefore, it only depends on the electromagnetic characteristics of the radiating element chosen. By other hand, the array factor is independent of the type of radiating element considered and it is determined by the geometrical configuration of the whole array antenna and the amplitude and phase of the excitations.

For the more used radiating element, as they could be dipoles, slots, etc. the element factor corresponds with a directional radiation pattern that exhibits a quite large bandwidth due to the fact that these elements present a low size ($l_{max} = \lambda/2$).

Usually the element factor is not considered in the synthesis procedure due to the fact that the characteristics of the radiation pattern are mainly determined by the array factor. For this approximation the array corresponds with a distribution of isotropic radiating elements.

1.1.1 The array factor

In Fig. 1 a sketch of the distribution of the array elements is shown. Each element radiates a directional pattern that presents a radial and an angular dependence near the element.

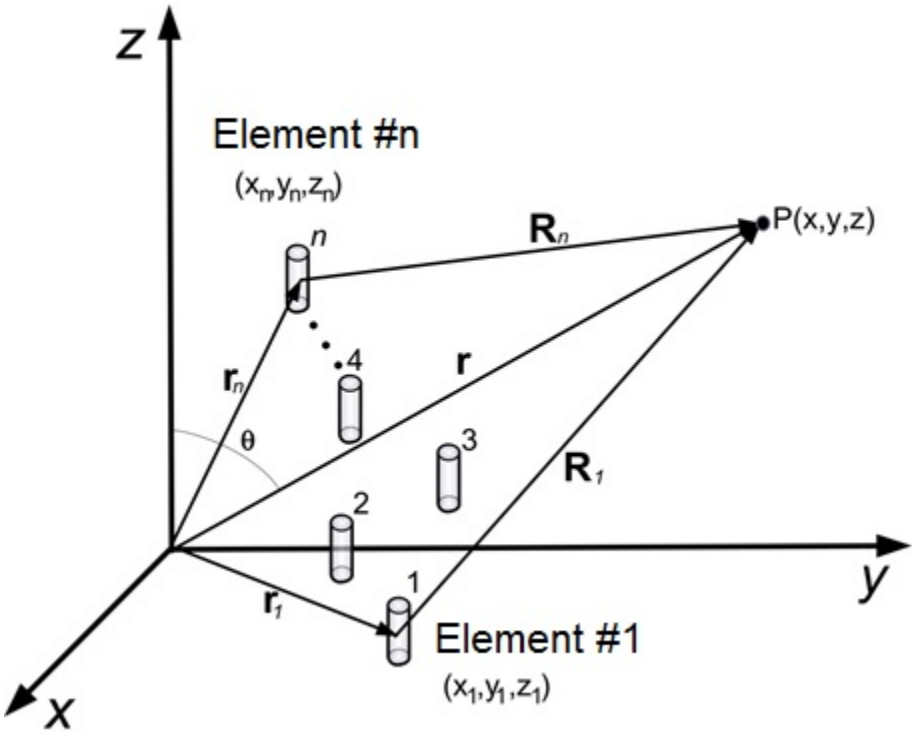

Figure 1: Sketch of the arrangement of a general array.

However, for great distances, the radiation pattern of the element can be expressed as the product of a spherical wave function e^{-jkR}/R and a vectorial function that depends on the angle $f_n(\theta, \phi)$ known as element pattern or element factor. Although this function depends on the type of element that is used, the far field of a n-th element of the array can be expressed as:

$$E_n(R, \theta, \phi) = f_n(\theta, \phi) \frac{e^{-jkR_n}}{R_n} \tag{1}$$

where

$$R_n = [(x - x_n)^2 + (y - y_n)^2 + (z - z_n)^2]^{1/2} \tag{2}$$

and $k = \frac{2\pi}{\lambda}$ is the wavenumber in the vacuum.

If the radiation pattern is measured at a large distance, the exponential term of (1) can be approximated by the distance between a field point and the center of an arbitrary coordinate system, denoted by (R, θ, ϕ). Following this assumption, it can be written:

$$R_n \approx R - \hat{r} \cdot r_n \tag{3}$$

so

$$\frac{e^{-jkR_n}}{R_n} \approx \frac{e^{-jkR}}{R} e^{jkr_n \cdot \hat{r}} \tag{4}$$

where r_n is the position vector of the n-th element with respect to the center of the chosen coordinate system and $\hat{r}$ is an unitary vector on the direction of the point (R, θ, ϕ). So, these vectors can be denoted by:

$$r_n = x_n\hat{x} + y_n\hat{y} + z_n\hat{z} \tag{5}$$

$$\hat{r} = \sin\theta\cos\phi\hat{x} + \sin\theta\sin\phi\hat{y} + \cos\theta\hat{z} \tag{6}$$

The minimum distance R for a valid approximation depends on the dimensions of the array as well as the desired precision for evaluating the radiation pattern. Therefore, a distance:

$$R = \frac{2D^2}{\lambda} \tag{7}$$

where D is the maximum dimension of the array antenna, is widely used as a criteria for the most part of the cases. However, in patterns with low sidelobes or with regions that present quite deep nulls it is necessary to consider a distance $\geq 10D^2/\lambda$. The radiation pattern of an arbitrary N elements array can be written by using the superposition principle

$$E(r) = \frac{e^{-jkR}}{R} \sum_{n=1}^{N} I_n f_n(\theta, \phi) e^{jkr_n \cdot \hat{r}} \tag{8}$$

This expression is general due to it is determined by using the pattern each element in the presence of the whole array. The coefficients I_n are the weights of the incident signals that are applied to each element and can be given by the voltages or the currents[1], attending to the type of considered element.

In general, the element factor is different for each one of the radiators, even in arrays with similar elements, this difference typically is due to the interaction between the elements near to the edges. However in most of the cases, it results completely valid to assume that all the elements are identical. In this case, the expression (8) is transformed in

$$F(\theta, \phi) = f(\theta, \phi) \frac{e^{-jkR}}{R} \sum_{n=1}^{N} I_n e^{jkr_n \cdot \hat{r}} \tag{9}$$

Due to the fact that the radiation pattern if often represented (or measured) in a sphere of constant radius, the spheric factor is generally neglected. Therefore, the radiation

[1] In this thesis we will work with current excitations.

pattern can be expressed as the product of a vector that is the element pattern $f_n(\theta, \phi)$ and a scalar factor $F(\theta, \phi)$ called array factor:

$$F(\theta, \phi) = \sum_{n=1}^{N} I_n e^{jk_n \cdot \hat{r}} \tag{10}$$

This expression, that is the basis of the radiation pattern synthesis of the antenna arrays, is widely used in linear and planar arrays.

Its using requires the same element pattern from all the radiating elements of the array, that implies that these must be identical and oriented in the same direction. For arrays with different elements or not uniformly oriented (as, for example, the so-called conformal array), it is necessary to consider the element factor in the synthesis procedure by using the expression (8) without the factor e^{-jkR}/R.

1.1.2 Array pattern synthesis

Given an array whose elements are in the positions (x_n, y_n, z_n) the synthesis of radiation patterns consists of computing the set of excitations I_n in order to get the closer radiation pattern $F(\theta, \phi)$ to the desire one as possible, so that it verifies a certain specification imposed at the design stage. It should be noted that not only the shape of the radiation pattern must meet the specification, but also other parameters such as the side lobe level (SLL), the beamwidth of the radiation pattern, the gain, etc.

As will be seen, in the synthesis process, in addition to the radiation diagram, the excitation set obtained is also crucial, since depending on how it is, it can be more or less easy to implement feeding network of the array. Thus, we find some solutions that, although they synthesize radiation patterns that perfectly verify the specifications, are impossible or very expensive to implement. At this respect, it is very important to look for a small variability of the excitations, in order to alleviate the effects derived from the mutual electromagnetic coupling between the different radiating elements, one of the major problems for the designer is to implement a given feeding network. In the synthesis problems, this variability is usually taken into account through the so-called dynamic range $|I_{max}/I_{min}|$, which evaluates the relation between the maximum and minimum excitation amplitudes, or through the parameter $|I_n/I_{n\pm1}|_{max}$, which measures the maximum excitation variability between adjacent elements.

In the most part of this thesis the synthesis of radiation patterns of two-dimensional arrays will be considered.

Linear arrays

Linear arrays represent arrays where the elements are located along a straight line. Without loss of generality, we can suppose an array of $N + 1$ elements distributed along

the z-axis. Since the positions of the elements are given by $(0, 0, z_n)$, the array factor for this case takes the following form:

$$F(\theta) = \sum_{n=0}^{N} I_n e^{jkz_n \cos\theta} \tag{11}$$

where θ is the measured angle from the axis of the array. It should be noted that in linear arrays it is quite common to represent the radiation patterns versus the measured angle from the direction perpendicular to the array, where the zenith of the antenna is. In this case, in expression 11 and subsequent, it is necessary to consider the sine of the angle instead of the cosine.

Returning to the expression of the array factor, we see that it has no dependence on ϕ, presenting rotation symmetry around the axis of the array. In the particular case that all elements are separated by a distance d, then $z_n = nd$ (placing the first element in the origin of coordinates), so that:

$$F(\theta) = \sum_{n=0}^{N} I_n e^{jkd\cos\theta} \tag{12}$$

By substituting in the previous expression the following terms:

$$\psi = kd\cos\theta, \quad w = e^{j\psi} \tag{13}$$

the array factor could be expressed as follows

$$F(\theta) = I_n \sum_{n=0}^{N} (I_n/I_N) w^n = I_N \prod_{n=1}^{N} (w - w_n) \tag{14}$$

It is observed that it has been possible to express the array factor as a polynomial of degree N, whose roots are given by w_n. Therefore, these roots characterize, like the excitations, this array factor.

In the previous literature, Schelkunoff [1] introduced a technique that allows to synthesize radiation patterns by calculating the position of the roots of the polynomial associated with the array factor. For this purpose, he constructed a unit circle in the complex plane, where the variable w is forced to move, also expressing the roots of the array factor of the form $w = e^{a_n + jb_n}$. Thus, a_n and b_n denote, respectively, the angular and radial position of the n-th root in the Schelkunoff circle. It can be shown that the position of the roots determines the radiation pattern of the array. Thus, by varying the relative position of these roots on the unit circle can be characterized 3 different radiation patterns, as suggested in Fig. 2. First, it is observed that if the roots are located on the unit circle (which implies that an $a_n = 0$) and with a given arrangement, we will synthesize a sum or 'pencil' pattern, characterized by a single main lobe, generally of elliptic section, and a family of low level secondary lobes. Since the zeros that appear in

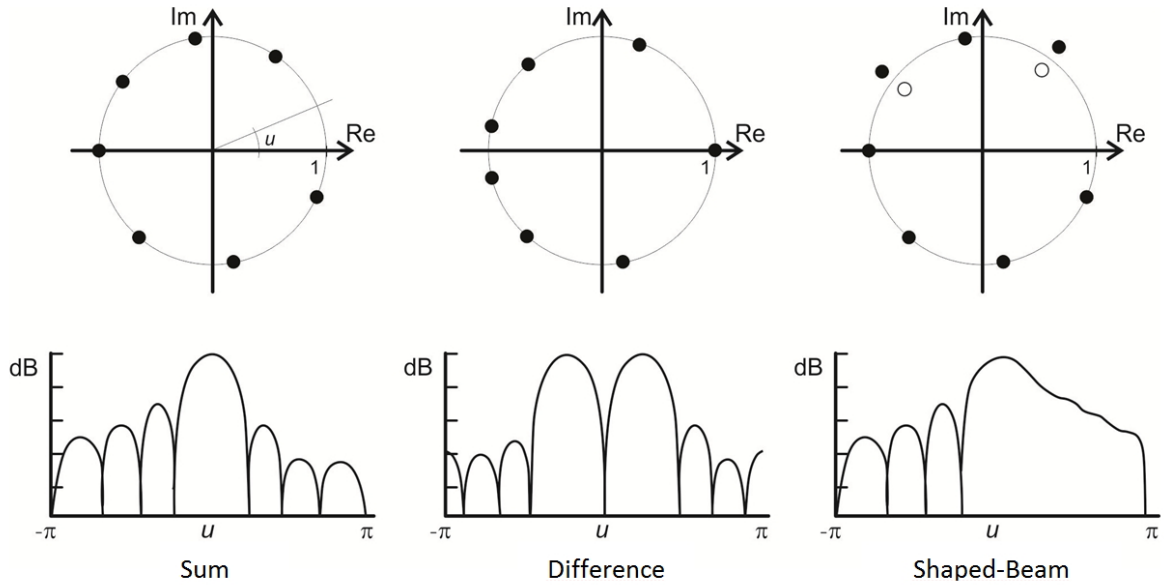

Figure 2: Distribution of zeros over the unit circle for the 3 cases of a linear array of 8 elements.

the radiation patterns are associated with the roots of the polynomial, if we approach or separate roots from others in the unit circle, the side lobes of the diagram will result from a lower or higher level, respectively. This allows us to place the roots so as to obtain a principal lobe and arbitrary lateral lobes in the case of the sum pattern, or two main lobes and arbitrary side lobes for the difference pattern, characterized by a pair of lobes in phase opposition, separated by a single zero, and a family of low level side lobes. Finally, if some of the roots are located outside or inside the unit circle (by doing $a_n \neq 0$) a shaped-beam pattern will be produced, consisting of a radiation pattern with a region of more or less flat filled zeros constituting the emission region and a region of side lobes at a certain level.

In the synthesis of sum patterns, Dolph [2] was the first to introduce an analytical technique to control the level of secondary lobes by using the Chebyshev polynomials. However, the fact that the resulting patterns present all their lateral lobes at the same level causes an extreme edge brightening in the current distributions associated with them, which can lead to difficulties on their physical implementation.

One of the most used and efficient method for the synthesis of radiation patterns for linear arrays with equispaced and identical elements is the method of Orchard-Elliott [3]. This technique iteratively perturb the roots associated with the array factor in order to obtain a radiation pattern with a desired side lobe topography and ripple level. This

method, applicable to the synthesis of sum, difference and shaped-beam patterns, allows a comprehensive control over the topography of the radiation patterns, providing the desired solution in a few seconds.

Subsequently, Kim et al. [4] extended the Orchard-Elliott technique to the synthesis of shaped-beam patterns by using pure real distributions. This was achieved by doubling the number of roots used in filling the zeros of the emission region and grouping them in pairs with respect to the conventional method. Asymmetric shaped-beam patterns were synthesized using a symmetrical aperture distribution in amplitude and antisymmetric in phase, a requirement of arrays with central power supply.

For linear arrays with a large number of elements, it is very common to first synthesize a linear distribution that is subsequently sampled. One of the most widely used solutions is the Taylor distribution [6], which provides sum pattern exhibiting a high gain and a desired level of side lobes.

Subsequently, the Orchard method was extended to the Taylor distributions in order to fill zeros and thus to be able to synthesize also shaped-beam patterns. The discussed techniques allow to synthesize this type of diagrams by using either complex [7] or pure real [8] aperture distributions.

In many of the radar and satellite communication applications, arrays whose elements are distributed on a plane are used. As it will be seen, this allows to have a control over the radiation pattern in the whole space, since the symmetry of rotation associated to the linear arrays disappears.

Suppose we have an array of N elements located in the XY plane at the positions given by (x_n, y_n). Using the expression (10) for this case, it is possible to write the array factor as follows:

$$F(\theta, \phi) = \sum_{n=1}^{N} I_n e^{jk \sin\theta (x_n \cos\phi + y_n \sin\phi)} \tag{15}$$

where I_n is the excitation coefficient of the $n-$th element, which in general will be complex. I_n the expression θ is measured with respect to the Z axis and ϕ is measured in the XY plane from the positive axis X to the positive axis Y.

In this case, the positions of the elements in the array are usually additional design parameters, as well as their amplitudes and phases. However, it is very common to arrange the elements in a rectangular lattice, separated by a distance d_x and d_y in the directions of the axes X and Y respectively, as it is shown in Fig. 3. Assuming that the array consists of $M \times N$ elements, the expression of the array factor would be as follows:

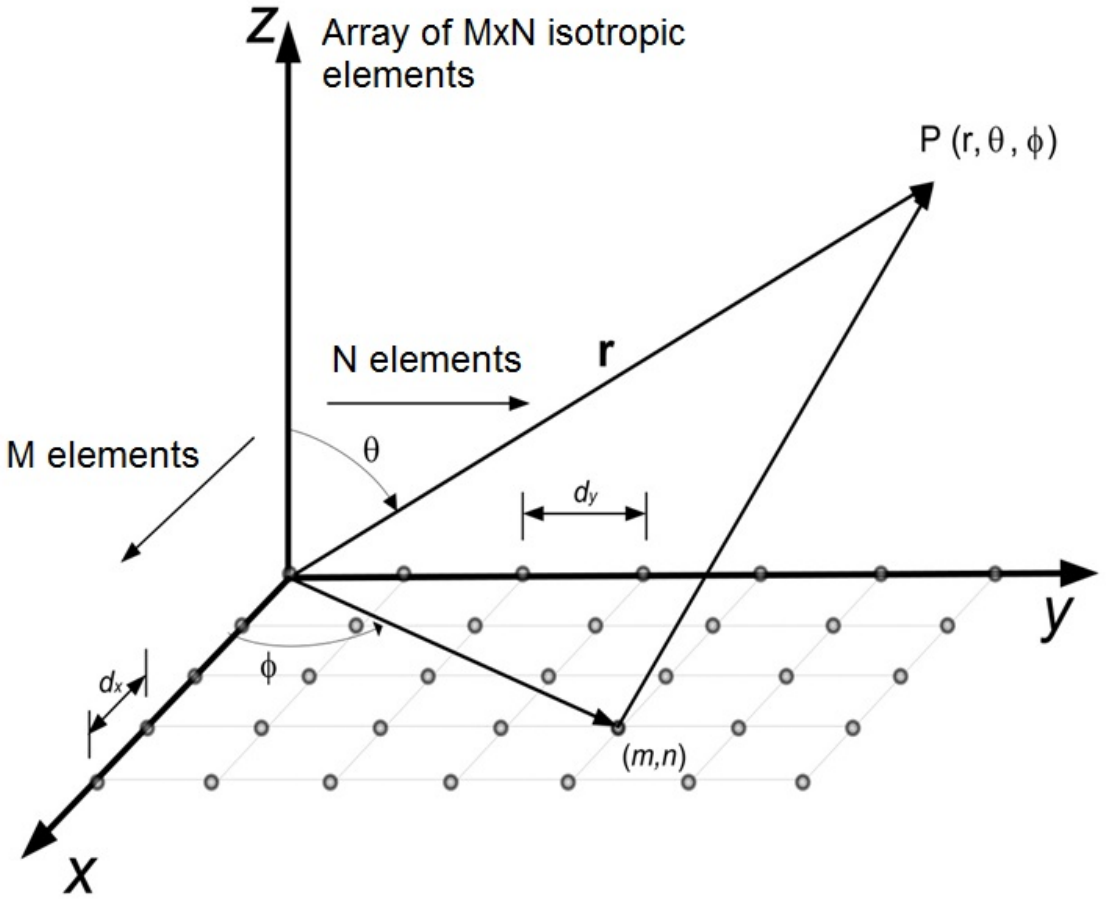

Figure 3: Planar array with rectangular grid.

$$F(\theta,\phi)=\sum_{m=1}^{M}\sum_{n=1}^{N}I_{mn}e^{jk\sin\theta(md_x\cos\phi+nd_y\sin\phi)} \tag{16}$$

where I_{mn} is the relative excitation of the element located in $m-$th row and $n-$th column of the array

One way to synthesize sum patterns of two-dimensional arrays is by using the so-called separable distributions. If each row of elements of an array with rectangular lattice has the same distribution of currents and different levels for the different columns, i.e., if $I_{mn}/I_{m0}=I_{0n}/I_{00}$, the current distribution is called separable and the array factor can be decomposed The following form:

$$F(\theta,\phi)=F_x(\theta,\phi)\cdot F_y(\theta,\phi) \tag{17}$$

in which,

$$F_x(\theta,\phi) = \sum_{m=1}^{M} I_m e^{jkmd_x \sin\theta\cos\phi} \tag{18}$$

$$F_y(\theta,\phi) = \sum_{n=1}^{N} I_n e^{jknd_y \sin\theta\sin\phi} \tag{19}$$

where $I_m = I_{m0}/I_{00}, I_n = I_{0n}/I_{00}$, are the current distributions, normalized to the excitation of the central element, in a row of elements parallel to the X axis and the Y axis respectively.

The expression (17) states that the array factor for an array with rectangular lattice and contour, under the constraint that the aperture is separable, is the product of the array factors corresponding to two linear arrays, one directed along the X axis and another along the Y axis. This allows to synthesize radiation patterns in two-dimensional arrays using most of the techniques developed for linear arrays. Although the use of separable distributions simplifies the implementation of the beam forming network, in the synthesized radiation patterns by this method, the lateral lobes outside the main planes usually have a very low level, which leads to a significant widening of the main beam, with the consequent loss in directivity.

To solve the above problem, it is necessary to use non-separable distributions. Taylor [9] developed a technique that allowed synthesizing sum patterns, with symmetry in and a desired level of lateral lobes, using circular distributions. It is possible to sample such distributions for use in two-dimensional arrays with circular boundaries. However, often it is necessary to use arrays with many elements to obtain satisfactory results.

Later, Elliott and Stern applied the method of Orchard to the circular Taylor distributions, filling nulls in the radiation diagrams and thus to be able to synthesize profiled beam diagrams. The method allowed to synthesize diagrams with circular or elliptical contours, allowing to control the ripple in the emission zone as well as the topography of lateral lobes. The resulting aperture distributions can be complex [10] or real [11]. However, this technique does not allow synthesizing radiation patterns that illuminate an arbitrary contour.

In a later work, F. Ares et al [12] introduced a method that increased or decreased the radius of the aperture in order to synthesize contour distributions that adapt to the irregular area that we want to illuminate, overcoming some of the drawbacks of circular distributions. The method allows to synthesize diagrams that illuminate arbitrary contours through real distributions, which makes it very suitable for the synthesis of footprint diagrams used in satellites. However, such a method is not suitable for illuminating very oblong covers. In addition, the fact that the optimization of the

radiation pattern is carried out by the method of Fletcher Powell [13] poses several problems in finding a suitable solution, besides not allowing to control the dynamic range of the resulting excitations.

One of the biggest challenges presented by flat arrays for satellite applications is the in-orbit detection of potential defective elements in the array, as well as the possible recovery of the beam taking into account the absence of these elements and reconfiguring the excitations of the remaining ones. This requires the use of active antennas, which is the current trend in radio frequency technology.

1.2 Monitoring of the electromagnetic field in the smart cities arena

A concept that is becoming increasingly important, especially in Europe, is the smart cities, namely, built-up areas where citizens enjoy a number of benefits: safer environment, reduced pollution, improved transportation services, reduced overall energy consumption, and so on. To reach these desirable performances, proper rules should be emanated by the competent authorities and appropriate tools implemented.

One relevant problem among those concerning to the improvement of the quality of life of the citizens could be a simple and cheap evaluation of the electromagnetic field intensity (EMFI), aimed to control the exposure level in the city environment of the citizens.

A limited set of electromagnetic hidden sensors of two different types are located in the area under protection. The detailed values of the electromagnetic field intensity on each point of the city will be evaluated by using a rigorous interpolation algorithm, based on the integration of several sensors and a software for the prediction of the field.

This work is based on a philosophy of a wireless network, with a complete fusion between sensors, simulation software and antennas.

The main objective of the presented work is to show an experimental proof in order to validate the proposed method for the real-time monitoring of the electromagnetic field in a urban scenario. The design of the system is based on the location of measurement sensors in some strategic points of the city. This information is fundamental in order to detect unacceptable field intensity levels; also, this information could be transmitted in real time to all the citizens through certain channels (call center or web page), that can be of great interest for the population due to the increasing of the concerns about the exposure levels to the electromagnetic fields.

A simple scheme of the different parts of the proposed system to the monitoring of the electromagnetic field intensity levels are depicted in Fig. 4.

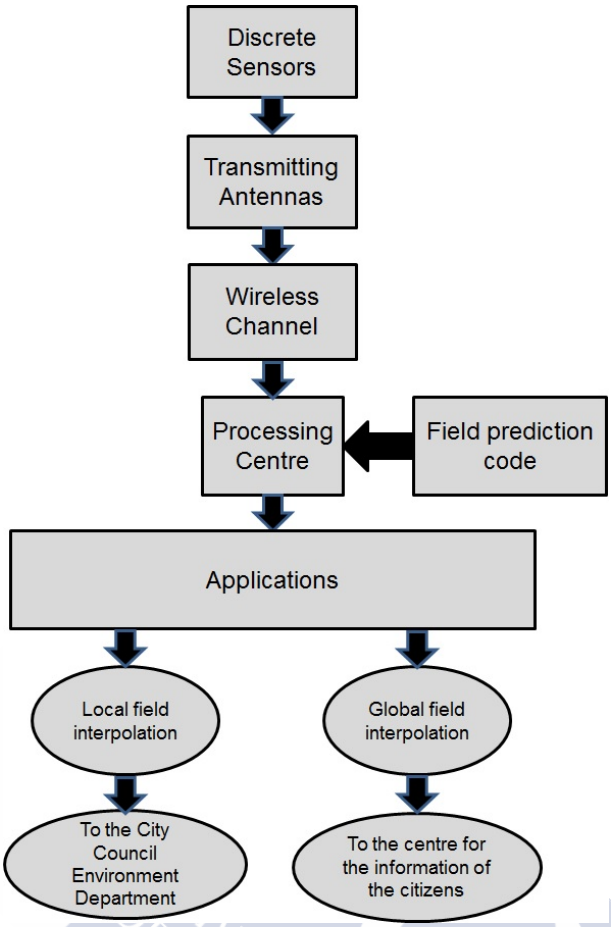

Figure 4: Scheme of the different system elements of the method.

1.3 Dosimetry calculations of SAR in small animals

In recent years, the use of wireless communication technologies has spread widely in our environment. The use of mobile phones, Bluetooth communications, Wifi, 4G, etc. are technologies with which we coexist and that are increasingly used and present in our daily lives. This fact makes the study of the effects of electromagnetic radiation on living beings of great interest. In World War II, the first rigorous studies of the interaction between living beings and electromagnetic energy started. In addition, the population is currently concerned about the possible damage of the radiofrequency (RF) fields to which it is exposed, motivating the growing appearance of studies in this field.

1.3.1 General classification of biological effects

Biological effects refer to measurable responses in those individuals exposed to radiation, which may or may not result in adverse health effects. These effects have been classified as follows [14, 15]: thermal, athermal and non-thermal effects.

- Thermal effects occur when enough energy is deposited in the body to increase the temperature measurably. Electromagnetic radiation is absorbed and transformed into heat. The basic molecular mechanism of heat production is because the interaction of the radiofrequency with the tissue generates vibrations and oscillations of molecular polar, like the water, inside the organism. This rotational energy is transformed into heat [16].

- Athermic effects occur when the deposited energy is sufficient to produce an increase in temperature in the biological tissue, but without the activation of thermoregulation mechanisms. The biological effects observed by this kind of radiation are mainly to induce electrical currents that can stimulate nerve and muscle cells.

- Non-thermal effects occur when the energy deposited in the biological object does not tend to produce temperature increase [16].

Most of the international regulations governing the non ionizing radiation (NIR) consider that the mechanisms involved in the main biological effects involve a thermal effect. A rise in temperature can alter the functioning of various biological systems and even cause irreversible damage. Although there is sufficient evidence on the thermal effects produced by the heating of the tissues exposed to microwave radiation, however, in the last decades an important debate has opened on the possibility of non-thermal effects that are not explained by the increase of the temperature of the tissue [17, 18].

There are multiple experimental studies whose findings have been attributed to the possible existence of biological effects due to exposure to low intensity electromagnetic fields that do not appear to be due to tissue heating. Several studies reveal that microwaves could induce physiological alterations of athermic nature [18], such as altering cellular metabolic processes [19] and altering the structure and function of the cell membrane [20]. Recent researches in cell cultures describe that athermal radiofrequency doses may induce changes in gene expression [21]. Evidence that radiofrequency at athermic doses stimulates the production of heat shock proteins could explain the effects of the radiofrequency on physiological cellular alterations that occur following radiation exposure [21]. However, other authors have not been able to corroborate these results [23, 24], therefore they consider them unreliable. In addition, they explain these effects due to possible errors in temperature measurement systems, or by the existence of hot spots that have not been detected [25]. For all this, more research is needed to obtain conclusive results.

At the level of the central nervous system, there have been indications, both in humans and in animals, of non-thermal effects of the microwave, among which we can highlight the alterations in brain electrical activity [26], cholinergic activity of the brain [27, 28], alterations in the phosphorylation of certain proteins [29], increased permeability of the blood-brain barrier [30] and decreased excitatory synaptic activity at

the level of hippocampal neurons [31].

On the other hand, effects occurring exclusively at athermal doses of radiation have been observed. The biological effects of low frequency exposures do not have a linear proportion to radiation power (window effect) or exposure time (matching mechanism) as might be expected. However, such effects have not been observed after exposure to thermal doses. Therefore, some authors postulate that window effects and matching are related to non-thermal mechanisms [15, 32].

All of this makes the understanding of the biological mechanisms of interaction with electromagnetic fields, especially of the mechanisms underlying the "non-thermal" effects of radiofrequency, is a current topic in research and should be clarified due to its potential adverse health effects.

1.3.2 Dosimetry. SAR calculations.

The basic physical quantity of electromagnetic energy that determines the biological effect is the electromagnetic field induced within the organism exposed to the incident radiation. Dosimetry is therefore defined as the determination of the energy absorbed by a body exposed to the electric and magnetic fields that make up a radiofrequency signal [14].

The absorption of electromagnetic energy in living organisms depends fundamentally on:

First: The parameters of the incident field, i.e. its frequency, its polarization, and the arrangement of the object in front of the incident field.

Second: The characteristics of the exposed body, such as its internal and external geometry or the dielectric properties of the tissues (conductivity and permittivity). The dielectric properties of tissues are largely determined by its water content. In general, the greater the water content of the tissues, the greater its absorption [33]. The results of the calculated values of permittivity and conductivity of the various biological tissues have been very variable, since the biological tissues are very heterogeneous, and these values can be altered of important form depending on the procedure of preparation of the fabric, or of the changes Metabolic postmortem, among others [34].

Third: The effects of earth, reflection or refraction and other objects that can interact between the source and the object. The incident energy is reflected at the level of the various tissue interfaces. The reflection coefficient, which is given by the relation between incident and reflected intensity, is very high at the air-skin interface, indicating that much of the incident energy is reflected without penetrating the tissue.

To determine the interaction of the radiofrequency with the tissues it is essential to describe the following physical parameters:

- The induced current density in the tissues (J).
- The internal electric field strength (E).
- The SAR.

The basic magnitude used for radiofrequency-microwave dosimetry is the Specific Absorption Rate (SAR), which has been defined as the amount of electromagnetic power absorbed by one tissue per unit mass. Its unit of measurement is watt per kilogram (W/kg).

The SAR is a measure of the electric field at the point of study and the local heating rate (dT/dt).

$$\frac{dT}{dt} = \frac{SAR}{c} \quad (^{\circ}C/s) \tag{20}$$

where c is the heat capacity of the tissue ($J/kg^{\circ}C$)

The mathematical formula used to calculate the SAR is as follows,

$$SAR = \sigma E_t^2 \rho^{-1} \quad (W/kg) \tag{21}$$

(V/m), σ the electrical conductivity of the tissue (S/m) and ρ the density of the tissue (kg/m^3).

As we appreciate in the formula, the SAR in the tissues is proportional to the square of the intensity of the electric field generated in the interior of the fabric, due to this it is extremely complex to determine SAR measurements. For this reason the alternatives found are the estimation of SAR in human phantoms in laboratories or perform computational models using specifically developed software tools.

At the experimental level it is essential to define two magnitudes of SAR, the determination of which will be useful in the dosimetry calculations:

- The SAR averaged over the whole body is a unique SAR value that represents the magnitude of SAR averaged over the entire body exposed to radiofrequency.
- Local SAR is a unique SAR value that represents the magnitude of SAR in a small portion of the body exposed to radiofrequency.

1.3.3 Phantoms and radiation systems.

In order to be able to experimentally determine the values of the absorption rate two procedures can be followed. The first is to obtain the value of the field strength in the area of interest, being necessary to know the electrical properties (conductivity, density) of the area under study. The second of the procedures is based on the measurement of temperature variations over the area to be studied (usually used in tissues and cell cultures in vivo).

These measurements can be taken in cadavers, although for practical reasons they are usually used phantoms. A phantom is a synthetic material that presents electrical properties equivalent to those of the actual biological tissue in which it is intended to be measured at certain frequencies of interest. With the current advances in materials it is possible to get phantoms with the shape of the tissue or the area of interest. The measurements are taken through probes, either field strength or temperature, which are implanted in the models during experimentation. With the electric field probes it is possible to obtain a direct value of this parameter at the desired point, these usually combine with optical fiber so that the transmission of the data due to the immunity of this against electromagnetic radiations. One of the limitations of electric field probes is their malfunction at low frequencies, below 150 MHz. Cables pick up spurious signals due to high impedance. Temperature probes are currently booming given their immunity to radiofrequency. There are devices that allow measuring temperature variations of the order of $0.01°C$ based on thermistors. Although they also present limitations and disadvantages, such as in thermocouple based probes that alter the original distribution of the RF field, so that a precise SAR value can not be obtained in the area of interest.

In order to be able to contrast the data obtained through the different probes, the possibility of using numerical simulations has now been added to the experimental systems thanks to the existence of numerical phantoms. These numerical phantoms are obtained by magnetic resonance of the zone or animal of interest computing all their electrical characteristics (density, permittivity, conductivity, etc.) and morphology (size and shape). With these computerized models and using the numerical calculation method it is possible to obtain SAR values. A clear example of this type of systems is the SEMCAD [35] electromagnetic simulation software based on the Finite-Difference Time-Domain method (FDTD). With the help of this type of tools it is possible to complete studies and radiation systems.

Different radiation systems have been presented in the literature to investigate the effects of signals in mobile communications on small animals [36–38]. It is also possible to obtain SAR values based on thermal variations [37, 38], by calculating the value of the electric field strength, or by means of numerical simulations with phantoms [39].

1.3.4 Regulation relating to electromagnetic fields

Faced with the progressive increase of all types of artificial electromagnetic radiation in the environment arises the need to investigate the dangers that can be associated with the different forms of non-ionizing radiation and on the basis of this to establish a safety criteria on exposure to such radiation. For this reason, the International Commission on Non-Ionizing Radiation Protection (ICNIRP) created in 1992 several working groups on radiation protection in collaboration with the World Health Organization (WHO).

Following a thorough and rigorous assessment of all available scientific evidence to date, the Commission issued recommendations in 1998 to limit exposure to electric, magnetic and electromagnetic field (ICNIRP, 1998). These guidelines set a threshold below which electromagnetic field exposure is considered safe. Exposure limits are based on the effects of short-term acute exposure rather than on long-term exposure, as the available scientific information on the long-term effects of exposure to electromagnetic field is considered insufficient to establish limits Quantitative.

Each country establishes its own national standards for exposure to electromagnetic field; most of them are based on the recommendations of the ICNIPR. The Council of Ministers for Health of the European Union endorsed the criteria of the ICNIPR and issued recommendations for the protection of the general public against non-ionizing radiation from 0 Hz to 300 GHz (RCMSUE-1999/519/EC of 12 July 1999).

Subsequently Spain elaborated a regulation that regulates at national level the principles of the Recommendation of the Council of Ministers of Health of the European Union (Real Decree 1066/2001, of 28 of September). This regulation establishes conditions of protection of the public radioelectric domain, restrictions to the radioelectric radiations, and measures of sanitary protection against radioelectric emissions. Some regions have published their own legislation, in four of them the limits of the Royal Decree are respected (Castilla-León, Illes Balears, La Rioja, and Madrid) and in the other three they are reduced to half (Catalunya, Navarra, Castilla- La Mancha).

Both in the RSMSUE and in the regulations elaborated by the Spanish Committee, it is concluded that there is no evidence that exposures to electromagnetic field within the established limits can cause adverse effects to human health. On the other hand, it affirms that the epidemiological studies may not have a sufficient period of latency and/or exposure to obtain definitive conclusions. At the moment there are also no scientific studies that are comprehensive and accurate to assure us the safety of the exposure to these electromagnetic fields. However, these safety recommendations are under continuous review and open to possible modifications in relation to the continuing assessment of new findings regarding the effects of electromagnetic fields on the human body.

1.3.5 Limits for the electromagnetic fields exposure.

The reference levels and the basic restrictions to electromagnetic fields emitted by ICNIRP (1998) are the most widely accepted worldwide.

- Basic restrictions are restrictions on the exposure of time-varying electric, magnetic and electromagnetic fields based on health effects and biological considerations (Table 1).
- The reference levels determine the probability that the basic restrictions will be exceeded and their objective is to ensure compliance with them (Table 2).

Exposure limits set by the ICNIRP guide are more stringent for general public exposure than for occupational exposures. The rationale of the ICNIRP is that the occupationally exposed population includes an adult population trained to take adequate precautions, while the general population encompasses all ages and is generally unaware of the degree of exposure and the precautionary measures to be taken.

For the frequency ranges between 100 KHz and 10 GHz the basic restrictions are provided in terms of SAR to prevent thermal stress of the whole body and localized heating of tissues. All SAR values should be averaged over any 6−minute period. In addition, the mass to average the localized SAR is considered any contiguous tissue of 10 g of mass.

Table 1: Basic restrictions for expositions to electromagnetic fields at frequencies of $10MHz$-$10GHz$ (ICNIRP, 1998).

Characteristics of the exposure	**Mean SAR in whole body (W/kg)**	**Mean SAR in head and trunk (W/kg)**	**Mean SAR in extremities (W/kg)**
Occupational	0.4	10	20
General public	0.08	2	4

Table 2: Reference levels for the exposure to electric and magnetic fields for frequencies in the range of $2 - 300\ GHz$. (Directive 2004/40/CE of the European Parlament and Council of April 29th; Council recommendation of 12 of July of 1999, 1999/512/EC)

Characteristics of the exposure	**Electric field strength E (V/m)**	**Magnetic field strength H (A/m)**	**Magnetic induction (μT)**	**Power density of an equivalent plane wave**
Occupational	137	0.36	0.45	50
General public	61	0.16	0.20	10

References

[1] S. A. Schelkunoff, "A mathematical theory of linear arrays", Bell Syst. Tech. J., Nº 22, pp. 0 107, 1943.

[2] C. L. Dolph, "A current distribution for broadside arrays which optimizes the relationship between beamwidth and side lobe level", Proc. I. R. E., vol. 34, pp. 348-355, 1946.

[3] H. J. Orchard, R. S. Elliott, and G. J. Stern, "Optimizing the synthesis of shaped beam antenna patterns", IEE Proc. Pt. H., vol. 132, Nº 1, pp. 63 68, 1985.

[4] Y. U. Kim and R. S. Elliott, "Shaped-pattern synthesis using pure real distributions", IEEE Trans. Antennas Propagat., vol. AP-36, Nº 11, pp. 1645-1649, 1988.

[5] J. A. Rodriguez, E. Botha, and F. Ares, "Extension of the Orchard-Elliott synthesis method to pure real nonsymmetrical-shaped patterns", IEEE Trans. Antennas Propagat., vol. 45, Nº 8, pp. 1317-1318, 1997.

[6] T. T. Taylor, "Design of line source antennas for narrow beamwidth and low side lobes", Trans. I. R. E., vol. AP 3, pp. 16 28, 1955.

[7] F. Ares, R. S. Elliott, and E. Moreno, "Optimised synthesis of shaped line-source antenna beams", Electronics Letters, vol. 29, pp. 1136-1137, 1993.

[8] F. Ares, R. S. Elliott, and E. Moreno, "Synthesis of shaped line-source antenna beams using pure real distributions", Electronics Letters, vol. 30, pp. 280-281, 1994.

[9] T. T. Taylor, "Design of circular apertures for narrow beamwidth and low side lobes", Trans. I. R. E., vol. AP 8, pp. 17 22, 1960.

[10] R. S. Elliott and G. J. Stern, "Shaped patterns from a continuous planar aperture distribution", IEE Proc. Pt. H, vol. 135, pp. 366-370, 1988.

[11] R. S. Elliott and G. J. Stern, "Footprint patterns obtained by planar arrays", IEE Proc. Pt. H, vol. 137, pp. 108-112, 1990.

[12] F. Ares, R. S. Elliott, and E. Moreno, "Design of planar arrays to obtain efficient footprint patterns with an arbitrary footprint boundary", IEEE Trans. Antennas Propagat., vol. AP-42, Nº 11, pp. 1509-1514, 1994.

[13] R. Flecher and M. J. D. Powell, "A rapidly convergent descent method of minimization", Computer J., vol. 6, 163-168, 1963.

[14] J. L. Sebastian Franco, S. Muñoz San-Martín, M. Sancho Ruiz, and J. M. Miranda Pantoja, 'Medición de radiación en seres vivos', Investigación y Ciencia, Frebrero 2006.

[15] J. A. Laurence, P. W. French, R. A. Lindner, and D. R. Mckenzie, 'Biological effects of electromagnetic fields-mechanisms for the effects of pulsed microwave radiation on protein conformation', J. Theor. Biol., vol. 206, pp. 291-298, 2000.

[16] L. J. Challis, 'Mechanisms for interaction between RF fields and biological tissues', Bioelectromagnetics supplement, vol. 7, pp. 98-106, 2005.

[17] A. S. Dawe, B. Smith, D. W. P. Thomas, S. Greedy, N. Vasic, A. Gregory, B. Loader, and D. De Pomerai, 'A small temperature rise may contribute towars the apparent induction by microwaves of heat shoc gene expression in the nematode caernorhabditis elegans', Bioelectromagnetics, vol. 27, pp. 88-97, 2006.

[18] S. Banik, S. Bandyopadhyay, and S. Ganguly, 'Bioeffects of microwaves: a brief review', Bioresource Technology., vol. 87, no. 2, pp. 155-159., 2003.

[19] S. P. Samarketu and S.P. Singh, 'Effect of direct modulated microwave modulation frequencies exposure on physiology of cyanobacterium Anabea dolilum', Asia Pacific Microwave Conference, vol. B.2.1., pp. 155-158, 1996.

[20] A. M. Phelan, C. F. Neubauer, R. Timm, J. Neirenberg, and D. G. Lange, 'Athermal alterations in the structure of the canalicular membrane and ATPase activity induced by thermal levels of microwave radiation', Radiation Research, vol. 137, no. 1, pp. 52-58, 1994.

[21] S. Lee, D. Jhonson, K. Dubar, H. Dong, X. Ge, C. Y. Kim, C. Wing, N. Jayathilaka, N. Emmanuel, C. Q. Zhou, H. L. Gerber, C. C. Tseng, and S. M. Wang, '2.45 GHz radiofrequency fields alter gene expression in cultured human cells', FEBS letters, vol. 579. 4829-4836, 2005.

[22] P. W. French, R. Penny, J. A. Laurence, and D. R. McKenzie, 'Mobile phones, heat shock proteins and cancer', Differentiation, vol. 67, no. 4-5, pp. 93-7, 2001.

[23] E. R. Adair, B. W. Adams, G. M. Akel, 'Minimal changes in hypothalamic temperature accompany microwave-induced alteration of thermoregulatory behavior', Bioelectromagnetics, vol. 5, no. 1, pp. 13-30, 1984.

[24] V. Chauhan, A. Mariampillai, G. B. Gajda, A. Thansandote, and J. P. McNamee, 'Analysis of protooncogene and heat-shock protein gene expression in human derived cell-lines exposed in vitro to an intermittent 1.9 GHz pulse-modulated radiofrequency field', Int J Radiat Biol., vol. 82, no. 5, pp. 347- 354, 2006.

[25] C. Antonio and R. T. Deam, 'Can "microwave effects" be explained by enhanced diffusion', Physical Chemistry Chemical Physics, vol. 9, pp. 2976-2982, 2007.

[26] R. K. Sinha, Y. Aggarwal, P. K. Upadhyay, A. Dwivedi, A. K. Keshri, and B. N. Das, 'Neural network-based evaluation of chronic non-thermal effects of modulated 2450 MHz microwave radiation on electroencephalogram', Annals of Biomedical Engineering, vol. 36, no. 5, pp. 839-851, 2008.

[27] V. Vorobyov, V. Pesic, B. Janac, and Z. Prolic, 'Repeated exposure to low-level extremely low frequency-modulated microwaves affects baseline and scopolamine-modified electroencephalograms in freely moving rats', International Journal of Radiation Research, vol. 80, no. 9, pp. 691-698, 2008.

[28] H. Lai, M. A. Carino, A. Horita, and A. W. Guy, 'Low level microwave irradiation and central cholinergic systems', Pharmacology Biochemestry and Behavior, vol. 33, pp. 131-138, 1989.

[29] D. Leszcynski, S. Joenväärä, J. Reivinen, and R. Kuokka, 'Non-thermal activation of the hsp27/p38MAPK stress pathway by mobile phone radiation in human endothelial cells: Molecular mechanism for cancer and blood-brain barrier-related effects', Differentiation, vol. 70, pp. 120-129, 2002.

[30] C. Neubauer, A. M. Phelan, H. Kues, and D. G. Lange, 'Microwave irradiation of rats at 2.45 GHz activates pinocytotic-like uptake of tracer by capillary endothelial cells of cerebral cortex', Bioelectromagnetics, vol. 11, no. 4, pp. 261-268, 1990.

[31] S. Xu, W. Ning, Z. Xu, S. Zhou, H. Chiang, and J. Luo, 'Chronic exposure to GSM 1800 MHz microwaves reduces excitatory synaptic activity in cultured hippocampal neurons', Neuroscience Letters, vol. 398, pp. 253-257, 2006.

[32] S. Kwee, 'Absence of linear correlation between biological effects and power density in the nonthermal radiofrecuency radiation range', Biological Effects of EMFs. 4th International Workshop., vol. 1, pp. 401-406, 2006.

[33] M. J. Schroeder, A. Sadasiva, and R. M. Nelson, 'An analysis on the role of wáter content and state on effective permittivity using mising formulas', Biomechanics, Biomedical and Biophysical Engineering, vol. 2, no. 1, pp. 1-10, 2008.

[34] G. Schimid, G. Neubauer, and P. R. Mazal, "Dielectric properties of human brain tissue measured less than 10h postmortem at frequencies from 800 to 2450 MHz", Bioelectromagnetics, vol. 24, pp. 423-430, 2003.

[35] Schmid & Partner Engineering AG, Reference manual for the SEMCAD simulation platform for electromagnetic compatibility, antenna design and dosimetry, disponible en www.semcad.com, 2010.

[36] N. Kuster, V. Berdiñas-Torres, N. Nikoloski, M. Frauscher, and W. Kainz, 'Methodology of detailed dosimetry and treatment of uncertainty and variations for in vivo studies', Bioelectromagnetics, vol. 27, pp. 378-391, 2006.

[37] E. G. Moros, W. L. Straube, and W. F. Pickard, 'A compact shielded exposure system for the cimultaneous long-term UHF irradiation of forty small mammals: I. Electromagnetic and environmental design', Bioelectromagnetics, vol. 19, pp. 459-468, 1998.

[38] M. Swicord, J Morrisey, D. Zakharai, M. Balien, and Q. Balzano, 'Dosimetry in mice exposed to 1.6 GHz microwaves in a carrousel irradiator', Bioelectromagnetics, vol. 20, pp. 42-47, 1999.

[39] F. Schoenborn, K. Popovic, and N. Kuster, 'Dosimetric analysis of the carousel setup for the exposure of rats at 1.62 GHz', Bioelectromagnetics, vol. 25, pp. 16-26, 2004.

USC
UNIVERSIDADE
DE SANTIAGO
DE COMPOSTELA

2 Synthesis problem of Taylor-like patterns with isophoric multi-ring planar antennas

Along this chapter we will describe the synthesis of circular Taylor-like patterns for antennas exhibiting concentring rings of uniformly excited elementes (that is, isophoric). The optimization goal is to achieve the close approximation of the envelope of desired pattern into a cone region around the main lobe. Also, we will discuss the approaching by using annular subarrays as an alternative in order to obtain a better results in terms of time computation. In this reformulation of the problem we will limit the number of between-ring spacings. Different examples will illustrate the potential of these methods. The results of this work were published in [1].

2.1 Introduction

In the context of continuing demand for high-resolution antennas, the budgetary constraints of recent years have enhanced interest in aperiodic arrays of radiating elements with excitations that are either all equal or differ only in phase. Such arrays need only relatively simple feed networks, and exploit the full power capability of all elements. A geometry that has always attracted attention in this respect is that of the concentric ring array [2–4]. In [2], simulated annealing was used to optimize relevant pattern parameters by varying the ring radii; [3] showed how to implement a circular planar version of the density tapering technique [5, 6], array elements being located so that the local average excitation density approximated that of a circular Taylor pattern [7]; while [4] employed genetic algorithms, with or without the help of local optimization procedures, to optimize ring radii, within-ring element spacing, or both. Multi-objective optimization, e.g. to balance beamwidth against maximum sidelobe level (SLL), has been considered by *Bianchi et al.* [8]. For references to the older literature, the above papers may be consulted. Though not directly relevant to this thesis, readers may also be interested in recent work on uniformly excited circular arrays in which elements or subarrays are arranged on square [9, 10], hexagonal [10] or spiral [11] grids.

It is characteristic of the radiation patterns of nonuniformly spaced arrays that highish side lobes tend to appear at wide angles. For linear arrays, received wisdom holds that the pattern of a symmetric density-tapered array with $2N$ elements is a good approximation to that of the corresponding amplitude-tapered array out to about the N-th side lobe [6], and results for $2N$ ring arrays also suggest good behaviour out to side lobe N [4]. In this work we report that rigorous control at small-to-medium angles from the main beam can be imposed by optimizing ring radii so that sidelobe peaks lie close to an envelope function fitted to the target function sidelobe peaks. Furthermore, acceptable results can be achieved even when the number of available degrees of freedom is reduced by the use of annular subarrays, in each of which the ring-spacing is uniform. The envisaged applications for these results are in the field of K_a-band multibeam satellite antennas.

2.2 Optimization of individual ring radii

Assuming that our arrays have quadrantal geometry symmetry consisting of M concentric rings of isotropic elements, the mth ring having radius ρ_m and m elements per quadrant, with the position of the nth element of its first quadrant being given by

$$x_{mn} = \rho_m \cos\left[\frac{(2n-1)\pi}{4m}\right] \tag{22}$$

$$y_{mn} = \rho_m \sin\left[\frac{(2n-1)\pi}{4m}\right] \tag{23}$$

Since the elements have uniform excitations, the field $F(\theta, \phi)$ generated by the annular array is given by

$$F(\theta, \phi) = 4 \sum_{m=1}^{M} \sum_{n=1}^{m} \cos(kx_{mn} \sin\theta \cos\phi) \cos\left(ky_{mn} \sin\theta \sin\phi\right) \tag{24}$$

where k is the wavenumber, and since the pattern is approximately ϕ-symmetric (due to the circular placement of the elements), (24) may be approximated by

$$F(\theta) \approx 4 \sum_{m=1}^{M} \sum_{n=1}^{m} \cos(kx_{mn} \sin\theta) \tag{25}$$

We assume that in reproducing a given pattern, what is really required of a uniformly excited array is that it reproduce the envelop of the corresponding power pattern, rather than the exact location of nulls. Here we consider target power patterns of circular Taylor type [7], with given values of the Taylor parameter $\bar{n}$ and given nominal SLL, as generated by a continuous aperture of given radius and expressed in dB relative to the mainbeam peak. Although it is possible to use alternative target patterns, Taylor distributions are highly efficient and relatively robust toward changes in frequency.

We approximate the sidelobe envelope of the target pattern with an *ad hoc* function (denoted $env(\theta)$) that is supplied by the program TableCurve 2-D as the function best fitting the sidelobe maxima (Fig. 5). Given and the function $env(\theta)$, simulated annealing [12] is used to vary the ring radii so as to make the sidelobe maxima of $P(\theta)$, the power pattern of $F(\theta)$ expressed in dB relative to the mainbeam peak, lie close to $env(\theta)$ while keeping beamwidth close to that of the Taylor pattern and ensuring that adjacent radiating elements are separated by at least $\lambda/2$ so as to minimize mutual coupling. This last condition is implemented by defining the ring radii recursively by

$$\rho_m = \rho_{m-1} + 0.5\lambda + \delta_m \tag{26}$$

where $\rho_0 = 0$, $\delta_m \geq 0$, and initially $\delta_m = 0$. The conditions on the sidelobe maxima and half-power beamwidth BW are implemented via the cost function

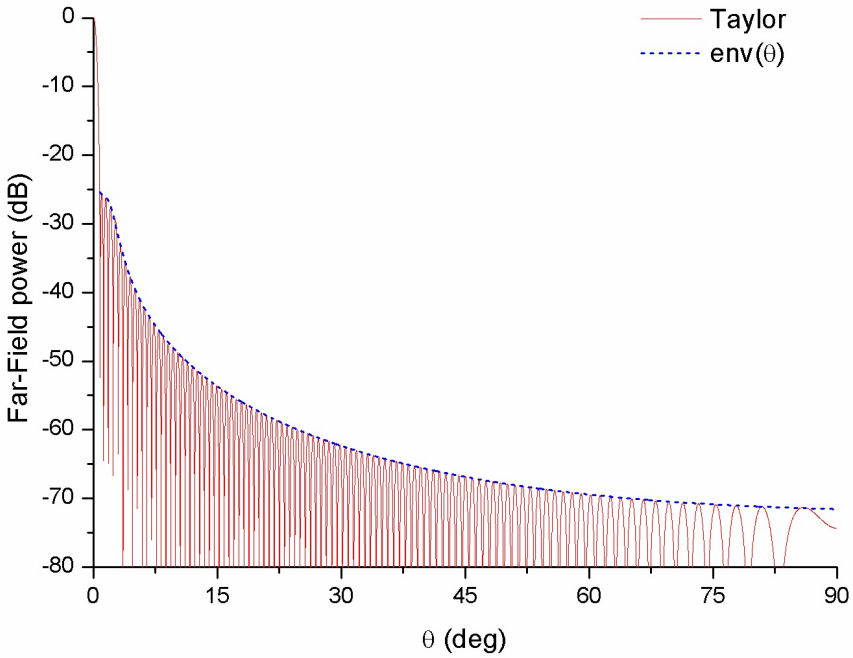

Figure 5: Solid line: Taylor pattern with nominal $SLL = -25\ dB$ and synthesized by a circular aperture of radius 50λ. Dashed line: approximate envelope function $env(\theta)$ fitted to the Taylor sidelobe maxima.

$$C = k_1 \times RMS + k_2 \times (BW - BW_d)^2 \tag{27}$$

where BW_d is the $3dB$ beamwidth of the Taylor pattern, the coefficients k_i control the relative weights of the two terms, and

$$RMS = \sqrt{\frac{\sum_{p=1}^{N} [P(\theta_p) - env(\theta_p)]^2}{N}} \tag{28}$$

where θ_p is the position of the p-th sidelobe maximum of $P(\theta)$ and N is the number of controlled maxima. Note that since $(BW - BW_d)^2$ is invariably small compared to initial RMS, k_2 must be considerably larger than k_1.

The radiation patterns of non-isotropic elements can be factored into the pattern in the usual way.

When synthesizing for a main beam scanned to (θ_0, ϕ_0) by setting the phases of elements to

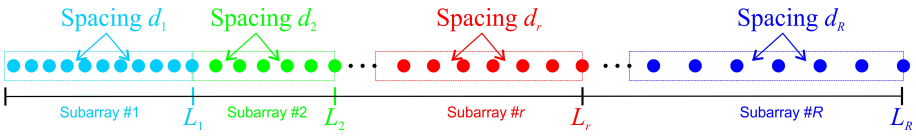

Figure 6: Between-ring spacing along a radius of the array, showing successive annular subarrays. The array centre is at the left.

$$\alpha(x, y) = -k \sin\theta_0 (x \cos\phi_0 + y \sin\phi_0) \tag{29}$$

the pattern must be calculated using (24) with $\sin\theta\cos\phi$ and $\sin\theta\sin\phi$ replaced by $(\sin\theta\cos\phi - \sin\theta_0\cos\phi_0)$ and $(\sin\theta\sin\phi - \sin\theta_0\cos\phi_0)$, respectively; and in (28), θ_p should be the position of the p-th sidelobe maximum in the ϕ-cut through (θ_0, ϕ_0).

2.3 Use of annular subarrays with uniform ring spacing

Some computational simplification can be achieved by limiting the number of distinct between-ring spacing values in subarray fashion, i.e. by dividing the set of rings in a small number of annuli, in each of which the between-ring spacing is uniform [13]. We may thus consider R annuli, with between-ring spacing d_r in the r-th annulus, the outer edge of which has radius L_r (Fig. 6; we abuse language somewhat, since the first annulus is actually a disk). The number of rings in the r-th annulus is

$$N_r = \frac{L_r - L_{r-1}}{d_r} \tag{30}$$

(L_0 is defined to be identically zero), and the radius of the s-th ring of the r-th annulus is

$$\rho_{rs} = L_{r-1} + s d_r \tag{31}$$

For given R and maximum allowed antenna radius L_R (set equal to the radius of the circular aperture synthesizing the desired Taylor pattern), the $2R-1$ unknowns L_r $(1 \le r \le R-1)$ and d_r $(1 \le r \le R)$ are optimized by simulated annealing so as to minimize the cost function C of (27) (as above, and in the same way, the between-ring spacings d_r are constrained to exceed 0.5λ). Note that when this subarray approach is used, the antenna radius is fixed and the number of rings is implicitly optimized, instead of *vice versa*.

2.4 Examples

In the following examples the unscanned target pattern was a circular Taylor pattern with nominal $SLL = -25dB$ and $\bar{n} = 5$ (this value of $\bar{n}$ affords maximum directivity for the given nominal SLL), as generated by a continuous circular aperture of radius 50λ (Fig. 5). The peak directivity of this pattern is $49.7dBi$ and its efficiency η (the ratio between

its peak directivity and that of a uniformly excited aperture of equal size) is 94%. In examples A-C, on the basis of previous experience in which a radius:rings ratio of about $5/8\lambda$ had emerged with various antenna sizes (see the Appendix), we considered an 80-ring array with 3240 elements per quadrant; in example D, setting the antenna radius to 50λ also led to an 80-ring array. In all cases, optimization was performed with $k_1 = 1$ and $k_2 = 100$ in (27). The program was written in C and executed on a PC with 8 Gb of RAM and an Intel Core $i7$ processor running at $3.40GHz$. Execution times were 15-20 minutes when ring radii were optimized individually, and 3-5 minutes when subarrays were used.

(A) **Isotropic elements, RMS calculated using all $\theta \in (0°, 90°)$.**

Using all the maxima in the visible region to calculate RMS in the optimization procedure led to a pattern with an SLL of $-22.2\ dB$ and a peak directivity of 49.2 dBi. However, this procedure failed to suppress the relatively high wide-angle side lobes that are typical of the patterns of density-tapered arrays (Fig. 7). Suspecting that the attempt to do so was favouring deviation from $env(\theta)$ nearer the main beam, in the next example we excluded wide angles from the calculation of RMS.

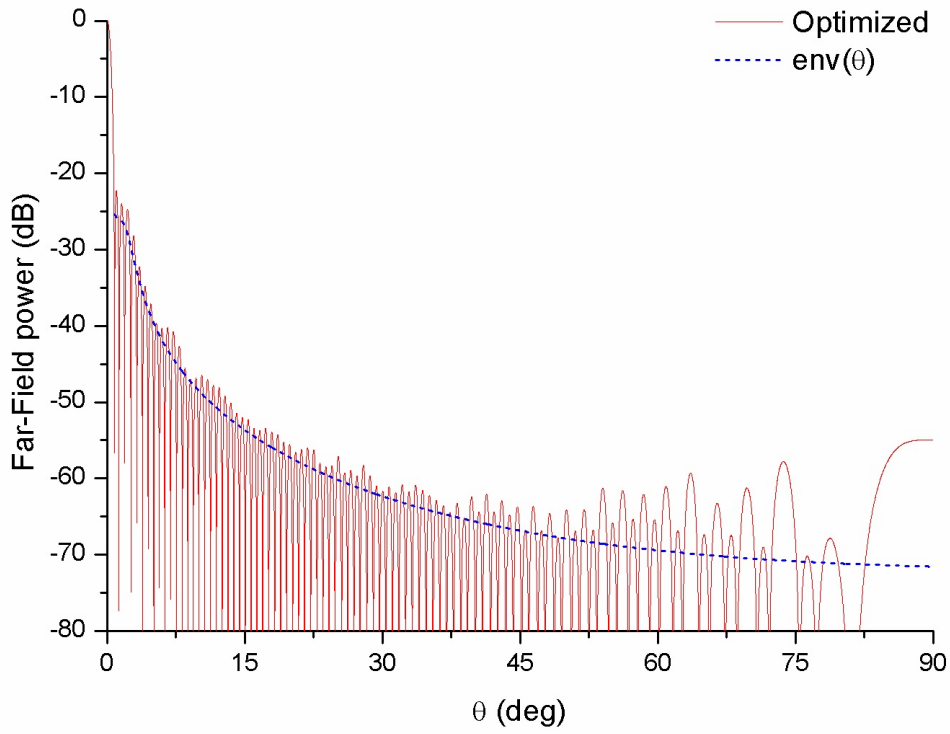

Figure 7: Power pattern of an 80-ring, $4\times3240-$element density-tapered array of isotropic elements in the plane $\phi = 0°$. Array synthesis included all maxima in the visible region in the calculation of deviation from $env(\theta)$ (dashed line).

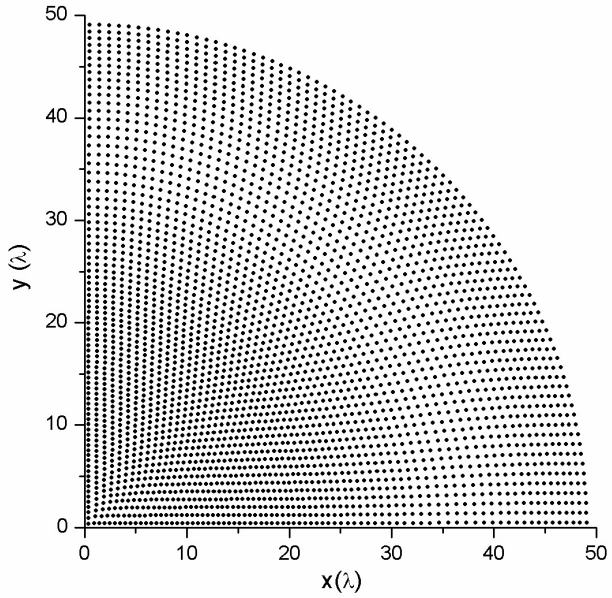

Figure 8: The layout of the first quadrant of the $4 \times 3240-$element density-tapered ring array of Table 3.

(B) **Isotropic elements, RMS calculated using all $\theta \in (0°, 50°)$.**

Using only the maxima with locations $\theta_p < 50°$ in the calculation of RMS led to a pattern with an SLL of -24.7 dB and a peak directivity of 49.5 dBi, the same as that of a circular Taylor aperture of radius equal to that of the largest ring in the present array, 49λ (Table 3). Fig. 8 shows the first quadrant of the optimized layout, and Fig. 9 the excellent fit of the synthesized pattern to $env(\theta)$ in the controlled region. Note that even in the uncontrolled region, all side lobes are now below -55 dB. Pattern quality declined if sidelobe control was attempted over a wider region than (0°, 50°).

The discussion about the pattern quality was based on two parameters: *Radius:rings ratio* and *Sidelobe control region*.

Radius:rings ratio. Our experience with various radius:rings ratios is illustrated by the results of systematic exploration of this issue for a Taylor target pattern with $SLL = -25dB$ and as generated by a continuous circular aperture of radius 25λ. Regardless of the sidelobe control region, the root mean square deviation between $env(\theta)$ and the sidelobe peaks of the synthesized pattern in this region was least for a radius:rings ratio of $5/8\lambda$ (Table 4).

Sidelobe control region. The maximum width of the region in which good control of side lobes can be achieved naturally depends on the quantitative interpretation of 'good'. Here we quantify performance in terms of RMS, the root mean square deviation between $env(\theta)$ and the sidelobe peaks of the synthesized pattern in the sidelobe control region. Increasing the width of the control region increases RMS. For arrays of various sizes with the apparently optimal radius:rings ratio of $5/8\lambda$, RMS begins to increase faster than about 0.2 per 10° when the control region is $(0^\circ, 40^\circ)$, and for $(0^\circ, 60^\circ)$ exceeds 1.0 (Table 5).

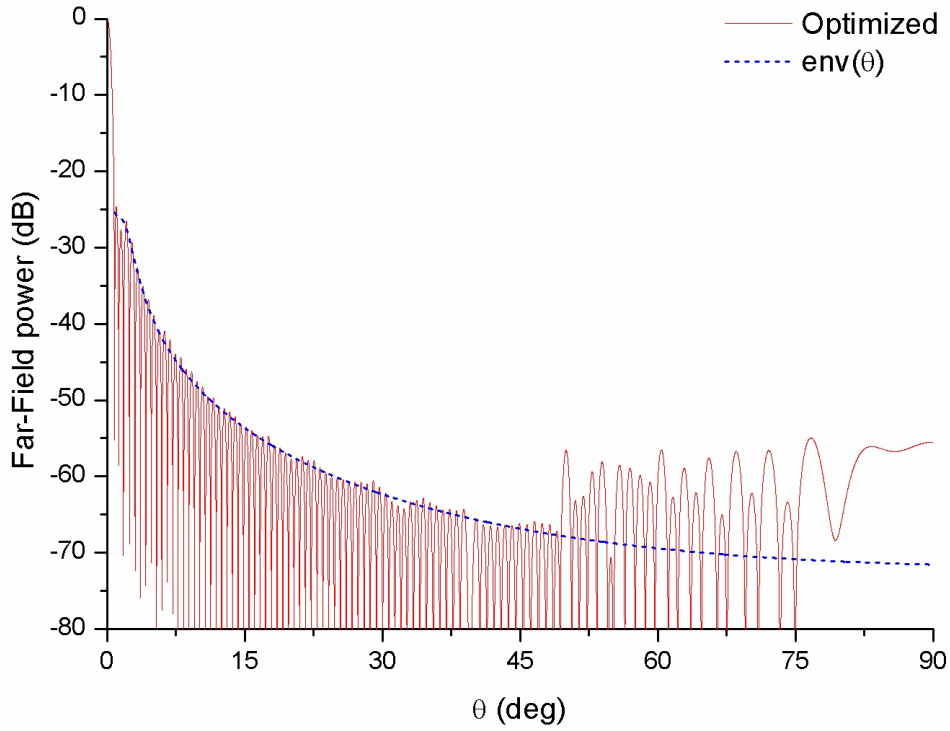

Figure 9: Power pattern of the circular array of Table 3 in the plane $\phi = 0^\circ$ when the elements are isotropic, together with the function $env(\theta)$ (dashed line) to which the pattern maxima were fitted in the region $\theta \in (0^\circ, 50^\circ)$.

By way of comparison with the performance of a non-uniformly excited antenna, we note that at $\theta = 0.325^\circ$, the edge of coverage (EOC) stipulated for the multibeam designs tendered in [14], the directivity of the pattern of Fig. 9 is 46.3 dBi (cf. 46.4 dBi for the circular Taylor distribution of the same size), while the SLL with respect to EOC is -21.6 dB. These values, obtained with a uniformly excited array of radius 49λ, are quite similar to those obtained in [15] with a continuous aperture of radius

60λ (EOC directivity 46.8 dBi, SLL -22.2 dB relative to EOC), even though the antenna of Table 3 was not optimized for these parameters.

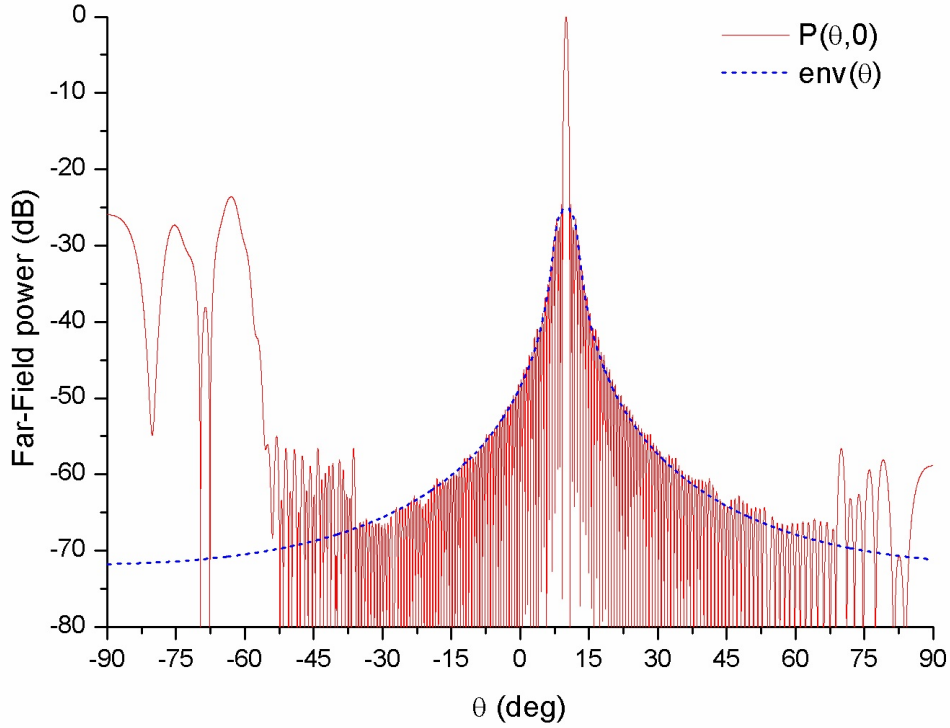

Figure 10: Power pattern of the circular array of Table 3 in the plane $\phi = 0°$ when the elements are isotropic and the main beam is scanned to ($\theta_0 = 10°$, $\phi_0 = 0°$), together with the corresponding function $env(\theta)$.

Table 6 (at the end of this chapter) lists the directivities and SLLs achieved when the main beam of the array of Table 3 is scanned to various angles by giving the elements appropriate phases while maintaining their uniform amplitudes (note that the geometry of the array was kept fixed, not re-optimized for each scan angle). Also shown are the root mean square deviations between $env(\theta)$ and the sidelobe peaks of the synthesized pattern in the whole visible region (RMS_{vis}), a region corresponding to the region in which sidelobe peaks were controlled during synthesis ($\theta_0 - 50°$, $\theta_0 + 50°$) (RMS_{50}), and the region ($\theta_0 - 10°$, θ_0+10°) (RMS_{10}). Note that for a geostationary satellite, a scan angle of 10° is sufficient to cover its view of the earth; Fig. 10 shows the section through $\phi = 0°$ when scanning to (10°, 0°). As expected, increasing the scan angle reduces directivity and raises SLL due to the presence of pseudo-grating lobes, but the topography of the pattern around the main lobe is kept

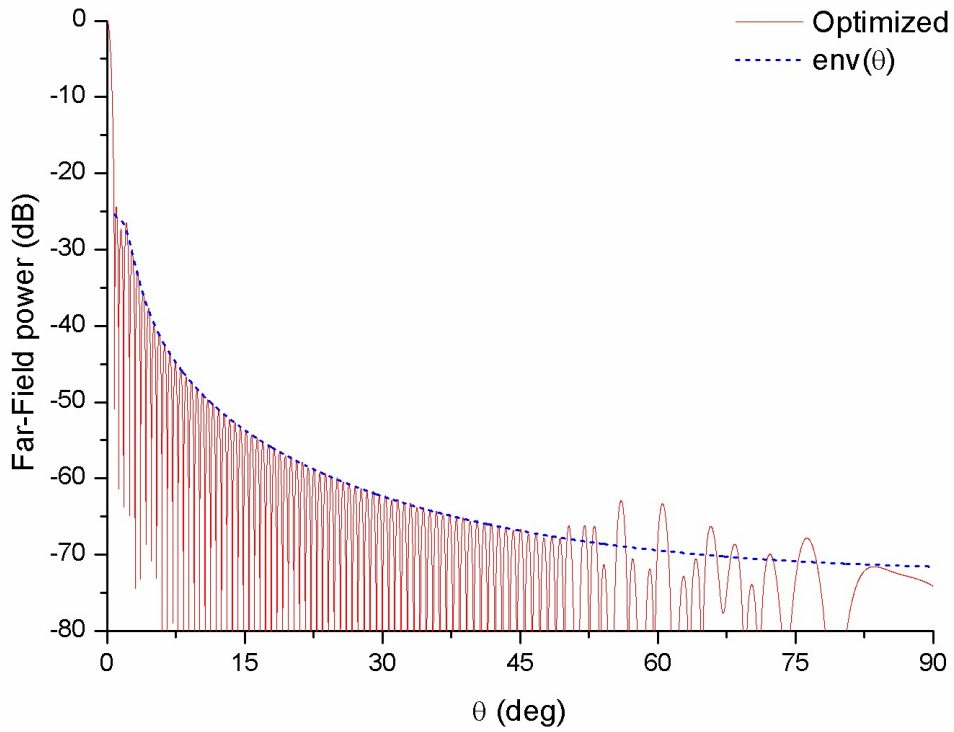

Figure 11: Power pattern of the density-tapered array of Table 8 in the plane $\phi = 0°$ when the element factor is $\cos^2(h_{20}\theta)$. The array was synthesized with all maxima in the range (0°,50°) included in the calculation of deviation from $env(\theta)$ (dashed line).

under control. In particular, for all the scan angles in Table 6, the highest side lobe within 50° of the main beam is the first, which maintains its level of $-24.7\ dB$.

(C) **Non-isotropic elements, RMS calculated using all $\theta \in (0°, 50°)$.**

When the synthesis of the previous subsection was repeated for non-isotropic elements with an element factor $\cos^2(h_{20}\theta)$, with the scaling factor h_{20} giving a taper of $-20\ dB$ at $\theta = 90°$, peak directivity and sidelobe level were hardly altered ($SLL = -24.5dB$, peak directivity $= 49.6dBi$), but behaviour at wide angles was much improved (Fig. 11), as was robustness under scanning (Table 7). Thus, scanning to 20° raised the SLL by just 0.1 dB and reduced directivity by only 1.2 dBi, whereas with isotropic elements SLL rose by 4.6 dB and there was a 3 dBi loss of directivity. Table 8 lists the ring radii of the antenna optimized for $\cos^2(h_{20}\theta)$ elements.

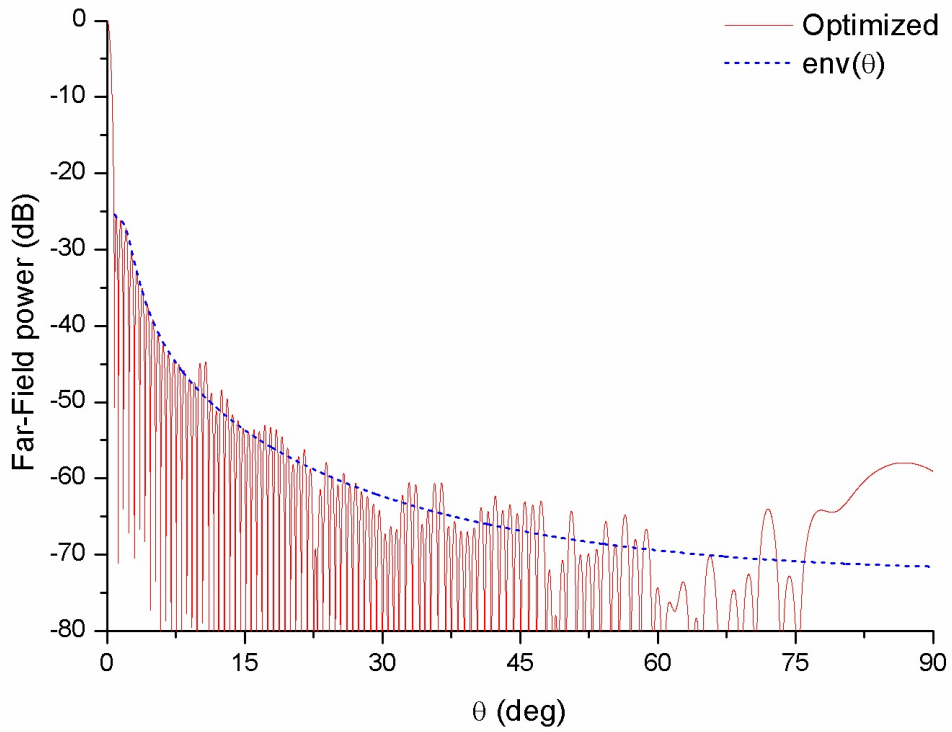

Figure 12: Power pattern, in the plane $\phi = 0°$, of the array described in Table 9, synthesized with all maxima in the range $(0°, 10°)$ included in the calculation of deviation from $env(\theta)$ (dashed line).

(D) **Array composed of annular subarrays of non-isotropic elements, *RMS* calculated using all $\boldsymbol{\theta} \in (\mathbf{0°, 10°})$.**

In this last example we considered an array composed of subarrays as described in section 2.3. Fixing the between-ring distance in each annular subarray reduces the number of degrees of freedom for optimization, which speeds calculations (in this case by a factor of $4-5$) but can also leave the best solutions outside the accessible solution space. In this case, a goodness-of-fit similar to that of the previous examples could only be achieved if sidelobe control was limited to the region $(0°, 10°)$, i.e. if during optimization RMS was calculated using only sidelobe peaks in this region. With $R = 8$, $L_R = 50\lambda$ and the element factor $\cos^2(h_{20}\theta)$, an $80-$ring array was synthesized that generated a power pattern with an SLL of $-25.4\ dB$ and a peak directivity of $49.7\ dBi$ (Fig. 12). Table 9 lists the between-ring spacing and the number of rings in each of the eight subarrays, Table 10 the radii of each ring, and Table 11 scanning results. Attempts to use a smaller number of subarrays while

maintaining the other conditions failed to achieve patterns with $SLL \leq -25dB$. It may be noted that although the controllable region was narrower than when the ring radii were optimized individually, performance in regard to the specifications of [14] actually improved, the directivity at EOC being 46.4 dBi and the SLL with respect to EOC -22.1 dB.

Table 3: Ring radii of an 80-ring, 4×3240-element density-tapered array of isotropic elements with a power pattern fitting the envelope of a -25 dB circular Taylor pattern in the range $\theta \in (0°, 50°)$.

Ring	$\rho_m(\lambda)$	**Ring**	$\rho_m(\lambda)$	**Ring**	$\rho_m(\lambda)$	**Ring**	$\rho_m(\lambda)$
1	0.50	21	10.73	41	21.07	61	34.57
2	1.02	22	11.24	42	21.60	62	35.46
3	1.57	23	11.74	43	22.14	63	36.36
4	2.07	24	12.24	44	22.71	64	37.27
5	2.58	25	12.74	45	23.26	65	38.16
6	3.08	26	13.25	46	23.85	66	39.02
7	3.58	27	13.77	47	24.44	67	39.87
8	4.09	28	14.27	48	25.05	68	40.68
9	4.59	29	14.80	49	25.67	69	41.48
10	5.10	30	15.31	50	26.30	70	42.25
11	5.62	31	15.82	51	26.96	71	43.00
12	6.13	32	16.36	52	27.62	72	43.74
13	6.66	33	16.86	53	28.30	73	44.44
14	7.17	34	17.40	54	29.00	74	45.13
15	7.68	35	17.91	55	29.71	75	45.78
16	8.20	36	18.42	56	30.46	76	46.44
17	8.71	37	18.95	57	31.22	77	47.05
18	9.21	38	19.46	58	32.02	78	47.69
19	9.72	39	20.00	59	32.83	79	48.27
20	10.23	40	20.51	60	33.69	80	48.96
Minimum spacing: 0.50λ				Maximum spacing: 0.91λ			

Table 4: Root mean square deviation between $env(\theta)$ and the sidelobe peaks in the sidelobe control region, for various control regions and number of rings. Target pattern: Taylor $-25\ dB$, $\bar{n} = 5$ as synthesized by an aperture of radius 25λ.

Number of rings	**Radius: rings ratio (λ)[a]**	**(0°, 40°)**	**(0°, 50°)**	**(0°, 60°)**
35	5/7	0.6	1.3	2.2
38	5/7.6	0.3	1.0	2.0
40	5/8	0.1	0.6	1.5
42	5/8.4	0.3	1.2	1.9
45	5/9	0.9	1.7	2.9

[a] The radius is that of the continuous circular aperture defining the target pattern.

Table 5: Root mean square deviation between $env(\theta)$ and the sidelobe peaks in the sidelobe control region, for various control regions and target pattern sizes. Target pattern: Taylor $-25\ dB$, $\bar{n} = 5$.

Radius (λ)[a]	10	25	50
No. of rings	16	40	80
(10°)	0.0	0.0	0.1
(20°)	0.1	0.1	0.1
(30°)	0.3	0.1	0.1
(40°)	0.4	0.1	0.2
(50°)	0.8	0.6	0.7
(60°)	1.4	1.5	1.6
(70°)	2.0	1.6	2.4
(80°)	2.3	2.1	2.9
(90°)	3.9	2.6	3.1

[a] The radius is that of the continuous circular aperture defining the target pattern.

Table 6: Performance of the array of Table 3 when the main beam is scanned to (θ_0,0°).

$\theta_0(°)$	**Directivity** (dBi)	**SLL**^{a} $\boldsymbol{dB}$	$\boldsymbol{RMS^b_{10}}$	$\boldsymbol{RMS^b_{50}}$	$\boldsymbol{RMS^c_{vis}}$
0	49.5	-24.7	1.0	0.7	5.0
5	48.4	-23.6	1.0	1.3	6.3
10	47.2	-23.6	1.1	1.7	7.2
15	46.0	-21.7	1.4	2.1	8.6
20	45.5	-20.1	1.7	2.4	10.3

^{a}SLL in the whole visible region. The highest sidelobe level in the regions $(\theta_0 - 10°, \theta_0 + 10°)$ and $(\theta_0 - 50°, \theta_0 + 50°)$ was in all cases $-24.7dB$. $^b RMS_\alpha$ is the root mean square deviation of sidelobe peaks from $env(\theta)$ in the region $(\theta_0 - \alpha, \theta_0 + \alpha)$. ^{c}Root mean square deviation of sidelobe peaks from $env(\theta)$ in the whole visible region.

Table 7: Performance of the array of Table 8 with element factor $\cos^2(h_{20}\theta)$ when the main beam is scanned to (θ_0,0°).

$\boldsymbol{\theta_0(°)}$	**Directivity** $\boldsymbol{(dBi)}$	**SLL**^{a} $\boldsymbol{(dB)}$	$\boldsymbol{RMS^b_{10}}$	$\boldsymbol{RMS^b_{50}}$	$\boldsymbol{RMS^b_{vis}}$
0	49.6	-24.5	0.5	0.3	3.3
5	49.5	-24.4	0.6	1.3	5.3
10	49.3	-24.4	0.6	1.5	5.7
15	48.9	-24.4	0.8	2.2	7.0
20	48.4	-24.4	1.0	2.4	8.8

^{a}SLL in the whole visible region. The highest sidelobe level in the regions $(\theta_0 - 10°, \theta_0 + 10°)$ and $(\theta_0 - 50°, \theta_0 + 50°)$ was in all cases the same. $^b RMS_{10}$, RMS_{50} and RMS_{vis} defined as in Table 6.

Table 8: Ring radii of an 80-ring, 4×3240-element density-tapered array of isotropic elements with a power pattern fitting the envelope of a -25 dB circular Taylor pattern in the range $\theta \in (0°, 50°)$, synthesized for elements with element factor $cos^2(h_{20}\theta)$.

Ring	$\boldsymbol{\rho_m(\lambda)}$	**Ring**	$\boldsymbol{\rho_m(\lambda)}$	**Ring**	$\boldsymbol{\rho_m(\lambda)}$	**Ring**	$\boldsymbol{\rho_m(\lambda)}$
1	0.50	21	10.75	41	21.06	61	34.67
2	1.08	22	11.25	42	21.59	62	35.55
3	1.63	23	11.75	43	22.18	63	36.43
4	2.13	24	12.25	44	22.73	64	37.30
5	2.67	25	12.75	45	23.33	65	38.16
6	3.17	26	13.26	46	23.90	66	39.01
7	3.69	27	13.76	47	24.52	67	39.83
8	4.20	28	14.26	48	25.12	68	40.62
9	4.70	29	14.77	49	25.75	69	41.40
10	5.20	30	15.28	50	26.39	70	42.15
11	5.71	31	15.78	51	27.04	71	42.87
12	6.21	32	16.30	52	27.71	72	43.58
13	6.72	33	16.80	53	28.40	73	44.28
14	7.22	34	17.33	54	29.10	74	44.96
15	7.72	35	17.84	55	29.83	75	45.63
16	8.23	36	18.36	56	30.58	76	46.30
17	8.73	37	18.90	57	31.36	77	46.96
18	9.24	38	19.41	58	32.15	78	47.62
19	9.74	39	19.97	59	32.97	79	48.28
20	10.24	40	20.48	60	33.82	80	48.94
Minimum spacing: 0.50λ				Maximum spacing: 0.88λ			

Table 9: Subarray parameters of the array of example D, synthesized for elements with element factor $cos^2(h_{20}\theta)$.

Subarray number, r	**Between-ring spacing, $d_r(\lambda)$**	**Number of rings, N_r**	**Distance of the outer rim of the subarray from the centre, $L_r(\lambda)$**
1	0.504	26	13.12
2	0.527	9	17.86
3	0.573	9	23.01
4	0.654	8	28.24
5	0.767	7	33.61
6	0.878	10	42.40
7	0.718	8	48.15
8	0.615	3	50.00

Table 10: Ring radii of the 80-ring density-tapered array described in Table 9.

Ring	$\rho_m(\lambda)$	**Ring**	$\rho_m(\lambda)$	**Ring**	$\rho_m(\lambda)$	**Ring**	$\rho_m(\lambda)$
1	0.50	21	10.59	41	21.30	61	35.37
2	1.01	22	11.10	42	21.87	62	36.25
3	1.51	23	11.60	43	22.44	63	37.13
4	2.02	24	12.11	44	23.02	64	38.01
5	2.52	25	12.61	45	23.67	65	38.89
6	3.03	26	13.12	46	24.32	66	39.77
7	3.53	27	13.64	47	24.98	67	40.65
8	4.04	28	14.17	48	25.63	68	41.52
9	4.54	29	14.70	49	26.28	69	42.40
10	5.05	30	15.23	50	26.94	70	43.12
11	5.55	31	15.75	51	27.59	71	43.84
12	6.05	32	16.28	52	28.25	72	44.56
13	6.56	33	16.81	53	29.01	73	45.28
14	7.06	34	17.33	54	29.78	74	46.00
15	7.57	35	17.86	55	30.55	75	46.71
16	8.07	36	18.43	56	31.32	76	47.43
17	8.58	37	19.01	57	32.08	77	48.15
18	9.08	38	19.58	58	32.85	78	48.77
19	9.59	39	20.15	59	33.62	79	49.38
20	10.09	40	20.73	60	34.50	80	50.00
Minimum spacing: 0.50λ				Maximum spacing: 0.88λ			

Table 11: Performance of the array of Table 10 when the main beam is scanned to (θ_0,0°).

$\boldsymbol{\theta_0}$(°)	Directivity ($\boldsymbol{dBi}$)	SLL[a] ($\boldsymbol{dB}$)	$\boldsymbol{RMS^b_{10}}$	$\boldsymbol{RMS^b_{vis}}$
0	49.8	-25.5	0.3	3.3
5	49.6	-25.5	0.3	4.4
10	49.4	-25.4	0.4	5.7
15	49.0	-25.3	0.6	7.3
20	48.5	-25.4	0.9	9.4

[a] SLL in the whole visible region and in ($\theta_0 - 10°$,$\theta_0 + 10°$).
[b] RMS_{10} and RMS_{vis} defined as in Table 6.

References

[1] Aarón Ángel Salas-Sánchez, Juan Antonio Rodríguez-González, Eduardo Moreno-Piquero, and Francisco José Ares-Pena, 'Synthesis of Taylor-like patterns with uniformly excited multi-ring planar antennas,' *IEEE Trans. Antennas and Propag.*, vol. 62, no. 4, pp. 1589-1595, Apr. 2014.

[2] M. Vicente-Lozano, F. Ares-Pena, and E. Moreno, "Pencil-beam pattern synthesis with a uniformly excited multi-ring planar antenna," *IEEE Antennas Propag. Mag.*, vol. 42, no. 6, pp. 70–74, Dec. 2000.

[3] T. A. Milligan, "Space-tapered circular (ring) array," *IEEE Antennas Propag. Mag.*, vol. 46, no. 3, pp. 70–73, Jun. 2004.

[4] R. L. Haupt, "Optimized element spacing for low sidelobe concentric ring arrays," *IEEE Trans. Antennas Propag.*, vol. 56, no. 1, pp. 266–268, Jan. 2008.

[5] W. Doyle, "On approximating linear array factors," RAND Corp. Memorandum RM-3530-PR, Feb. 1963.

[6] M. I. Skolnik, "Nonuniform arrays," in Antenna Theory, Part I, R. E. Collin, Ed., F. J. Zucker, Ed. New York, NY, USA: McGraw-Hill, 1969.

[7] T. T. Taylor, "Design of circular apertures for narrow beamwidth and low sidelobes," *IRE Trans. Antennas Propag.*, vol. AP-8, no. 1, pp. 17–22, Jan. 1960.

[8] D. Bianchi, S. Genovesi, and A. Monorchio, "Constrained Pareto optimization of wide band and steerable concentric ring arrays," *IEEE Trans. Antennas Propag.*, vol. 60, no. 7, pp. 3195–3204, Jul. 2012.

[9] A. Trucco, "Thinning and weighting of large planar arrays by simulated annealing," *IEEE Trans. Ultrason. Ferroelect. Freq. Control*, vol. 46, no. 2, pp. 347–355, Mar. 1999.

[10] O. M. Bucci, T. Isernia, and A. F. Morabito, "A deterministic approach to the synthesis of pencil beams through planar thinned arrays," *Progress in Electromagn. Res.*, vol. PIER 101, pp. 217–230, 2010.

[11] M. C. Viganó, G. Toso, G. Caille, C. Mangenot, and I. E. Lager, "Sunflower array antenna with adjustable density taper," *Int. J. Antennas Propag.*, vol. 2009, 10.1155/2009/624035, Article ID 624035.

[12] W. H. Press, W. T. Vetterling, S. A. Teukolsky, and B. P. Flannery, Numerical Recipes in C, 2nd ed. Cambridge, U.K.: Cambridge Univ. Press, 1992.

[13] M. Álvarez-Folgueiras, J. A. Rodríguez-González, and F. Ares-Pena, "High-performance uniformly excited linear and planar arrays based on linear semiarrays composed of subarrays with different uniform spacings," *IEEE Trans. Antennas Propag.*, vol. 57, no. 12, pp. 4002–4006, Dec. 2009.

[14] ESA/ESTEC Tender AO/1-559808/NL/ST, Innovative architectures for reducing the number of controls of multiple beam telecommunication antennas.

[15] O. M. Bucci, T. Isernia, and A. F. Morabito, "Optimal synthesis of directivity constrained pencil beams by means of circularly symmetric aperture fields," *IEEE Antennas Wireless Propag. Lett.*, vol. 8, pp. 1386–1389, 2009.

3 Parametric synthesis of isophoric pencil beam and phase-shaped flat-topped beams

Interest in uniformly illuminated (isophoric) density-tapered planar antenna arrays has recently revived. For arrays consisting of concentric rings of elements, we present a non-stochastic algorithm that calculates ring radii for generation of pencil beams without the need for prior specification of the number of rings. If element phases are allowed to differ, the algorithm also synthesizes density-tapered arrays generating axially symmetric shaped footprint beams (to which the usual distortion methods can be applied to obtain beams with other contour shapes). Along this chapter, the use of the algorithm is illustrated by application to multibeam coverage of the Earth and to circular, elliptic and square footprint beams; in the multibeam case, the use of its results as the starting point of a stochastic optimization has greatly assisted the solution of a recalcitrant synthesis problem. This work is reflected in [1] and [2].

3.1 Introduction

The advantages and disadvantages of uniformly excited, nonuniformly spaced array antennas, in comparison with uniform spacing and nonuniform excitation, have long been known [3]. For a given antenna size, the use of uniformly excited nonuniformly spaced elements to generate sum or pencil beams can typically reduce weight, cost and feed network complexity, and increase average element efficiency, at the expense of a reduction in directivity due mainly to high wide-angle sidelobes [4, 5]. The reductions in weight and cost derive from the use of fewer elements than in a uniformly spaced array, the increased average element efficiency from the use of all elements at maximum power, and the reduction in feed network complexity from both these factors. Beamwidth is in general hardly affected, because it depends mainly on the physical size of the array rather than the number of elements. Bandwidth and scanning range are generally improved due to the absence of true grating lobes.

Although best results for a given target radiation pattern are nowadays, in most cases, probably obtained using stochastic optimization methods to determine the element positions [6], it is often desirable or necessary to employ a computationally less costly technique. The traditional deterministic approach, analysed by Doyle for the linear array case [7], has been to synthesize a continuous aperture that generates a satisfactory radiation pattern; divide the aperture into as many portions as the intended number of antenna elements, N, in such a way that, in a plot of the aperture distribution, the area or volume over each portion is the same; and place the N elements at the centroids of the portions with respect to the distribution. Hybrid methods that combine stochastic techniques with a version of this traditional deterministic approach have also been proposed [8].

For linear arrays the traditional deterministic approach is straightforward and

unambiguous; for planar arrays its implementations may vary considerably, basically because of freedom to choose the shapes of the aperture portions. This is so even in the case of arrays consisting essentially of concentric rings of elements, with the elements on each ring equispaced so as to afford an essentially axisymmetric pattern: Willey, for example, fixes the ring radii and varies the azimuthal width of the portions [9], while Milligan varies ring radii while using an azimuthal portion width that approximates a pre-imposed function of ring radius [10]. Other portion shapes result when elements are placed differently, e.g. on a spiral [11].

Both Willey and Milligan use a predetermined number of rings, while Bucci and Perna [12] use a predetermined total number of elements. Here we describe a modification of Milligan's method that requires prespecification of neither the number of rings nor the total number of elements, and a generalization in which element phases are allowed to vary, which permits the synthesis of density-tapered isophoric antennas generating flat-topped or otherwise-shaped beams. We illustrate their use by several examples, including flat-topped beams (distorted to have elliptical and square contours) and multibeam coverage of the Earth. In this latter case, using as the deterministically synthesized array as the starting point of a stochastic optimization has greatly assisted the solution of the recalcitrant synthesis problem posed by the reported specifications of two European Space Agency (ESA) tenders [13].

3.2 Method

We consider arrays consisting of concentric rings of elements, the number M and radii $r_1, \ldots, r_M$ of which are to be determined. The array radius a is given, as is an axially symmetric continuous excitation density $I(r)$ for a circular aperture of the same radius - the model to be approximated. The number of elements with their centre on a ring of radius r, $n(r)$, is an initially prefixed function, and the elements are equispaced, making the distance between their centres

$$d(r) = 2r \sin[\pi/n(r)] \tag{32}$$

For example, if the elements are to be packed as closely as possible on each ring while respecting a specified minimum distance $d_0(r)$ between their centres, then

$$n(r) = \left\lfloor \frac{\pi}{\arcsin\left(\frac{d_0(r)}{2r}\right)} \right\rfloor \tag{33}$$

where $\lfloor . \rfloor$ indicates the floor function. We assume, in fact, that the size of the elements and/or the need to minimize their mutual coupling imposes a requirement that both $d(r)$ and the radial distance between rings be greater than a specified minimum, d_{min}, but $d_0(r)$ may be greater than d_{min} and may vary with r.

In the spirit of Milligan [10], we consider a radial density-per-element

$$y(r) = \frac{2\pi r I(r)}{n(r)} \tag{34}$$

(constructed by integrating $I(r)$ around a circumference and dividing by the appropriate number of elements) and the corresponding cumulative distribution

$$Y(r) = \int_0^r y(\rho) d\rho \tag{35}$$

Once M is known, we shall partition the antenna into M annuli with boundaries $0 = s_0, s_1, \ldots, s_M = a$ such that the excitation per element is the same in each annulus (and hence in the whole antenna), i.e.

$$Y(s_m) - Y(s_{m-1}) = Y(a)/M \quad \forall m \in 1, \ldots, M \tag{36}$$

and we shall define the ring radii r_m to be such that

$$Y(r_m) = 1/2[Y(s_{m-1}) + Y(s_m)] \tag{37}$$

(see Fig. 13). This ensures that $Y(r)$ is approximated as closely as possible (for given M) by the staircase function $s(r) = m(r)Y(a)/M$, where $m(r)$ is the integer m for which $Y(s_m)$ is closest to $Y(r)$ [7]. By an extension of Doyle's analysis in [7] it may be shown that this in turn leads to the radiation pattern $F(u)$ of the array ($u = \sin\theta$), where θ is the angle from boresight) being the best weighted least squares approximation to that of the continuous distribution modelled, with weighting $1/u^2$.

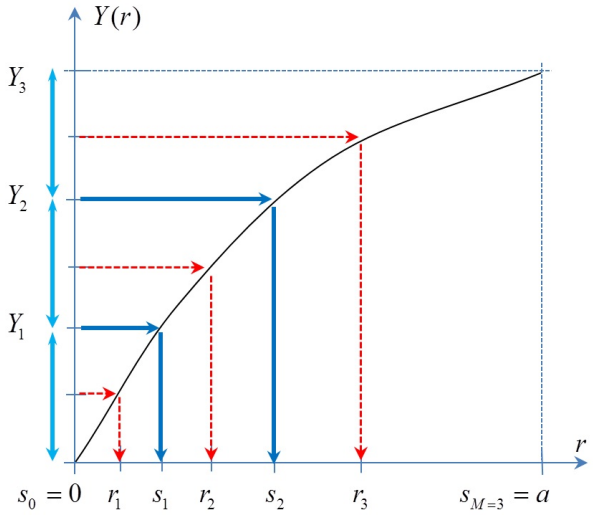

Figure 13: Schematic showing how, for a three-ring array, annuli and ring radii are determined by dividing the maximum value of the cumulative function $Y(r)$ into equal parts. For brevity, $Y(s_i)$ is here indicated as Y_i.

It is clear that the greater M is, the better will $s(r)$ approximate $Y(r)$; that M cannot exceed a/d_{min}; and that M also depends on $d_0(r)$ and the behaviour of $Y(r)$. Assuming for simplicity that $d_0(r) = d_{min}$, if $Y(r)$ were as in Fig. 13, with a smooth derivative $y(r)$, then since the annuli are narrowest where $Y(r)$ increases most steeply and $y(r)$ attains its maximum (y_{max}), the increase in Y due to the limiting annulus would be approximately $d_{min}y_{max}^2$; and since, by (36), the increase in Y due to any annulus is the same ($Y(a)/M$), then

$$M = \left\lfloor \frac{Y(a)}{d_{min}y_{max}} \right\rfloor \tag{38}$$

However, $y(r)$ is generally not smooth. For example, assuming once more that $d_0(r) = d_{min}$, and with $n(r)$ defined as in (33), $y(r)$ oscillates rapidly and with discontinuities due to $n(r)$ increasing discontinuously by one unit at intervals smaller than about $d_{min}/6$. This oscillation is of course especially pronounced in the small-r region, as is illustrated in Fig. 14, which shows $d(r)$, $y(r)$ and $I(r)$ for an antenna of radius 60λ when a) $d_{min} = 0.5\lambda$ and $I(r)$ is a circular Taylor density with nominal sidelobe level $SLL = -20dB$ and null-control parameter $\bar{n} = 9$; and b) $d_{min} = 3\lambda$ and $I(r)$ is a Gaussian distribution [14] with $\rho = 1.0693$. Note that the marked edge-brightening of $I(r)$ in Fig. 14.A, which increases with $\bar{n}$ and jeopardizes the realizability of the corresponding amplitude-tapered array (by both complicating the array feed network and favoring mutual coupling), is of no concern for a density-tapered array, at least when all elements are in phase. On the contrary, so long as $\bar{n}$ is not so large as to cause phase inversion, moderate-to-large values of $\bar{n}$ are preferable so as to maximize directivity.

In the case of Fig. 14.A the oscillation of $y(r)$ in the small-r region causes no problem: $y(r)$ attains its maximum near the edge of the antenna, where oscillation is minimal, so there is no difficulty in determining y_{max} for use in (38). The situation is different in the case of Fig. 14.B, in which $y(r)$ oscillates widely in the region where it peaks, with a period that is only a fraction of d_{min} and which therefore makes it impossible to use $d_{min}y_{max}$ to estimate the increase in $Y(r)$ over the width of the limiting annulus. One solution might be to integrate $y(r)$ over an interval of width d_{min} around its peak and use this result instead of $d_{min}y_{max}$ in (38). However, with this strategy there arise questions about the integration interval and other issues, and it is simpler to take the following clumsier but nonetheless effective approach. As a surrogate for y_{max} in (38) we use the value of $y(r)$ at the smallest value of r for which $d(r) = d_{min}$. This will overestimate M, with the result that there will be between-ring distances smaller than d_{min}, so we iteratively decrement M until the d_{min} condition is fulfilled.

If to achieve shaped beams by filling nulls it is necessary for $I(r)$ to be complex, its modulus, $|I(r)|$, is used in (34) to obtain $y(r)$. M and the ring radii are then computed for this $y(r)$, and the phases of the elements are set to the phases of $I(r)$ at their positions. This simple combination of a uniform amplitude with the phase of a continuous distribution of non-uniform amplitude has previously been employed by

Trastoy-Ríos et al. [15] (during optimization of the continuous distribution) and by *Bucci et al.* [16].

If further refinement of the synthesized array is required, the ring radii (and/or element phases) may be subjected to an appropriate optimization procedure. The advantage of using the deterministically synthesized array as the starting point of such optimization is illustrated in section 3.4 below.

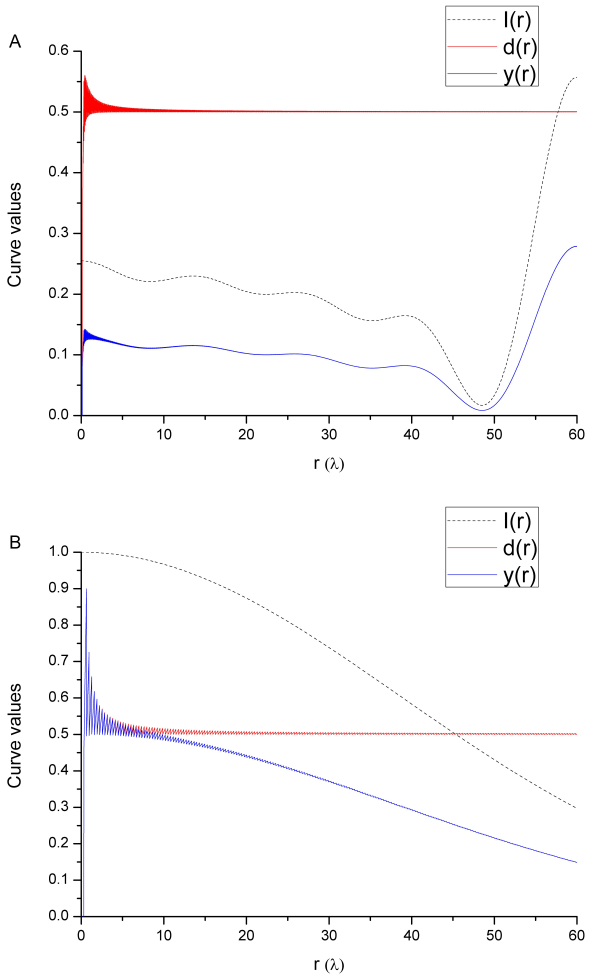

Figure 14: Examples of how maintenance of a minimum distance d_{min} between the elements in a ring introduces oscillation in the radial density-per-element function $y(r)$. A) $d_{min} = 0.5\lambda$, $I(r)$ a circular Taylor density with nominal $SLL = -20\ dB$ and $\bar{n} = 9$. B) $d_{min} = 3\lambda$, $I(r)$ a circular Gaussian distribution [14] with $\rho = 1.0693$

3.3 Examples

3.3.1 Pencil beams

High-performance pencil beams may be obtained starting from a Taylor distribution as $I(r)$. With $a = 60\lambda$ and $d_0(r) = d_{min} = 0.5\lambda$, and assuming isotropic radiating elements, using $-30dB$ Taylor distributions with $\bar{n} = 9 - 20$ affords power patterns with peak directivities of $45.0 - 46.7dBi$ and side lobe levels ranging from -30.0 to $-30.2dB$. Figs. 15.A and 15.B compare the power pattern achieved with $\bar{n} = 18$, which has best peak directivity, with the model Taylor pattern. The array in this case has $19,376$ elements arranged in 62 rings with between-ring spacings ranging from 0.50λ to 5.00λ. The half-power semi-beamwidth is $0.262°$, and the aperture efficiency 97.8% (cf. 78.9% for the continuous Taylor distribution used as $I(r)$, or 88.4% for the most efficient $-30dB$ continuous Taylor distribution ($\bar{n} = 8$), which has a peak directivity of only $46.2dBi$). The side lobes rising above the Taylor pattern in directions greater than about 25° from the beam centre, an effect typical of density-tapered arrays, never exceed $-39dB$. Interestingly, the beam can be scanned to very wide angles without any appreciable loss of performance. When scanned to 60λ (Fig. 16), the sidelobe level rises just $0.1dB$, and although peak directivity falls from 46.7 to $45.4dBi$, the directivity at the *edge* of the beam actually rises: at the edge of coverage in the ESA tender example considered below, 0.325° from beam centre, the directivity rises from 42.0 to $44.3dBi$.

A 19,376-element array is of course complicated to produce; like other authors [17–19], we present results for such a large array more as an illustration of the theoretical potential of our technique than as a practical proposal. However, a very much smaller array can be achieved, albeit at the expense of raising the side lobes a few dB, by using directive elements (which are larger, and therefore make d_{min} larger) and/or a $d_0(r)$ that increases with r. For example, with a $cos^{19}(\theta)$ element pattern corresponding to $d_{min} = 3\lambda$ (see below), varying the Taylor parameters (nominal $SLL = -35dB$, $\bar{n} = 13$) leads to a 585-element antenna producing a pattern with a peak directivity of $46.5dBi$, a sidelobe level of $-26.2dB$, and an aperture efficiency of 86.0% (Fig. 17). These performance figures can be compared with those of $I(r)$, the most efficient $-35dB$ Taylor distribution (peak directivity $50.7dBi$, aperture efficiency 82.1%); or with the results of sampling $I(r)$ onto an array of 1257 3λ, $cos^{19}(\theta)$ elements packed as tightly as possible on 20 rings 3λ apart (peak directivity $49.0dBi$, sidelobe level $-33.5dB$, aperture efficiency 70.7%). Scanning the beam 8° (as required for coverage of the edge of Earth by a GEO satellite with an antenna pointing at the Equator) lowers the peak directivity to $45.0dBi$ while raising the sidelobe level to $-22.4dB$.

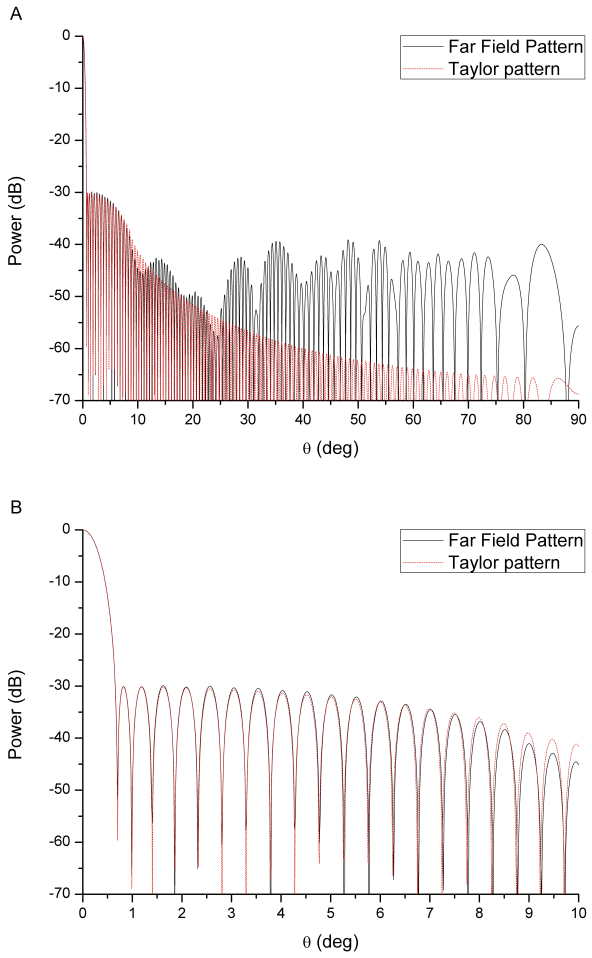

Figure 15: A) Power pattern of an array of 19376-elements arranged in 62 rings, together with the $-30\ dB$, $\bar{n} = 18$ Taylor pattern corresponding to $I(r)$. B) Detail of (A).

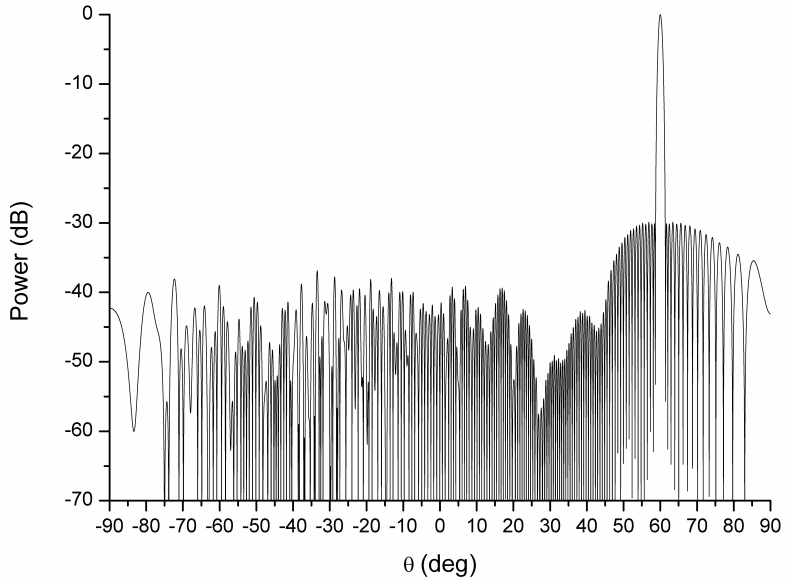

Figure 16: Power pattern obtained when the beam in Fig. 15.A is scanned 60°.

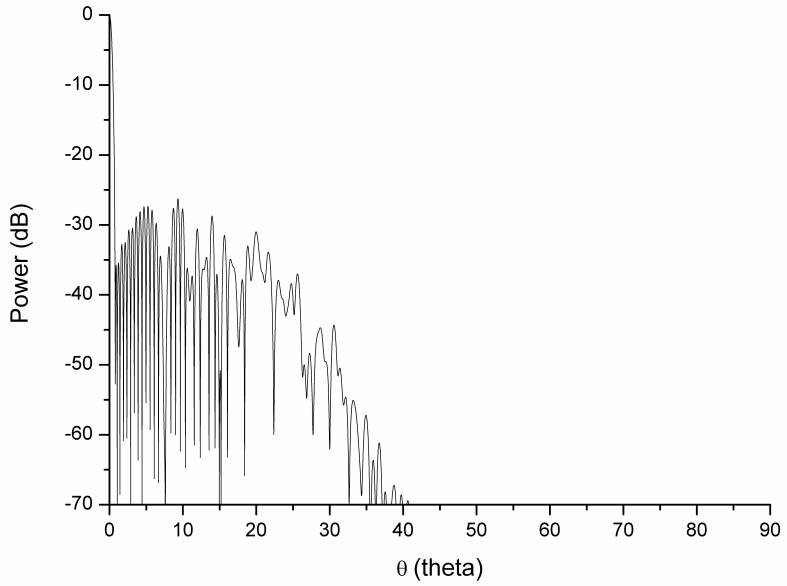

Figure 17: Pencil beam with a peak directivity of 46.5 dB and a sidelobe level of -26.0 dB generated by an array of 585 elements with $cos^{19}(\theta)$ patterns.

3.4 Application to a Multibeam spot coverage scenario

ESA/ESTEC tenders AO/1-5598/08/NL/ST and AO/1-6338/09/NL/JD, concerning an isophoric array with a radius of up to 60λ without restriction in the number of elements, reportedly require coverage of the Earth by pencil beams of two frequencies and both polarities such that a) the directivity D_{EOC} at the edge of coverage (EOC, 0.325° from beam centre) is at least $43.8dB$ for the central (unscanned) beam, and b) the off-coverage directivity relative to D_{EOC} (D_{off}) is no higher than $-10dB$ outside the Earth and no higher than $-20dB$ in the areas covered by beams of the same frequency and polarity, the nearest of which is 0.795° from beam centre [12, 13]. An analysis of the pseudo-grating-lobe effect suggests that for this problem an element diameter of about 3λ is appropriate [20], and we accordingly set d_{min} to this value, as also $d_0(r)$, and took as our elements circular horns of this diameter, for which the element pattern is of the form $cos^{19}(\theta)$ according to customary criteria [21]. Note that contact between elements should give rise to no significant mutual coupling problems for horns of this size [22].

For this problem, we obtained best results with the circular Gaussian distribution [14]:

$$I(r) = e^{-\rho\left(\frac{r}{a}\right)^2} \quad |r| \leq a \tag{39}$$

For each distribution radius a considered, an optimal value of the parameter ρ was identified in the interval $0.0 \leq \rho \leq 4.0$. As in similar cases [19], a wide antenna was not always an advantage: at the expense of a $0.5dBi$ drop in D_{EOC}, an antenna of radius 44λ, obtained from a distribution radius a of 47λ, satisfied the off-coverage directivity requirements using 418 elements, 250 fewer than in the 55λ antenna that gave best results for a distribution radius of 60λ (Table 12). Further reduction was achieved by setting $d_0(r) = 3.3\lambda$ instead of 3λ, which lowered D_{EOC} another $0.4dBi$ but reduced the required number of elements to 380 (Table 12, Table 13, and Figs. 18, 19 and 20).

Table 12: Results obtained for the ESA Tender example by the deterministic method[a].

a $(\lambda)^b$	ρ	b $(\lambda)^c$	# rings	# elements	Scan (°)	D_{EOC} (dBi)	D_{off} On Earth[d]	D_{off} Off Earth	η
47	1.0693	44	10	418	0	42.5	-20.3	-21.1	16.3
					8	41.1	-20.0	-17.0	14.9
60	1.2878	55	14	668	0	43.0	-20.8	-23.2	14.8
					8	41.6	-20.1	-17.5	13.4
47	1.0756	44	10	380	0	42.1	-20.5	-19.1	16.3
					8	40.7	-20.1	-11.8	14.9

[a]In all cases, radiating elements have radius 3λ and element pattern $cos^{19}(\theta)$. $d_0(r)$ is 3λ for the 418− and 668−element arrays, and 3.3λ for the 380−element array. [b]Radius of the model distribution. [c]$b = r_M + 1.5$, the actual radius of the density-tapered antenna. [d]On Earth, further than 0.795° from beam centre.

Table 13: Ring radii of the 380-Element Array of Table 12

Ring number (m)	Radius $r_m(\lambda)$	# Elements
1	2.912	5
2	6.245	11
3	9.552	18
4	12.863	24
5	16.313	31
6	20.640	39
7	25.748	48
8	29.853	56
9	35.727	67
10	42.564	81

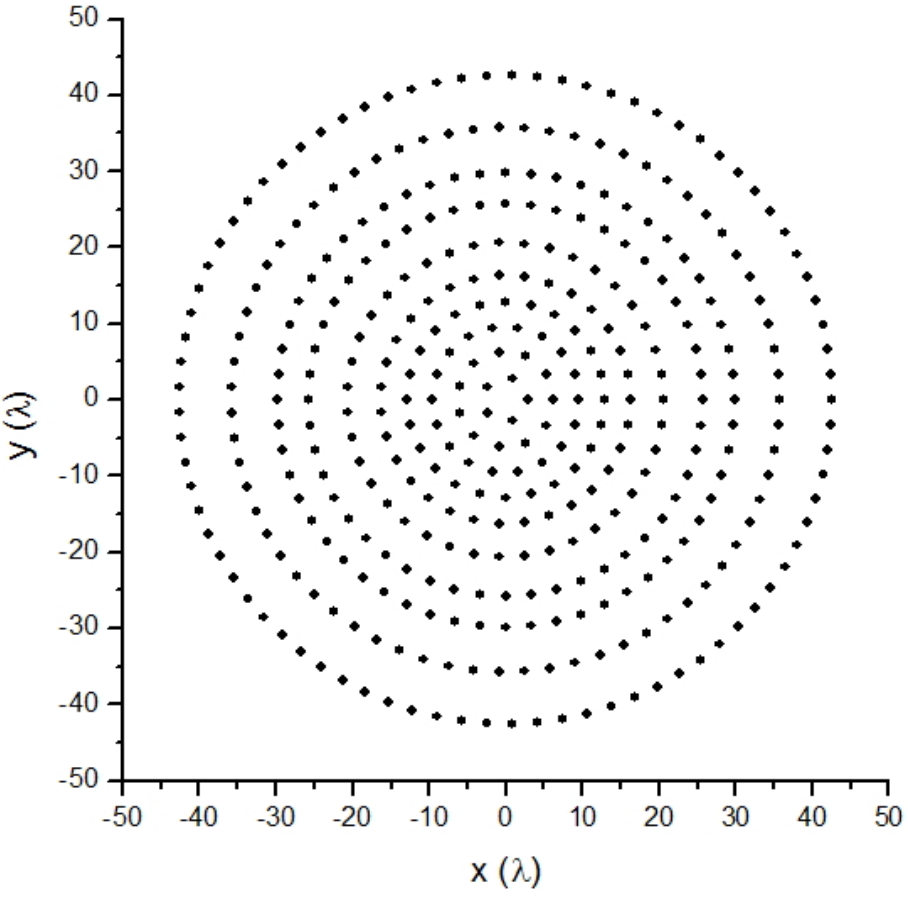

Figure 18: Arrangement of the elements for the 380-element isophoric array of Table 13 (element diameter 3λ, element factor $\cos^{19}\theta$ and $d_0(r) = 3.3\lambda$).

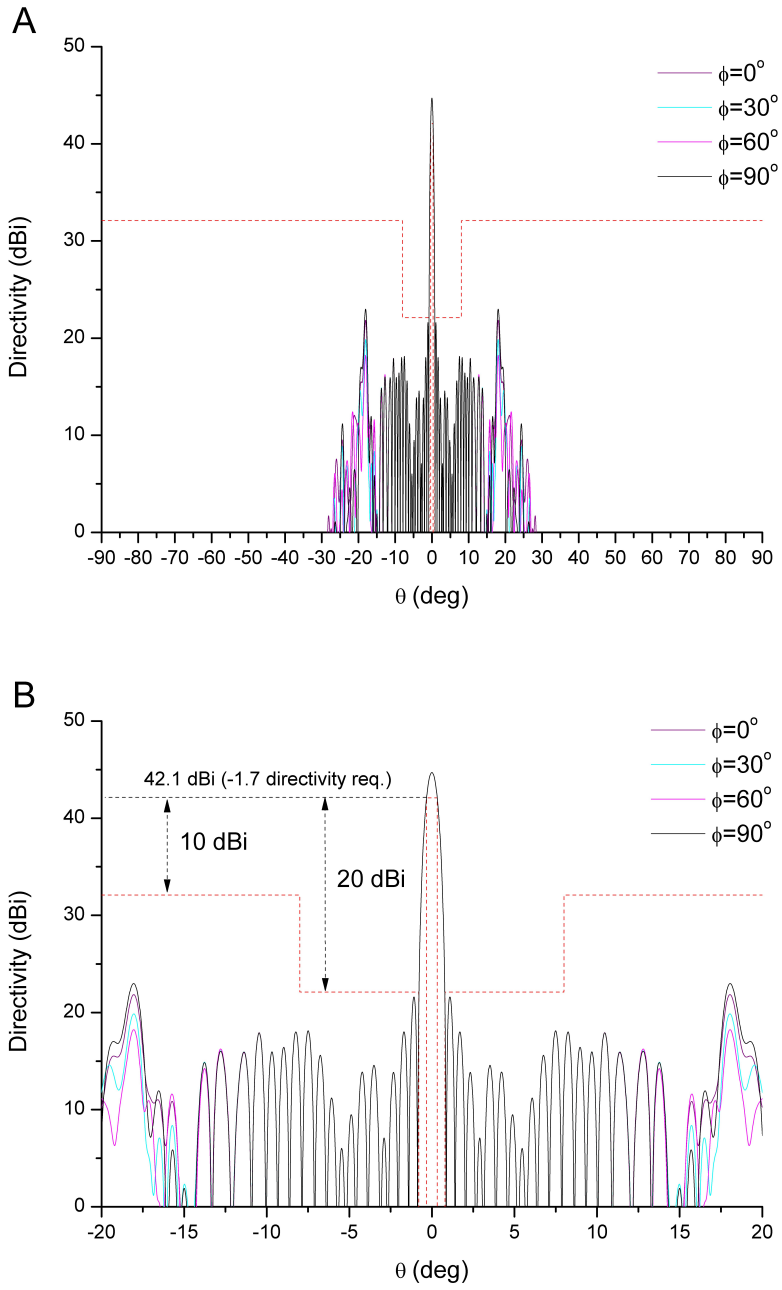

Figure 19: A) Power pattern in several ϕ cuts for the 380-element isophoric array of Table 13. B) Detail of A)

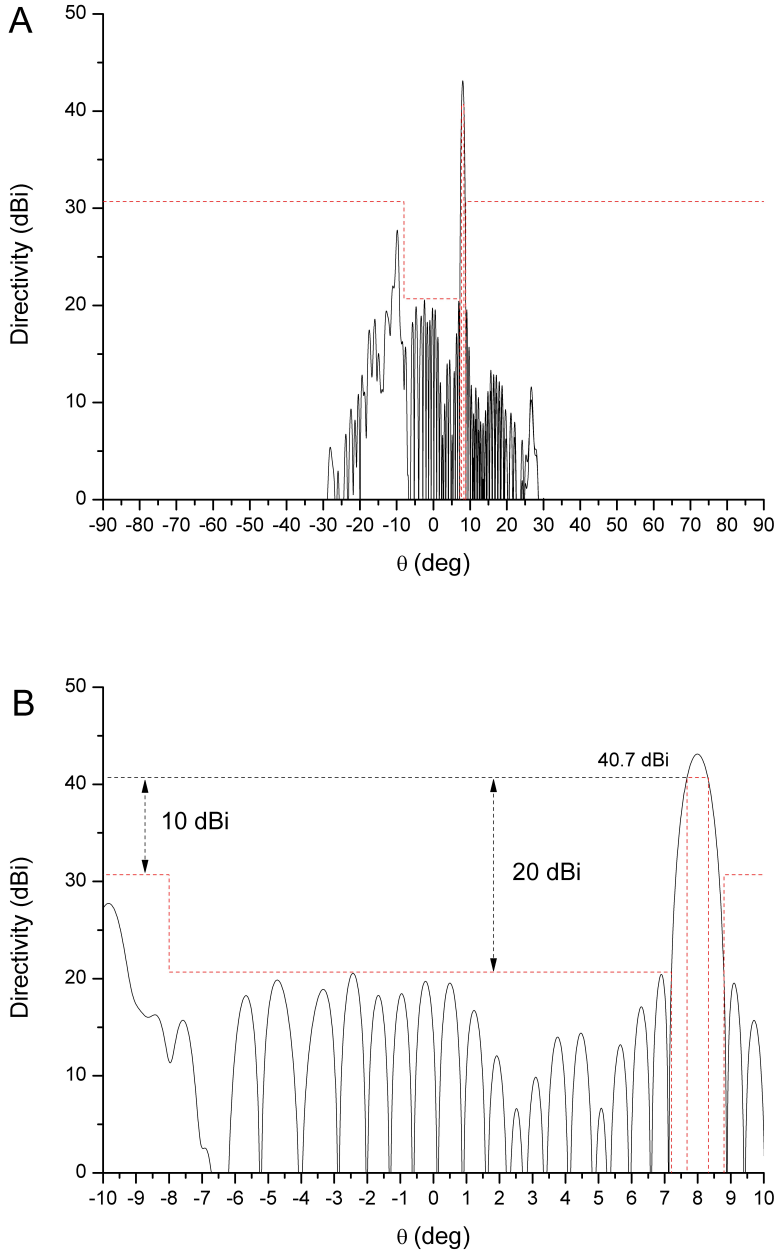

Figure 20: A) Power pattern ($\phi = 0°$) of the 380-element isophoric array of Table 13 when scanned 8°. B) Detail of A)

The aperture efficiency pertinent to this problem relates the theoretical maximum efficiency to the directivity at the *EOC* rather than the directivity at the peak of the main beam; except for a constant term that depends only on the diameter of the elements, its

logarithmic version is the quantity η introduced by *Bucci et al.* [20]:

$$\eta = D_{EOC} - 10log_{10}N \tag{40}$$

where N is the number of elements in the array. The values of η of the solutions described above are listed in Table 12.

The best solution obtained by the authors from whom we took this problem was an antenna with 368 3λ elements that achieved a D_{EOC} of $42.6dBi$ unscanned and $40.6dBi$ when scanned 8°; η was 16.94 unscanned and 14.9 scanned 8° [20] (cf. the D_{EOC}s of 42.1/40.7 and 42.5/41.1, with η's of 16.3/14.9, for the 44λ antennas of Table 12). However, this solution was arrived at by means of a hybrid method involving both deterministic calculations and stochastic optimization, and required a non-standard highly directive element. The *EOC* directivity required by the reported ESA specifications is provided neither by any of the solutions described in [20] nor by any obtained in the present work by the direct density-tapering method of section 3.2.

To investigate whether the ESA tender problem was in fact soluble, or whether, on the contrary, its specifications had been unrealistically optimistic, we sought a solution by stochastic optimization, using simulated annealing [24] to optimize the ring radii of arrays with the same elements, dmin, $d_0(r)$ and numbers of rings, and the same model distributions, as are listed in Table 12. The cost function C employed was

$$C = \Delta^2_{D_{EOC}} H(-\Delta_{D_{EOC}}) + \Delta^2_{D_{off,1}} H(\Delta_{D_{off,1}}) + \Delta^2_{D_{off,2}} H(\Delta_{D_{off,2}}) \tag{41}$$

where H is the Heaviside step function, $D_{off,1}$ is the maximum directivity on Earth but further than 0.795° from beam centre, $D_{off,2}$ is the maximum off-coverage directivity off Earth, and $\Delta_\alpha = \alpha - \alpha^d$ for $\alpha = D_{EOC}$, $D_{off,1}$ and $D_{off,2}$, where α^d is the limiting acceptable value of the quantity α. Although the ESA-specified values of D^d_{EOC}, $D^d_{off,1}$ and $D^d_{off,2}$ are respectively $43.8dBi$, $-20dB$ and $-10dB$, we actually used values of $44.0dBi$, $-20.5dB$ and $-10.5dB$ in order to favour achievement of an acceptable solution.

In the optimization procedure, simulated annealing introduces small perturbations (δr_m) to the rings obtained from the deterministic solution (r^0_m) of Table 12. In order to guarantee the constraint of a minimum spacing between rings of d_0, the radius of the m-ring is calculated as follows:

$$r_m = \begin{cases} r^0_m + \delta r_m & if \quad r^0_m + \delta r_m - r_{m-1} \geq d_0(r) \\ \\ r_{m-1} + d_0(r) & otherwise \end{cases} \tag{42}$$

where $r_0 = d_0/2$.

For neither of the small antennas of table 12 did optimization achieve the desired result. Starting from the deterministic solutions, the D_{off} specifications were met but

D_{EOC} improved only an insufficient $0.5dBi$, presumably because the model distribution is too small and/or 10 rings can house too few radiating elements. When starting with the rings in *close-packed* configuration ($r_m = [m - 1/2]d_0$), neither the D_{EOC} nor the D_{off} specifications were met. However, for the large array, starting from the deterministic solution summarized in Table 12, the algorithm converged to the solution described in Tables 14, 15, and Figs. 21, 22 and 23. This solution completely satisfies the reported ESA specifications. Because of the heavy burden of the directivity computations required by the cost function, convergence required some 4 hours on a PC with an Intel Core i5-4570 processor running at 3.2 GHz. For this 14-ring array the optimization algorithm also achieved a satisfactory solution starting from the close-packed configuration, but needed more than 24 hours to do so. Since in both cases prior knowledge of an appropriate number of rings was required, the preliminary, rapid acquisition of the deterministic solution was well worth while.

Obviously, the challenge would be synthesize an antenna that verifies the ESA requirements by using a minimal number of feeds (circular horns). We are considering a new approach based on adding a new degree of freedom in the synthesis process: the excitation phase of each one of them. Because beam-steering phase shifters are already part of the antenna, in order to proceed with the beam scanning process, it does not complicate the feeding network.

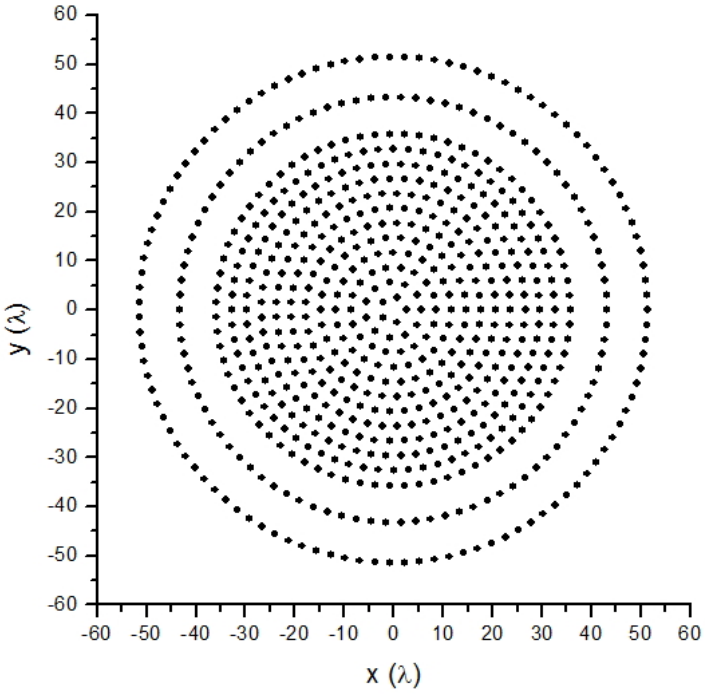

Figure 21: Arrangement of the elements for the 674-element isophoric array of Table 14 (element diameter 3λ, element factor $\cos^{19}\theta$ and $d_0(r) = 3\lambda$).

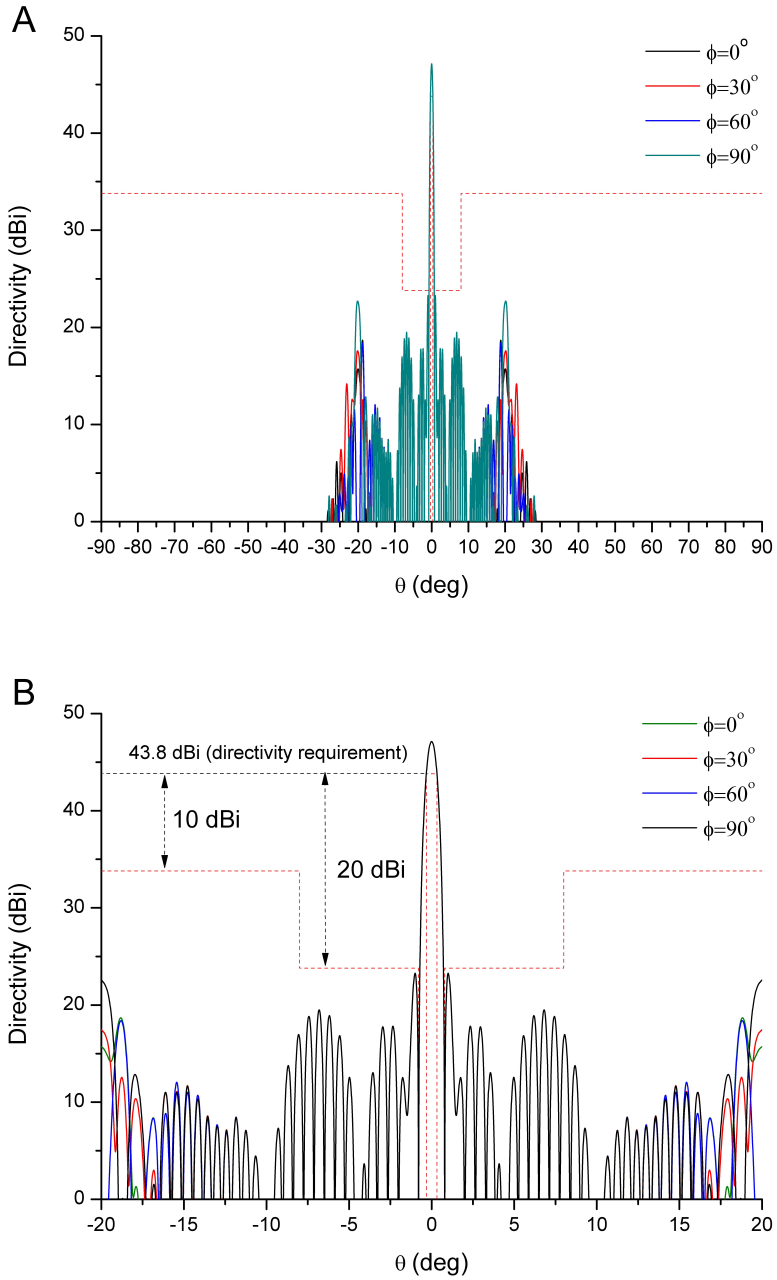

Figure 22: A) Power pattern in several ϕ cuts for the 380-element isophoric array of Table 13. B) Detail of A)

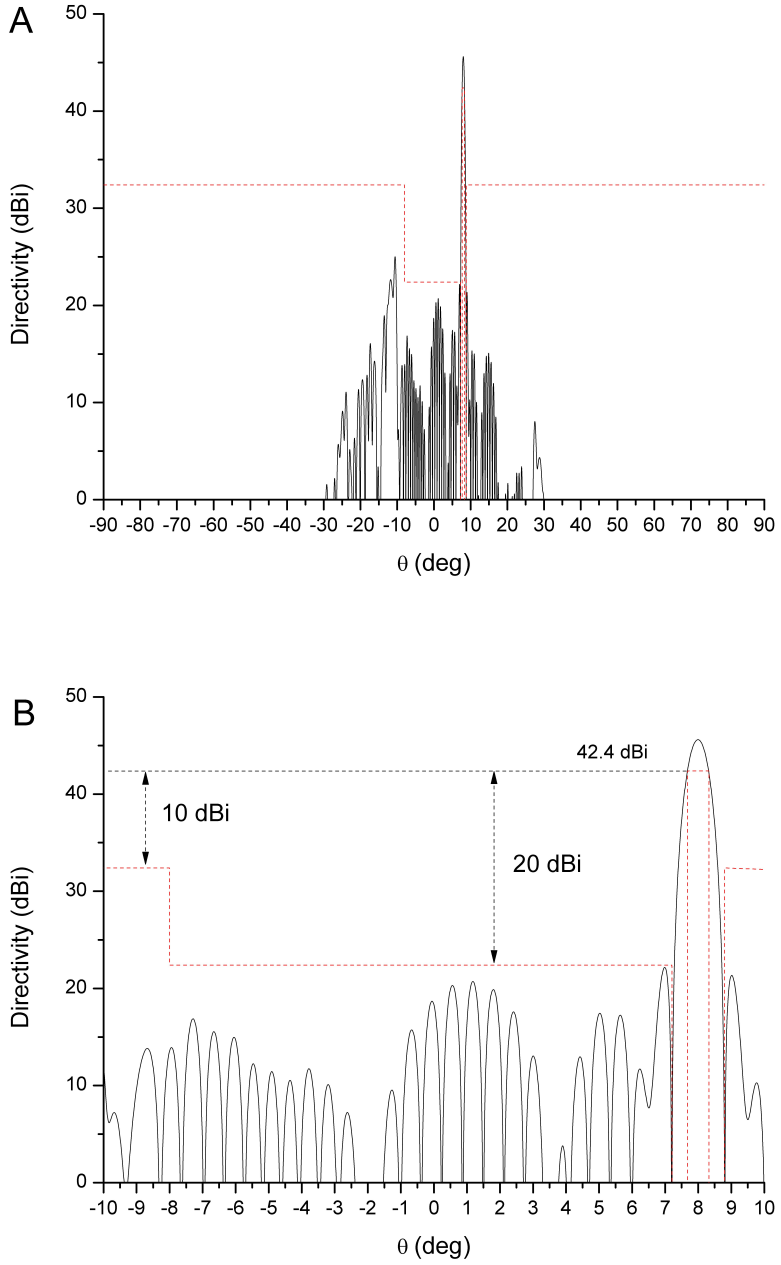

Figure 23: A) Power pattern ($\phi = 0°$) of the 380-element isophoric array of Table 13 when scanned 8°. B) Detail of A)

Table 14: Results obtained for the ESA Tender example by simulated annealing, starting from the deterministic solution[a].

b $(\lambda)^b$	d_0 $(\lambda)^c$	# rings	# elements	Scan (°)	D_{EOC} (dBi)	D_{off} On Earth[d]	D_{off} Off Earth	η
53	3.0	14	674	0	43.8	-20.6	-24.1	15.5
				8	42.4	-20.3	-16.4	14.1

[a]Radiating elements have radius 3λ and element pattern $\cos^{19}(\theta)$.[b]Radius of the final antenna. [c]Minimum distance between element centres. [d]On Earth further than 0.795° from beam centre.

Table 15: Ring radii of the 674-element array of table 14.

Ring number (m)	Radius $r_m(\lambda)$	# Elements
1	2.623	5
2	5.661	11
3	8.661	18
4	11.664	24
5	14.674	30
6	17.688	37
7	20.688	43
8	23.688	49
9	26.688	55
10	29.690	62
11	32.693	68
12	35.821	75
13	43.231	90
14	51.447	107

3.4.1 Flat-topped shaped beam

Following the theoretical basis shown in section 3.2, the method there described can be used to design uniform-amplitude phased arrays affording shaped beams. The first step is to find a continuous aperture density $I(r)$ generating a suitable flat-topped axisymmetric beam. This can be done by means of an automated version of the Elliott-Stern method [25], starting from an appropriate Taylor pattern. The procedure described in section 3.2 is then applied to $|I(r)|$, and the phases of the elements are set to the phases of $I(r)$ at their locations. Beam contour shaping is then carried out by stretching or shrinking of the distance between each element and the array centre, as in [26], or between each element and the x or y axis, as in [25].

- **Example 1**

As a first example we consider the synthesis of a flat-topped circular beam. We use an antenna of radius 60λ. An analysis of the pseudo-grating-lobe effect suggests that for this problem an element diameter of about 2.2λ is appropriate, and we accordingly took as our elements circular horns of this diameter, for which the element pattern is of the form $cos^{10}\theta$ according to customary criteria [21]. We start from a Taylor pattern with $\bar{n} = 7$ and nominal $SLL = -25\ dB$. The starting aperture distribution, $I(r)$, is obtained by the Elliott-Stern method [25] so as to afford a flat-topped power pattern in which the first side lobe lies at the same level as the main beam, the first null has been filled to $-1\ dB$, and the next five side lobes are held at $-25\ dB$. Application of the procedure described in section 3.2 to $|I(r)|$, and assignment of the element phases as described above, affords a 607-element array generating a circular beam 1.46° wide with a peak directivity of 37.1 dBi, a ripple of 1.2 dB (which guarantees a directivity of at least 35.9 dBi throughout the beam top), and a side lobe level of $-15.8\ dB$ inside the Earth (considering a GEO satellite with an antenna pointing at the Equator) that is reduced to -16.8 outside the Earth. This solution is shown in Table 16 and Figs. 24 and 25.

In order to study the steering capabilities of this antenna, when the beam is scanned to 8°, the minimum directivity throughout the beam top is reduced to 36.1 dBi, while the ripple slightly increases to 1.3 dBi. With this maximum scanning angle, the side lobe level inside the Earth remained practically unaltered ($-15.0\ dB$), whereas outside the Earth is increased to $-12.6\ dB$, see Fig. 26.

Table 16: Ring and phase radii of the 607-element array for the flat-topped circular beam example.

Ring number (m)	Radius $r_m(\lambda)$	Phase ϕ (deg)	# Elements
1	1.959	67.4	5
2	4.240	67.5	11
3	6.579	67.6	18
4	9.008	67.3	24
5	11.599	66.3	30
6	14.478	64.4	37
7	17.870	60.8	43
8	22.226	54.8	49
9	28.908	36.6	55
10	42.136	-59.1	62
11	55.572	-82.8	68

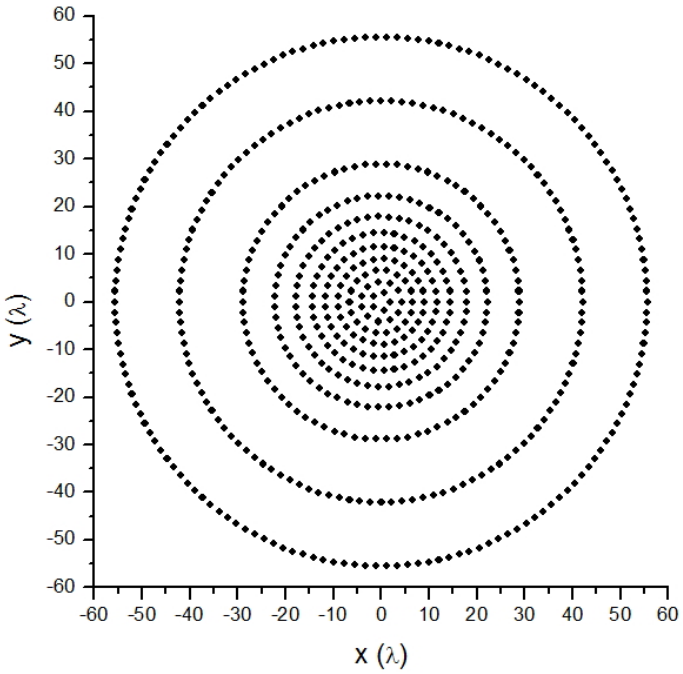

Figure 24: Arrangement of the elements for the 607-element isophoric array of Table 16 (element diameter 2.2λ, element factor $\cos^{10}\theta$.)

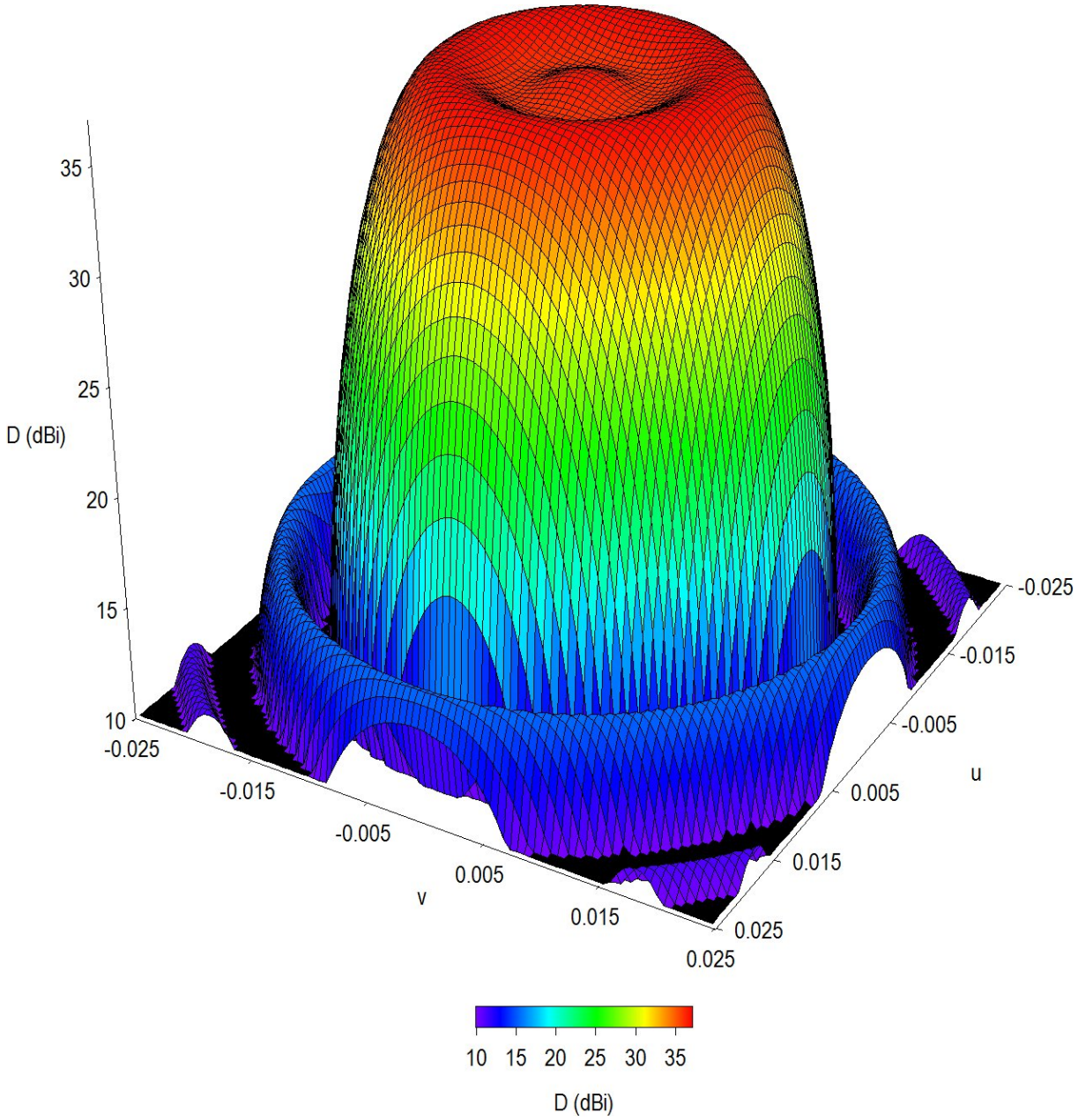

Figure 25: Circular beam pattern for the 607-element isophoric array of Table 16 (element diameter 2.2λ, element factor $\cos^{10}\theta$.)

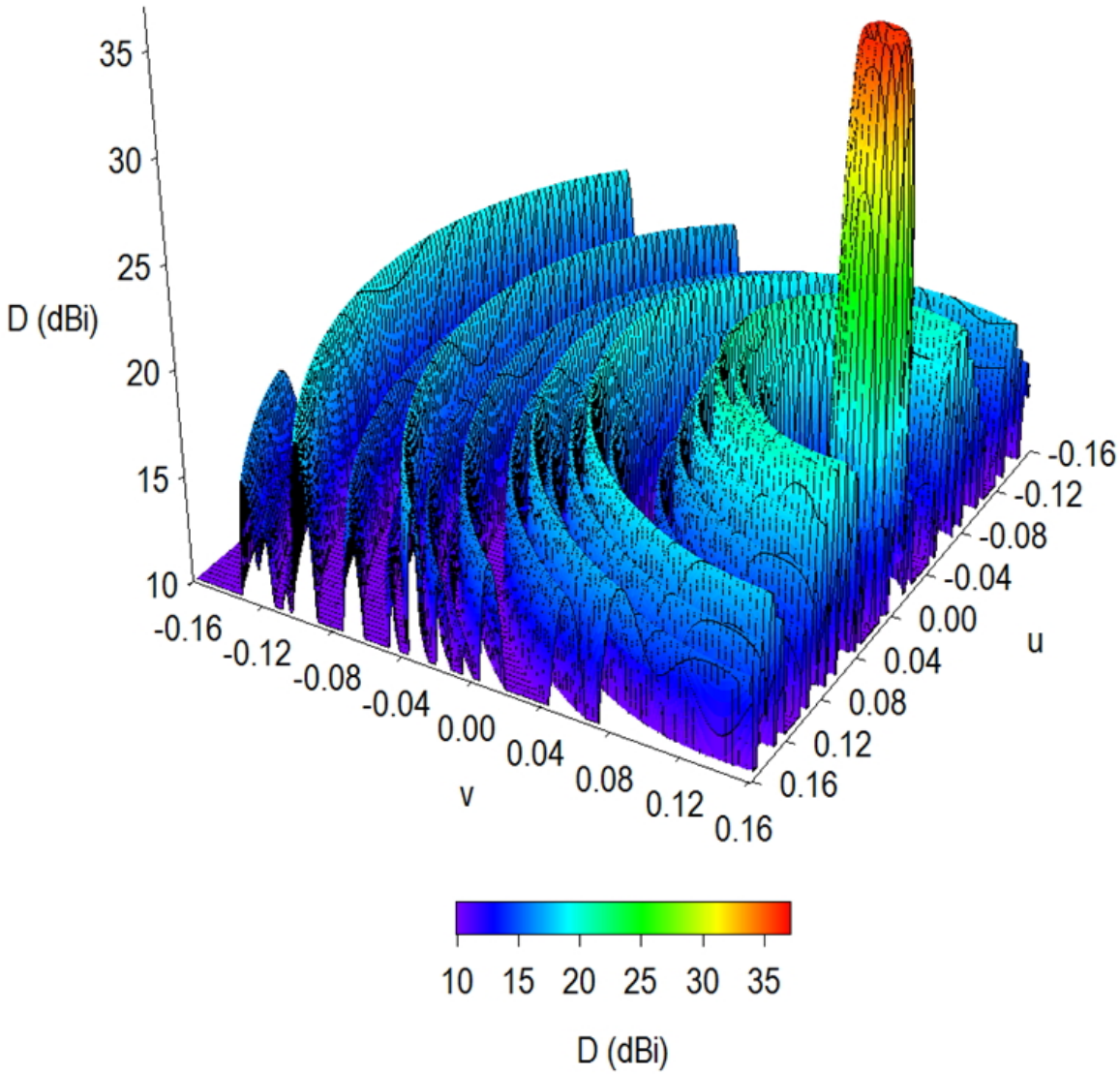

Figure 26: Circular beam pattern of Fig. 25 scanned to $\theta = 8°, \phi = 0°$ ($u = \sin\theta\cos\phi, \nu = \sin\theta\sin\phi$).)

- **Example 2**

  In the next example, we consider the synthesis of a flat-topped circular elliptical beam with a width of 1.46° along one axis and 0.73° along the other. This pattern can be achieved just by doubling the distance of the elements from the x axis of the antenna described in Table 16. The arrangement of the elements of the array is shown in Fig. 27. The resulting pattern has the specified dimensions with a directivity of at least of 36.0 dBi throughout the beam top and a ripple of 1.3 dB (Fig. 28). The side lobe level is -15.6 dB inside the Earth and it is increased to -10.1 dB outside the Earth. Regarding to the steering capabilities of this antenna, since the antenna has been stretched in the direction of the x-axis, i.e, the direction of the minor axis of the elliptical beam, it is excepted to have worse steering performance in this direction. In fact, when this pattern is scanned in the direction of the minor axis ($\theta = 8°, \phi = 0°$), the resulting side lobe level inside the Earth is notability increased to -8.0 dB due to the apparition of high grating lobes (see Fig. 29), whereas this level remains practically unaltered (-15.0 dB) when the pattern is scanned in the direction of the mayor axis ($\theta = 8°, \phi = 90°$), see Fig. 30.

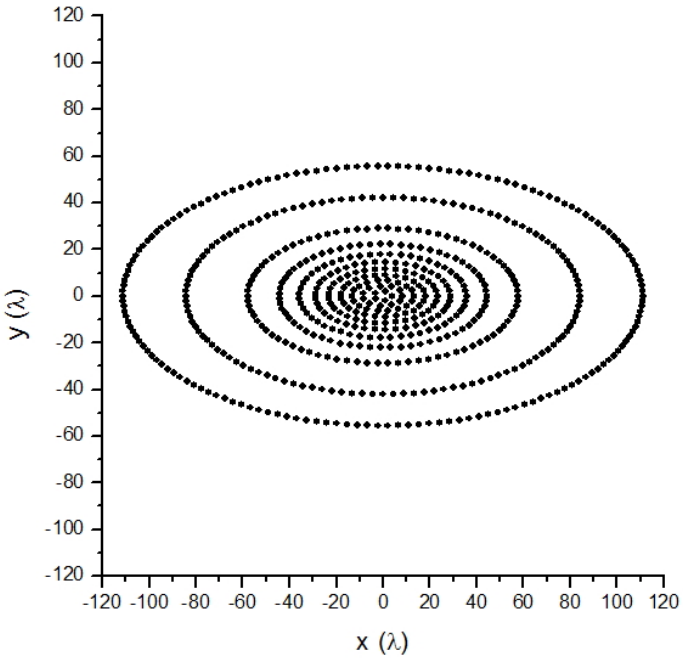

Figure 27: Arrangement of the elements for the resulting isophoric array to synthesize an elliptical beam (element diameter 2.2λ, element factor $\cos^{10}\theta$.)

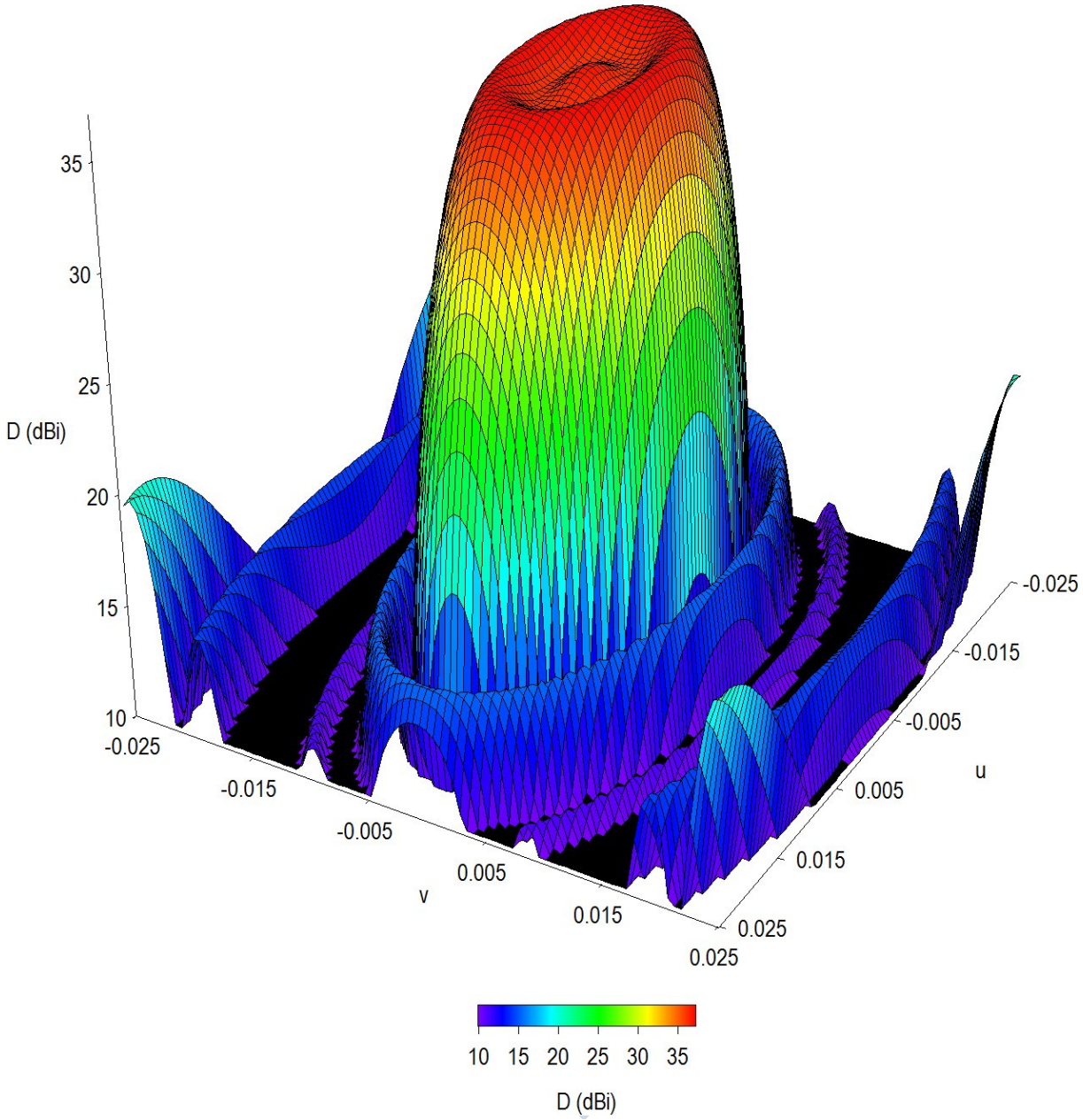

Figure 28: Elliptical beam pattern of the array array layout from the Fig. 27 ($u = \sin\theta\cos\phi, \nu = \sin\theta\sin\phi$).

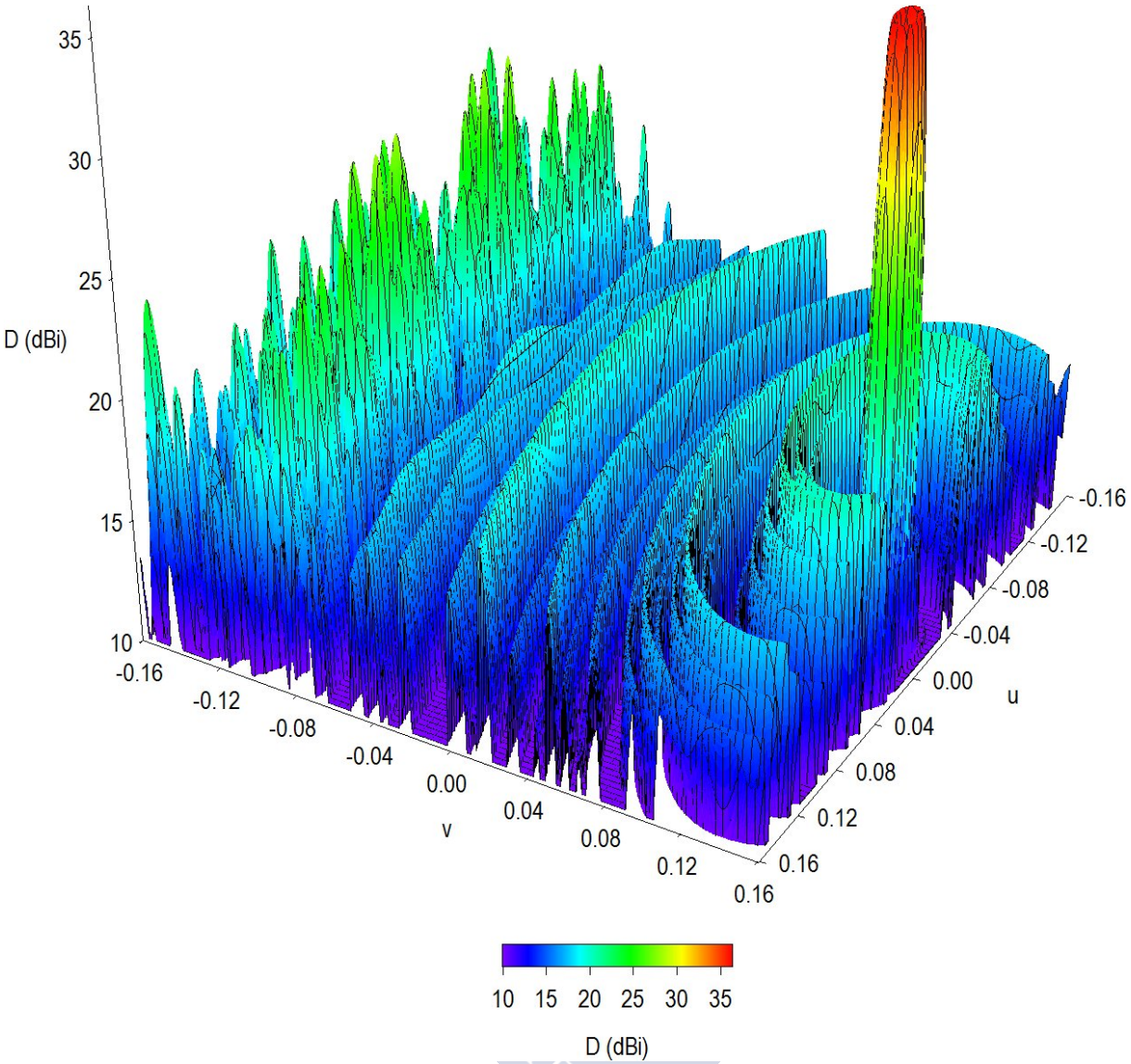

Figure 29: Elliptical beam pattern of Fig. 28 scanned to $\theta = 8°, \phi = 0°$ ($u = \sin\theta\cos\phi, \nu = \sin\theta\sin\phi$).)

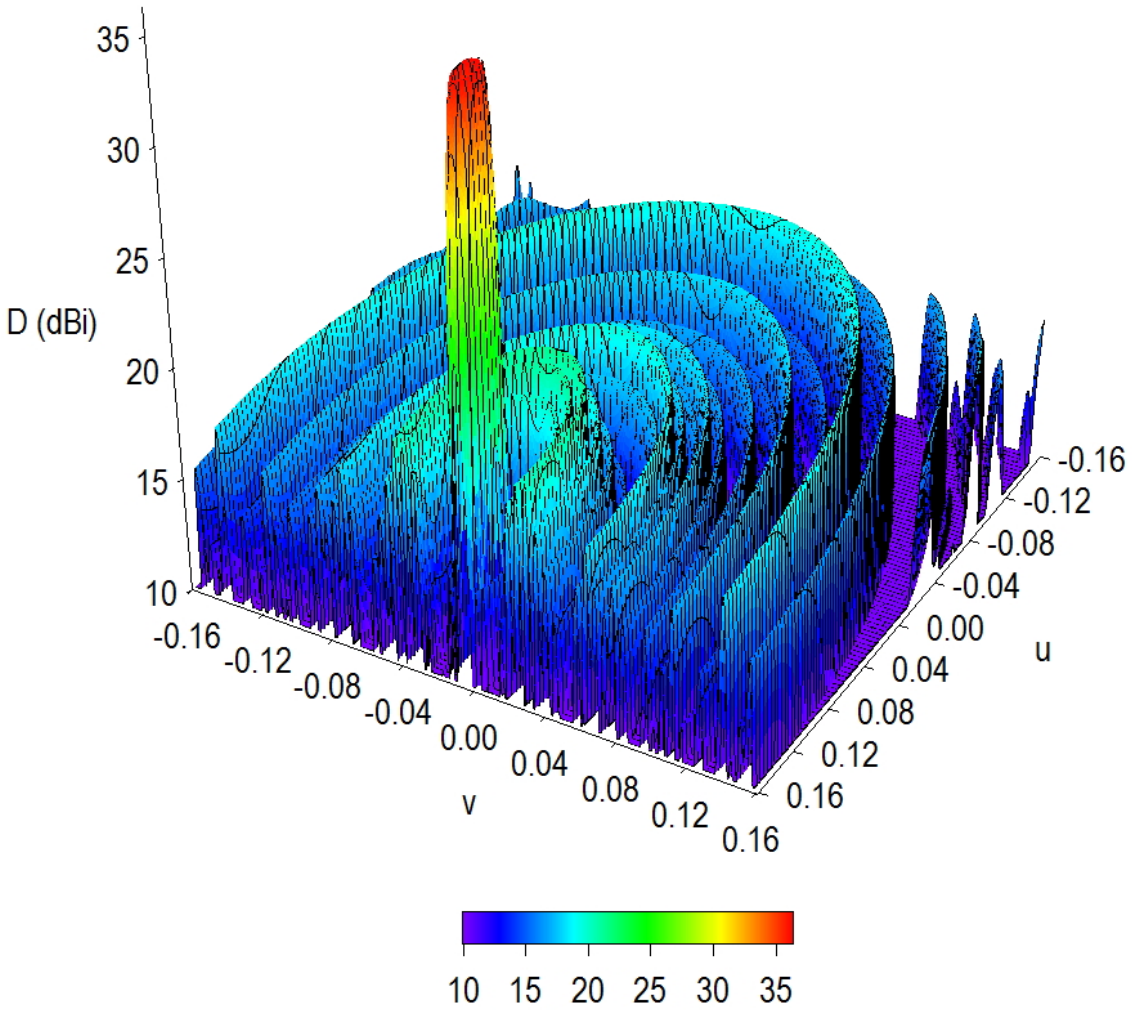

Figure 30: Elliptical beam pattern of Fig. 28 scanned to $\theta = 8°, \phi = 90°$ ($u = \sin\theta\cos\phi, \nu = \sin\theta\sin\phi$).)

- **Example 3**

  Finally, we consider the synthesis of a flat-topped square beam with a width of about 1° from side to side (the Iberian Peninsula fits very well into this contour). In this case, the antenna elements of Table 16 are radially stretched as in [26] and the array layout has a quatrefoil shape (Fig. 31). The resulting pattern has the specified dimensions with a directivity of at least of 35.0 dBi throughout the beam top and a ripple of 1.5 dB (Fig. 32). The side lobe level is -12.8 dB inside the Earth and -9.5 dB outside the Earth.

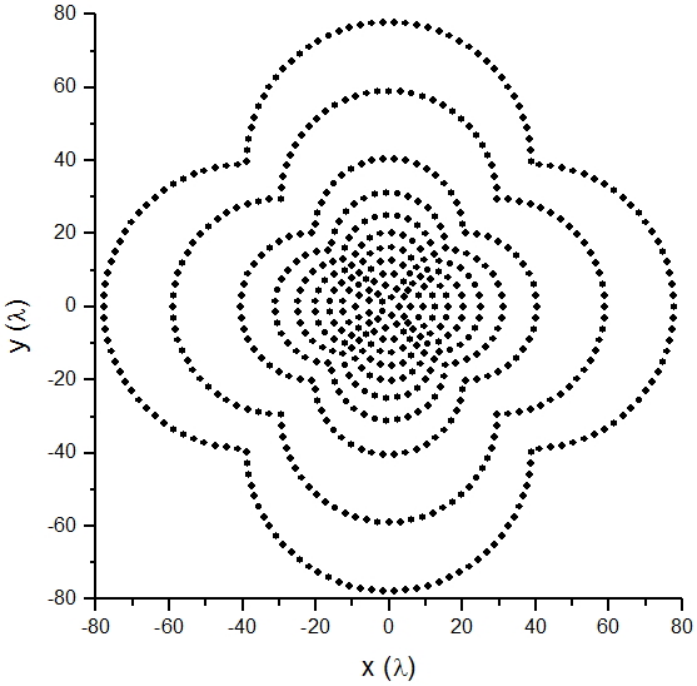

Figure 31: Arrangement of the elements for the resulting array to synthesize a square beam (element diameter 2.2λ, element factor $\cos^{10}\theta$.)

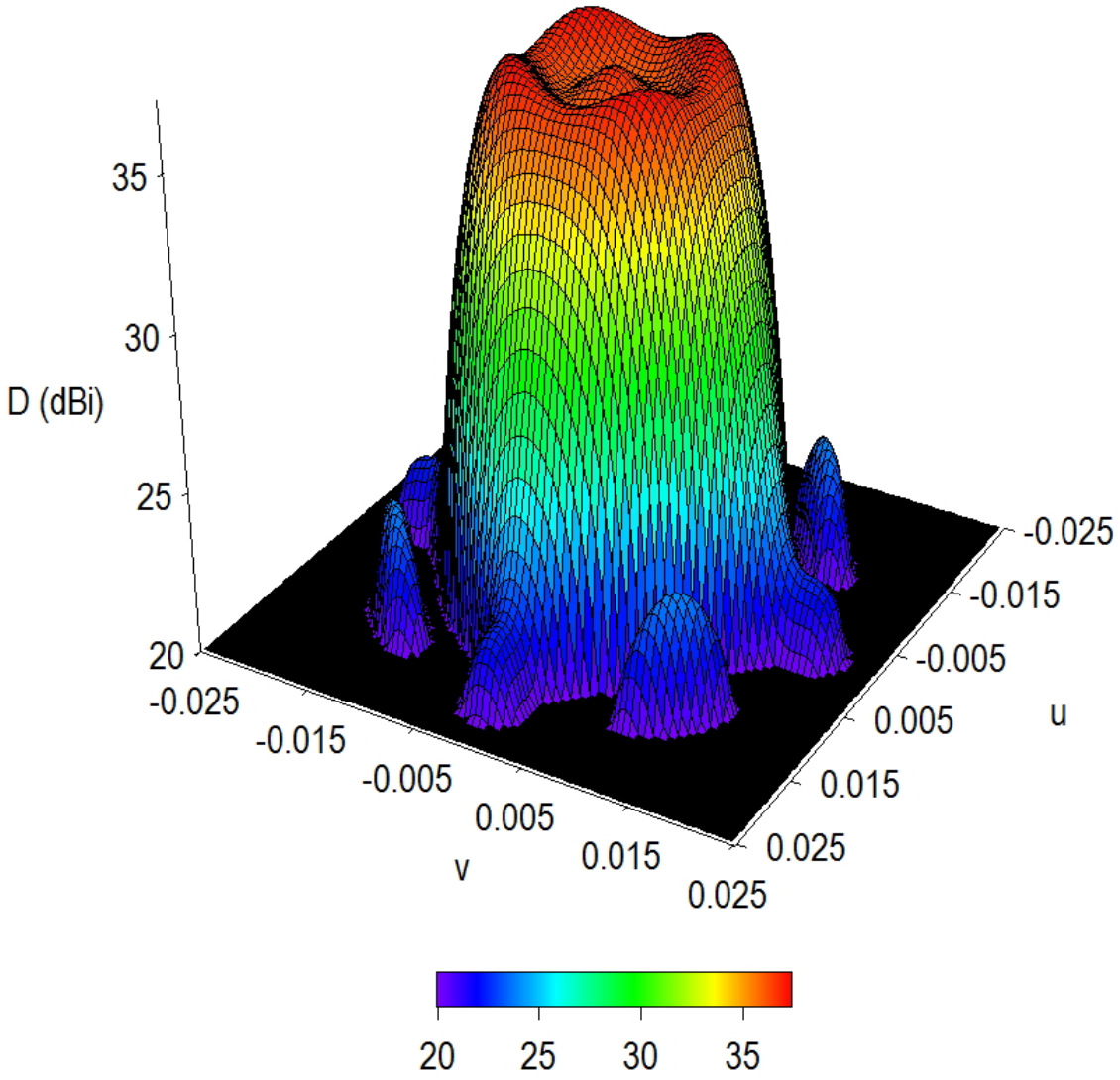

Figure 32: Square beam pattern of the array layout from Fig. 31 ($u = \sin\theta\cos\phi, \nu = \sin\theta\sin\phi$).

References

[1] A. A. Salas-Sánchez, J. Fondevila-Gómez, J. A. Rodríguez-González, and F. J. Ares-Pena, 'Parametric synthesis of well-scanning isophoric pencil beams,' *IEEE Trans. on Antennas Propag.*, vol. 65, no.3, pp. 1422-1427, Mar. 2017.

[2] Aarón Ángel Salas-Sánchez, Juan Antonio Rodríguez-González, and Francisco José Ares-Pena, 'Parametric Synthesis of Isophoric Phase-Shaped Flat-Topped Beams,' Under Review for publication in the Journal *IEEE Trans. on Antennas and Propag.*.

[3] M.I. Skolnik, "Nonuniform arrays," In R.E. Collin and F.J. Zucker (eds.), *Antenna Theory, Part I*, New York, McGraw-Hill, 1969.

[4] G. Toso, C. Mangenot, A. G. Roederer, "Sparse and thinned arrays for multiple beam satellite applications," in *Proc. 2nd Eur. Conf. Antennas Propagat. (EUCAP 2007)*, Edinburg, United Kingdom, Nov. 11-16, pp. 450, 2007.

[5] G. Toso, C. Mangenot, A. G. Roederer, "Sparse and thinned arrays for multiple beam satellite applications," in *Proc. 29th ESA Antenna Workshop on Multiple Beams and Reconfigurable Antennas*, Noordwijk, The Netherlands, Apr. 18-20, pp. 207-210, 2007.

[6] A.A. Salas-Sanchez, J.A. Rodriguez-Gonzalez, E. Moreno-Piquero and F.J. Ares-Pena, "Synthesis of Taylor-like patterns with uniformly excited multi-ring planar antennas," *IEEE Trans. Antennas Propag.*, vol. 62, No. 4, pp. 1589-1595, April 2014.

[7] W. Doyle, "On approximating linear array factors," RAND Corporation Memorandum RM-3530-PR, Feb. 1963.

[8] O.M. Bucci, D. Pinchera, "A generalized hybrid approach for the synthesis of uniform amplitude pencil beam ring-arrays", *IEEE Trans. on Antennas and Propag.*, Vol. 60, No. 1, pp.174-183, Jan. 2012.

[9] R.E. Willey, "Space tapering of linear and planar arrays," *IRE Trans. Antennas Propag.*, vol. 10, pp. 369-377, Jul. 1962.

[10] T.A. Milligan, "Space-tapered circular (ring) array," *IEEE Antennas Propag. Mag.*, Vol. 46, No. 3, pp. 70-73, Jun. 2004.

[11] M.C. Viganó, G. Toso, G. Caille, C. Mangenot, I.E. Lager, "Sunflower array antenna with adjustable density taper," *Int J Ant Prop*, 624035, Jan. 2009. doi: 10.1155/2009/624035.

[12] O.M. Bucci, S. Perna, "A deterministic two dimensional density taper approach for fast design of uniform amplitude pencil beam arrays," *IEEE Trans. Antennas Propag.*, Vol. 59, No. 8, pp. 2852-2861, Aug. 2011.

[13] O.M. Bucci, S. Perna, D. Pinchera, "Advances in the Deterministic Synthesis of Uniform Amplitude Pencil Beam Concentric Ring Arrays," *IEEE Trans. Antennas Propag.*, Vol. 60, No. 7, pp. 3504-3509, Jul 2012.

[14] T.A. Milligan, "Modern Antenna Design," 2nd edition, John Wiley and Sons, 2005, pp. 194-195.

[15] A. Trastoy-Ríos, M. Vicente-Lozano, F. Ares-Pena, "Shaped beams from circular apertures and arrays with uniform amplitude", *Electron. Lett.*, Vol. 36, No. 14, pp.1180-1182, July 2000.

[16] O.M. Bucci, T. Isernia, A.F. Morabito, S. Perna, D. Pinchera, "On the optimal synthesis of shaped beam sparse arrays having uniform amplitude excitations", *Proc. IEEE International Symposium on Phased Array Systems & Technology*, 2010, pp. 757-762.

[17] O.M. Bucci, T. Isernia, A.F. Morabito, "A Deterministic Approach to the Synthesis of Pencil Beams Through planar Thinned Arrays," *Progr. In Electromagn. Res.*, Vol. PIER 101, pp. 217-230, 2010.

[18] W.P.M.N. Keizer, "Synthesis of Thinned Planar Circular and Square Arrays Using Density Tapering," *IEEE Trans. Antennas Propag.*, Vol. 62, No. 4, pp. 1555-1563, Apr. 2014.

[19] X.K. Wang, Y.C. Jiao, Y.Y. Tan, "Synthesis of Large Thinned Planar Arrays Using a Modified Iterative Fourier Technique," *IEEE Trans. Antennas Propag.*, Vol. 62, No. 4, pp. 1564-1571, Apr. 2014

[20] O.M. Bucci, T. Isernia, S. Perna, D. Pinchera, "Isophoric Sparse Arrays Ensuring Global Coverage in Satellite Communications," *IEEE Trans. Antennas Propag.*, Vol. 62, No. 4, pp.1607-1618, Apr. 2014.

[21] Y. Rahmat-Samii, "Reflector antennas." Chapter 15 in: Y.T. Lo and S.W. Lee (eds.), Antenna Handbook: Theory, Applications, and Design, New York, Van Nostrand Reinhold, 1988.

[22] P.J.B. Clarricoats, S.M. Tun, C.G. Parini, "Effects of mutual coupling in conical horn arrays," *IEE Proc.*, Vol. 131, Part H, No. 3, pp. 165-171, June 1984.

[23] J. Fondevila-Gómez, I.C. Coleman, J.A. Rodríguez-González, F. Ares-Pena, "A cautionary note on optimization," *IEEE Antennas Propag. Mag.*, Vol. 55, No. 5, pp. 136-139, Oct. 2013.

[24] W.H. Press, W.T. Vetterling, S.A. Teukolsky, B.P. Flannery, Numerical Recipes in C, 2nd ed., Cambridge, U,K.: Cambridge University Press, 1992.

[25] R.S. Elliott, G.J. Stern, "Shaped patterns from a continuous planar aperture distribution," IEE Proc., Vol. 135, Pt. H, No. 6, pp. 366-370, Dec. 1988.

[26] F. Ares, R.S. Elliott, E. Moreno, "Design of Planar Arrays to Obtain Efficient Footprint Patterns With an Arbitrary Footprint Boundary", *IEEE Trans. Antennas Propag.*, Vol. 42, No. 11, pp.1509-1514, Nov. 1994.

4 Planar antenna prototyping

4.1 Summary

In this chapter an antenna design based on the use of an active dipole placed above a ground plane with an array of parasitic dipoles is presented. The presence of the parasitic dipoles increases the effective antenna size and significantly improves directivity over that of an isolated dipole in front of a ground plane. In addition, the use of just one active element makes for a very simple feed network that reduces the complexity of the antenna. As an application of this technique, a planar array of 48 parasitic dipoles above a ground plane, fed by a single active dipole at 5 GHz, was designed to afford a pencil beam pattern of moderate gain and bandwidth. Measurements agree well with theory. With a protective radome in place, directivity and gain were, respectively, 15.30 and 14.78 dB, the sidelobe level -6.15 dB, and the bandwidth 12.7% for $S_{11} < -10$ dB and 3.1% for gain loss < 3 dB [1].

4.2 Introduction

One way to reduce the complexity and cost of an array antenna is to eliminate the need for a complex feed network by feeding parasitic elements via a single active element [2], [3]. The elements that are not directly driven, called parasites, receive their excitations from the driven element through field coupling. Parasitic array elements introduce degrees of freedom that allow patterns to be synthesized without modification of the feed. A well-known example is the Yagi-Uda array, a linear array of parallel dipoles, only one of which is connected to the feed line. Though most commonly seen as an array of metal rods, the Yagi-Uda design can be implemented on a printed circuit board as either strips [4], [5] or slots [6], and can be used for the individual elements of a planar array [7]. A planar array of nanoscale Yagi-Uda elements has been designed for optical frequencies with a view to its connection to photonic circuits [8]. Arrays of parasitic elements can also be combined with multi-element active arrays; a design using parallel printed circuit boards is the subject of a patent application by Killen and Delgado [9]. In [10] we designed a 48-parasite pencil beam array with moderate gain and bandwidth using the method of moments as implemented in FEKO simulation software [11] and its particle swarm optimization module. Here we describe the design and construction of a similar array, more compact than that of [3], with optimized directivity and impedance matching a 50Ω feedline. Measurements of its characteristics with and without a protective radome agree well with theory.

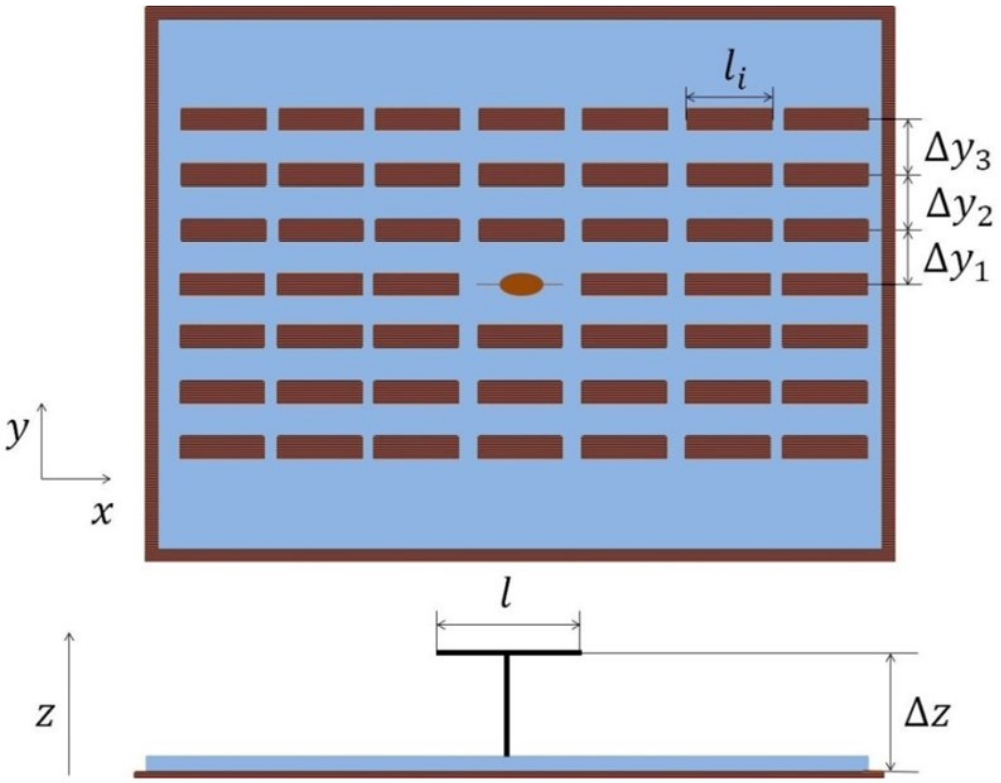

Figure 33: Top view (top) and side view (bottom) of the initial geometry used for optimization (not to scale), with the optimized parameters indicated.

4.3 Design and construction

The basic design comprised a 1.5 mm thick sheet of dielectric (DICLAD 880; $\epsilon_r = 2.17$, $tan(\delta) = 9 \times 10^{-4}$) bearing a ground plane on one side and, on the other side, a array of parallel parasitic strips with the central strip replaced by a pillar bearing an active feed dipole parallel to the parasites (Fig. 33). The centres of the parasites were separated in the direction parallel to their length (x). The design frequency was 5 GHz. Employing the same optimization and simulation methods as in [10], and imposing quadrantal symmetry, the lengths of the parasitic elements (l_1, l_2, ..., l_{15}), their width (δ_{pas}), the separation between parasite rows perpendicular to their length (Δy_1, Δy_2, Δy_3), the length of the feed dipole (l) and the height of the feed dipole above the ground plane (Δz) were jointly optimized for maximum broadside directivity and matching to a 50Ω feedline using the minimizing cost function

$$C = c_1 \left(\frac{1}{D_{max}} \right)^2 + c_2(Re[Z_{in} - Z_0])^2 + c_3(Im[Z_{in}])^2 \tag{43}$$

where D_{max} is the directivity at broadside, Z_{in} the input impedance of the antenna, Z_0 the characteristic impedance of the feed line (50Ω), and the control parameters that, in the light of preliminary results, were set to the values $c_1 = 1.5$, $c_2 = c_3 = 2.0$. The starting values of the optimized parameters were as follows: the dipoles (active and passive) were all $\lambda/2$ long, the feed dipole was $\lambda/4$ above the ground plane, and the parasites were 0.005λ wide with their centres separated by $\lambda/4$ in the y direction. To simplify the calculations, the ground plane was treated as infinite, and the active dipole as a cylinder of radius 0.005λ.

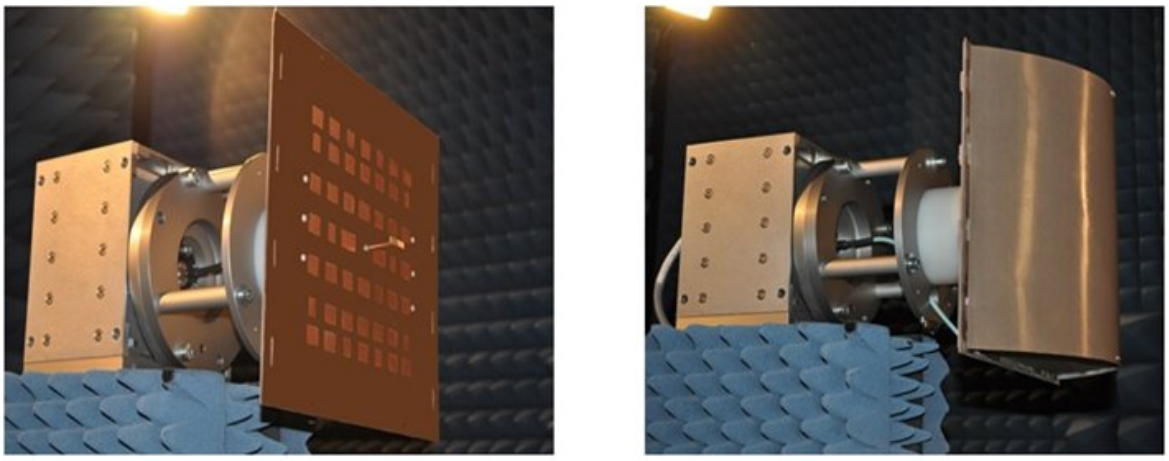

Figure 34: The antenna mounted on the measurement platform. Left: without the radome. Right: with the radome.

Table 17: Optimised Values for the Array of Parasitic Elements for the Designed Antenna

Parameter	**Optimum Value (λ)**	**Parameter**	**Optimum Value (λ)**
l_1	0.4550	l_{11}	0.1904
l_2	0.1997	l_{12}	0.3196
l_3	0.3223	l_{13}	0.2139
l_4	0.3670	l_{14}	0.3400
l_5	0.3009	l_{15}	0.3238
l_6	0.3231	δ_{pas}	0.2378
l_7	0.3117	Δy_1	0.5606
l_8	0.3261	Δy_2	0.5748
l_9	0.3233	Δy_3	0.3682
l_{10}	0.3175		

The optimized active dipole length was 0.46λ and its optimized height above the ground plane 0.69λ. The optimized parameters of the parasites are listed in Table 17. The overall size of the array, represented by the centres of its corner elements, was $3.30\times3.00\lambda^2$. Fig. 34 (left) shows the prototype constructed to these specifications. The lateral slots in the dielectric and ground plane are for holding the radome added subsequently as described below (Fig. 34 (right)).

4.4 Results without a radome

The performance of the antenna was evaluated in an $8.5 \times 4.5 \times 4.5\ m^3$ electromagnetic anechoic chamber lined with 8- and 18-inch pyramidal microwave absorbers affording a reflectivity better than –30 dB at frequencies above 1 GHz. S_{11} measurements exhibited a systematic shift with respect to the simulated curves, in principle due to the assumption of an infinite ground plane for the latter, although inaccuracies in construction, interactions between materials and welding defects may also have played a part. The minimum measured and simulated S_{11} values were –17.10 and –28.64 dB, respectively. A maximum peak gain of 14.98 dB (directivity 15.49 dB) was achieved at a working frequency of 4.93 GHz; Fig. 35 shows satisfactory agreement between the measured and simulated copolar power patterns at this frequency, and comparison with the crosspolar pattern.

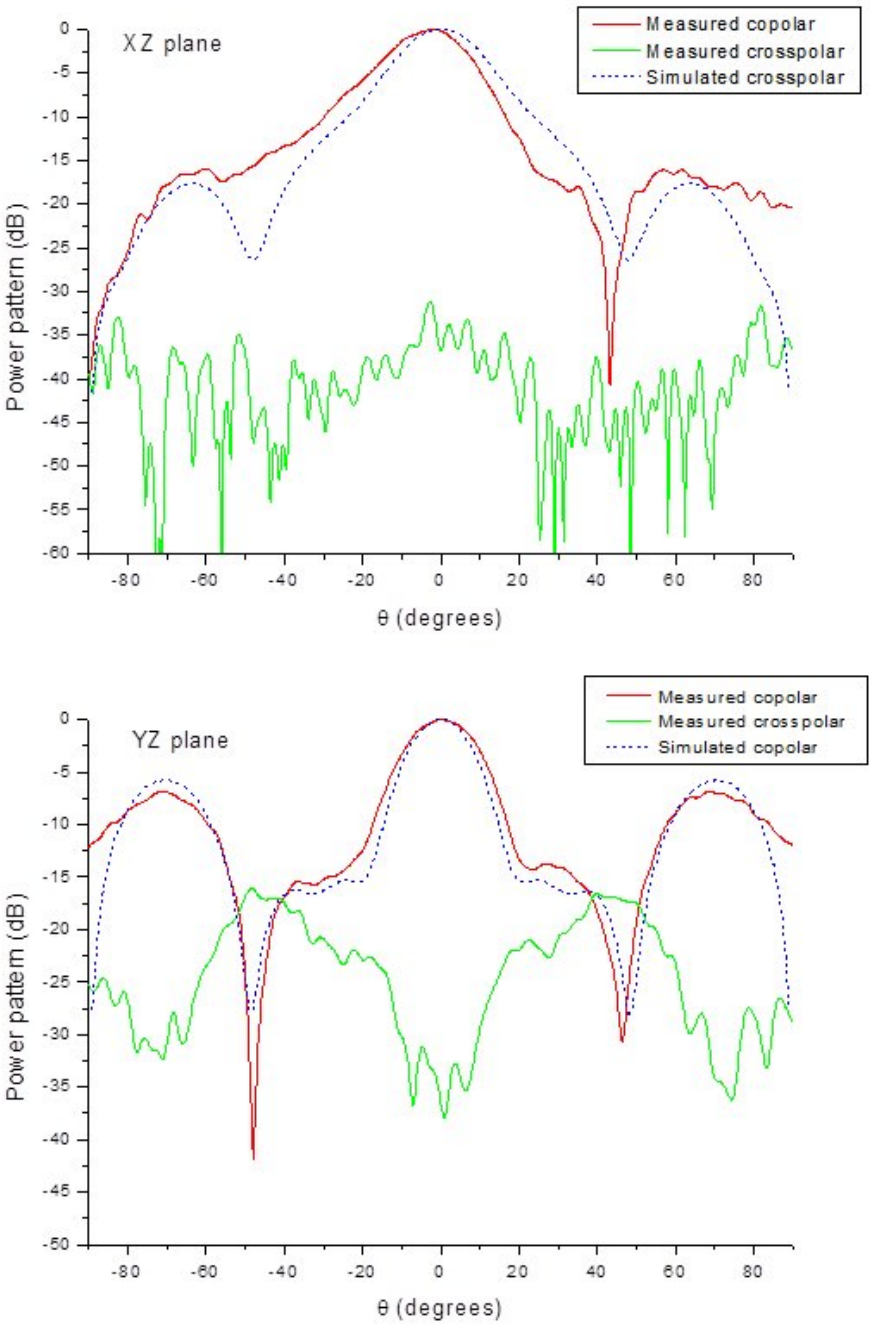

Figure 35: Measured copolar and crosspolar power patterns of the antenna without a radome, together with the simulated copolar component. Top: XZ-plane. Bottom: YZ-plane.

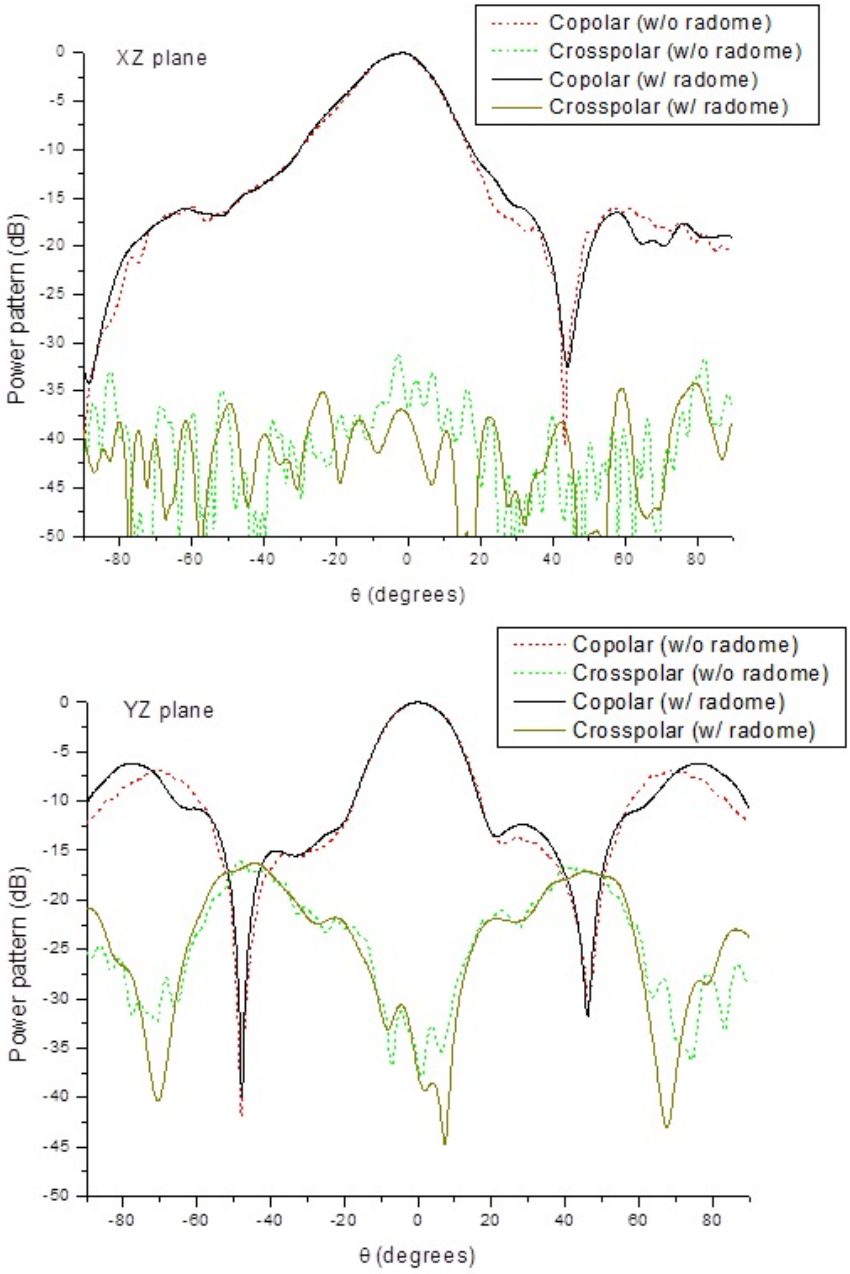

Figure 36: Measured copolar and crosspolar components of the power pattern of the antenna with and without the radome. Top: XZ-plane. Bottom: YZ-plane.

4.5 Results with a radome

The protective radome consisted of a sheet of DICLAD 880 bent to form a partial parabolic cylinder, the open ends of which were closed with parabolic segments of the sturdier dielectric FR4 ($\epsilon_r = 4.6$, $tan(\delta) = 0.014$) (Fig. 34). Both these dielectrics are low-loss. The presence of the radome hardly altered the copolar power pattern of the antenna at 4.93 GHz, and its influence on the crosspolar pattern was little greater (Fig. 36). Accordingly, there was hardly any alteration in either peak directivity (15.30 dB as against 15.49 dB without the radome) or peak gain (14.78 as against 14.98 dB), and S_{11} values (Fig. 37) differed by only about 1% from the values obtained without the radome. The bandwidth for $S_{11} < -10dB$ around the S_{11} minimum (–16.65 dB) was 12.69% referred to the minimum–S_{11} frequency of 4.65 GHz ($\approx$ 21 % if a small excursion above –10 dB around 4.4 GHz is ignored). However, the bandwidths for gain losses of less than 3 and less than 1 dB around the maximum-gain frequency of 4.93 GHz were only 3.1% and 1.6%, respectively.

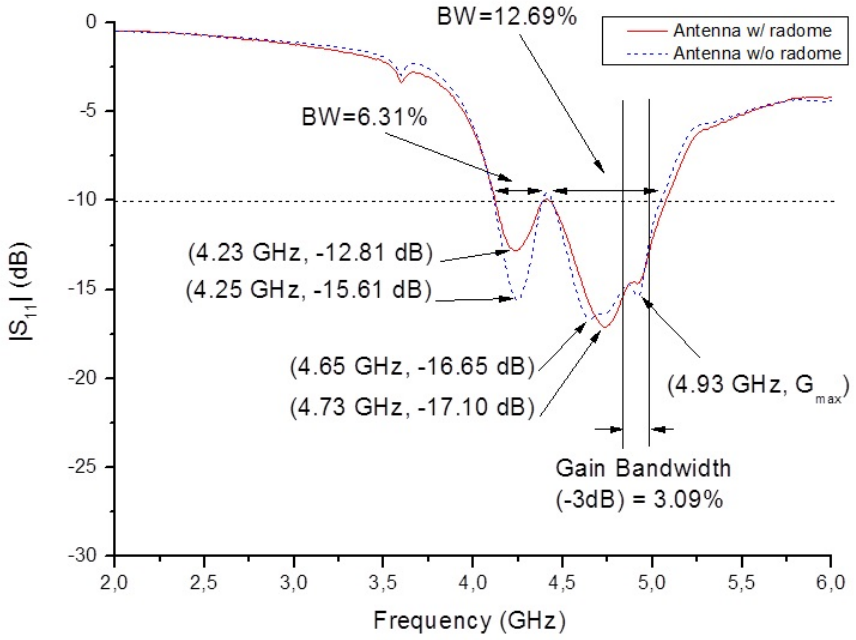

Figure 37: S_{11}-frequency curve for the antenna with the radome. Vertical lines show the frequency band with a peak gain loss less than 3 dB with respect to the maximum peak gain.

References

[1] Aaron A. Salas-Sanchez, Javier Fondevila-Gomez, Juan A. Rodríguez-González, and Francisco J. Ares-Pena, 'Measured characteristics of a planar array of parasitic elements fed by one active element,' *Microw. Opt. Technol. Lett.*, vol. 57, no. 12, pp. 2807-2809, Dec. 2015.

[2] M. Álvarez-Folgueiras, J.A. Rodríguez-González, and F.J. Ares-Pena, 'Pencil beam patterns obtained by planar arrays of parasitic dipoles fed by only one active element,' *Prog Electromagn. Res.*, PIER 103, pp. 419–431, 2010.

[3] M. Álvarez-Folgueiras, J.A. Rodríguez-González, and F.J. Ares-Pena, 'Experimental results on a planar array of parasitic dipoles fed by one active element, *Prog Electromagn. Res.*, PIER 113, pp. 369–377, 2011.

[4] E. Huang and T. Chiu, 'Printed Yagi antenna with multiple reflectors,' *Electron. Lett.*, vol. 40, pp. 1165–1166, 2010.

[5] R.A. Alhalabi and G.M. Rebeiz, 'High-gain Yagi-Uda antennas for millimeter-wave switched-beam systems,' *IEEE Trans. Antennas Propag.*, vol. 57, pp. 3672–3676, 2009.

[6] A.Y. Simba, M. Yamamoto, T. Nojima, and K. Itoh, 'Planar-type sectored antenna based on slot Yagi-Uda array,' *IEE Proc. Microwave Antennas Propag.*, vol. 152, pp. 347–353, 2005.

[7] S.P. Skobelev, 'Performance of Yagi-Uda elements in planar array antennas for limited-scan applications,' *Microwave Opt. Technol. Lett.*, vol. 34, pp. 141–145, 2002.

[8] D. Dregely, R. Taubert, J. Dorfmüller, R. Vogelgesang, K. Kern, and H. Giessen, '3D optical Yagi–Uda nanoantenna array', *Nat. Commun.*, vol. 2, 267, 2011.

[9] W.D. Killen and H.J. Delgado, 'Printed circuit board-configured dipole array having matched impedance-coupled microstrip feed and parasitic elements for reducing sidelobes,' U.S. Patent application 2001/0050654 A1, 2001.

[10] J.A. Rodríguez-González and F.J. Ares-Pena, 'Design of planar arrays composed by an active dipole above a ground plane with parasitic elements,' *Prog. Electromagn. Res.*, PIER 119, pp. 265–277, 2011.

[11] EM Software & Systems. FEKO. Suite 6.3. 2014. Available at: http://www.feko.info.

5 Feasibility studies of antenna solutions for monitoring ambiental parameters

Particulate atmospheric pollution alters the dielectric coefficient of the atmosphere. In principle, this could allow pollution to be measured via its effects on the performance of an antenna. In this chapter, a novel technique for measuring these effects, based on the use of an optimized air-filled waveguide-fed slot linear array, is shown. Also, in order to assure the precision of the method above mentioned, it is necessary to include a measurement system of the relative humidity level in which it is inmersed. Coating an antenna with a hydrophilic polyimide film has been reported to enhance the effects of atmospheric relative humidity on the characteristics of the antenna. In this work we designed Yagi-Uda antennas with polyimide-coated dipoles, and we performed a simulation study investigating the influence of atmospheric relative humidity on their resonant frequencies. We conclude that antennas of this type might constitute viable sensors for the measurement of atmospheric relative humidity, and hypothesize that in certain situations such sensors may have advantages over existing alternatives.

Results of this work were published in [1, 2].

5.1 Introduction

Today, 54% of the world's population lives in urban areas, a proportion that is expected to increase to 66% by 2050 [3]. Particulate matter (PM) (or aerosols) is one of the major pollutants that affect air quality in urban and even rural areas of the world. Atmospheric pollution is a serious public health problem. The respiratory systems of children and the aged are particularly affected; for the most vulnerable, atmospheric pollution can be fatal. Air pollutants can cause allergic symptoms, but when associated with allergen pollen grains, their allergenicity power is increased. Other environmental effects include reduction of the ozone layer (which in turn favours skin cancers), and damage to the fabric of buildings and monuments. The sources of atmospheric pollution include both natural (wind-blown dust, sea salt from the oceans, and volcanic eruptions) and anthropogenic sources (aerosols from biomass burning, combustion from automobiles and emission from power plants) also play an important role in climate processes. The main components of atmospheric pollution are (depending on source) carbon monoxide, carbon dioxide, chlorofluorocarbons (CFCs), heavy metals (mainly lead), ozone, mononitrogen oxides (NOx), sulphur dioxide, volatile organic compounds (VOCs) and other hazardous air pollutants (HAPs, generally associated with specific industrial activity), and airborne particulate matter (PM). Each of these components poses a health threat. Although emissions of airborne pollutants have in general decreased over the past twenty years, in many Member States of the European Union (EU) they continue to exceed the limits that have been established internationally for the protection of human health and the environment [4], and epidemiological studies carried out in various EU cities during the past decade have confirmed that environmental pollution continues to affect the health

of both children [5] and adults [6].

Increased awareness of the importance of environmental quality, in part in relation to climate change, has created a demand for accurate, flexible measurement of multiple environmental variables. This is exemplified by the inclusion of the development of novel *in situ* observation systems as a specific challenge for the Climate action, Environment, Resource efficiency and Raw materials section of the European Union's Horizon 2020 program.

5.2 Particulate matter level: Waveguide fed-slot linear array antenna

Airborne PM can include all types of solid or liquid matter suspended in the air as smoke, dust or vapour. The components of its constituent particles can include toxic metals, but its biological effects depend not only on its chemical composition but also on the size and aerodynamic properties of its particles. The hierarchical size categories currently adopted in most pertinent legislation on the basis of their presumed biological relevance are $PM10$ (roughly, particles with an aerodynamic diameter less than $10\mu m$), $PM2.5$ (sub-$2.5\mu m$ particles), and UFP (ultrafine particles with diameters less than $0.1\mu m$). It is also often convenient to distinguish three mutually exclusive size categories: UFP, fine particles ($PM2.5$ minus UFP), and coarse particles ($PM10$ minus $PM2.5$). The current reference methods for monitoring airborne PM are manual, non-continuous gravimetric techniques with very limited portability and temporal resolution.

For continuous monitoring of environmental airborne particles, three main methods are currently employed [7, 8]. In all three, ambient air is drawn through a filter at a controlled volumetric rate, and the mass of particles caught on the filter in successive short pre-set time intervals is measured and recorded. In two of these methods the filter is automatically renewed between measurements (in practice, a roll of filter material is advanced). In one, the mass of the film of particles that accumulates on the filter during each measuring interval is determined by measuring the optical density of the film. In the other the mass of the film is determined by measuring the degree to which it attenuates a beam of beta radiation. In the third method the filter on which particles accumulate is placed on the tip of a vibrating horn. As particles accumulate, their increasing mass changes the natural frequency of the horn, and it is the change in frequency over a short interval that is measured in order to determine the mass accumulated during this interval. It may be noted that all three methods require relatively frequent replacement of filters.

Other methods, which for various reasons may be considered as less satisfactory or of more limited scope, are based on light scattering or scintillation caused by particles, the induction of electric current in a probe by charged particles, or the piezo-electric balance.

The potential for monitoring PM air quality using satellite data from space-based sensors from regional to global scales has been demonstrated using aerosol optical thickness (AOT) data [9]. Although the satellite-based retrieval of air quality is promising, it poses several challenges. There are many factors that can affect the relationship between AOT and $PM2.5$. For example, the satellite-derived quantities provide columnar information for ambient conditions whereas the $PM2.5$ measurements are representative of near-surface dry mass concentrations. The satellite footprints represent large spatial areas and are subject to cloud contamination [10].

In the literature, there are some approaches that use antennas for measurement of gaseous pollution. Grusha [11] needed either essential complication of the equipment for the data treatment in three frequency sounding by Sodar (sonic detecting and ranging) or three frequency RASS (radio acoustic sounding system) application with radio channel antennas choice. Tonouchi [12] suggests using THz technology for gas sensing by means of a quantum cascade laser, QCL (for instance, a new detection technique for detecting hazardous-gases, such as carbon monoxide, is required at fire sites where infrared gas detection is sometimes blocked, for example by concrete walls).

In another approach [13] automotive particulate matter emissions are monitored using a $LiDAR$ (Light Detection And Ranging). In this case, the set-up system is huge, including all the light sources and detectors, mirrors and retro-reflectors. A trailer hosting the data acquisition and computer system is parked on the side of a single line road where the exhaust plume of vehicles passing by is intercepted by the light beams.

All the above methods have quite limited portability and/or temporal resolution. There is therefore a need to develop apparatus allowing rapid, flexible exploration of both indoor and outdoor environments - apparatus that can, for example, be easily elevated to any desired height above ground, or mounted on an airplane or unmanned aerial vehicle (UAV). This is a critical point due to the inhomogeneity of atmospheric pollution in urban environments (it is well known that pollution is transported from one location to another by wind in the atmosphere).

To fill this gap, in this work a feasibility study of a novel technique for the measurement and characterization of airborne particulate matter using a microwave antenna is developed. It will be verified whether, at particle concentrations in the range of environmental interest, particulate atmospheric pollution alters the input reflection of an optimized linear waveguide-fed slot array in order to afford a narrow bandwidth.

More concretely, a well-known relation (see below), providing the relative permittivity of a mixture (polluted air) in terms of the permittivity of its constituents (unpolluted and humid air and polluting particles), is used. As it can be seen in section 5.2.1: 'Pure air', the unpolluted and humid air will be modelled using different atmospheric parameters.

Then, in subsection 5.2.1: 'Pollutant inclusions: Effective medium theory' this above mentioned mixture will be modelled in terms of the volume fraction of these different inclusions and the pure air will act as the hosting material. Once a relation between the different pollution level and the relative permittivity of the environment is established, a waveguide antenna is proposed (section 5.2.2: 'First approach') in order to measure how its reflection coefficient varies. For improving this response (i.e. in order to reach a stronger variation of the parameters), an optimization process of the antenna design will be described in section 5.2.2: 'Model improvement: Optimization process'. Then, in section 5.2.3 some numerical results obtained in the simulation process are shown in addition to the permittivity values related with two realistic examples of different atmospheric scenarios. These permittivity values are related with two different works:

First, *R.P. Michel et al.* [14] outlines the study of Diesel soot particle properties in the frequency band $2.0 - 40.0\ GHz$. Using a transmission/reflection (placing a sample in a section at waveguide or coaxial line and then measuring the scattering parameters using a network analyzer) as well a cavity perturbation method, the complex dielectric constant was measured for multiple of samples (soot particles produced by a Diesel engine and deposited on paper filter).

Second, *Koven et al.* [15] presents a method of inferring the dust composition from "Aerosol Robotic Network ($AERONET$)" observations in the "dust belt" region of the Earth. One of their measurements is the mean volume concentration of Black Carbon in the air of the West and South Sahara desert (in summer season) that can be used to determine the dielectric. Finally, some conclusions and future development are shown.

5.2.1 Electromagnetic model of air

- **Pure air**

  In the absence of particulate pollution, the relative dielectric constant of the air is almost unit, but it actually is a function of the air pressure, temperature and humidity. An empirical result which is useful at microwave frequencies is given by [16]:

$$\epsilon_r = \left[1 + 10^{-6}\left(\frac{79P}{T} - \frac{11V}{T} + \frac{3.8 \times 10^5 V}{T^2}\right)\right]^2 \tag{44}$$

  where P is the barometric pressure in millibars, T is the temperature in Kelvin, and V is the water vapor pressure in millibars. For example, with a pressure of $1atm$, a relative humidity of 60% and room temperature ($20°C$), the relative permittivity of otherwise unpolluted air is approximately 1.00067.

  However, the relative dielectric constant of polluted air must be different from unity, depending on the type and concentration of the polluting particles (also, it is ex-

pected that the relative dielectric constant was significantly greater than unity in certain industrial emissions or in clouds of volcanic ash [17]).

- **Pollutant inclusions: Effective medium theory**

  It is possible to calculate the effective macroscopic permittivity for a given heterogeneous material sample as a function of its structure and the geometrical and material characteristics of its constituent components. There is a general family of mixing rules defined by [18]:

$$\frac{\epsilon_{eff} - \epsilon_e}{\epsilon_{eff} + 2\epsilon_e + v(\epsilon_{eff} - \epsilon_e)} = f\frac{\epsilon_i - \epsilon_e}{\epsilon_i + 2\epsilon_e + v(\epsilon_{eff} - \epsilon_e)} \tag{45}$$

  where ϵ_{eff} is the effective permittivity of a mixture where spherical inclusions with permittivity ϵ_i occupy a volume fraction f in the host material ϵ_e. In this formula, is a dimensionless parameter. For different choices of ν the previous mixing rules are recovered: $\nu = 0$ gives the Maxwell Garnett rule whereas $\nu = 2$ gives the Bruggeman formula. In order to find which formula is better, numerical simulations (using $FDTD$ – Finite Differences Time Domain – method) have been used to calculate the effective permittivity of two- and three-dimensional mixtures with the result that when clustering effects are allowed, the Bruggeman prediction is closer to the simulations, whereas if the inclusions are all separate spheres, the results are better in agreement with the Maxwell-Garnett model [19, 20].

5.2.2 Proposed antenna model

- **First approach**

  Elliott and Kurtz [21] used an equivalent-dipole approach to calculate slot's lengths ($2l_i$) and offsets (x_i) that achieve a desired slot voltage distribution while ensuring both real active admittances and feed matching (see Fig. 38). The resulting shunt admittance model is valid under the assumption that the offsets slots are not large in reduced height waveguides (in our case, we are using a full height waveguide and the maximum offsets are constrained to $3a/8$). The required self-admittances were calculated by using empirical expressions whereas the mutual impedances were obtained using standard formulae [22].

  Based on this work, *Rodríguez et al.* [23] used an integrated optimization procedure for determining slot's lengths and offsets of a waveguide slot array corresponding to an excitation distribution that generates the desired power pattern but includes no elements with excessively weak excitation.

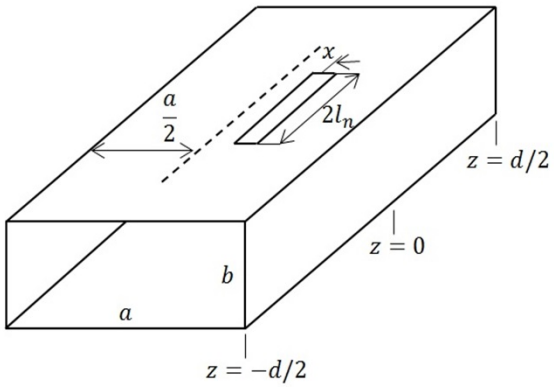

Figure 38: Waveguide slot module.

As first step to a hypothetical use of these devices in a measurement system of the polluted air, the optimized example in [23] was introduced in an effective medium with properties obtained by using the model described in section 5.2.1. The considered array is a linear array of N longitudinal slots cut with an interslot spacing of $\lambda_g/2$ in the broad wall, see Fig. 39. The equivalent circuit of the array consists of N admittances connected across a transmission line with spacing $\lambda_g/2$. Since all slots are spaced $\lambda_g/2$ apart, the equivalent input admittance of the array is simply the sum of all the individual slot admittances (standing-wave fed). The waveguide extreme is open (i.e., zero load admittance) and is located at a distance of $\lambda_g/2$ from the last slot.

The use of a dielectric medium changes the wavelength

$$(\lambda^{new} = \lambda_0/\sqrt{\epsilon_r}) \tag{46}$$

and therefore the wavelength in the guide (dominant TE_{10} mode) will also change:

$$(\lambda_g^{new} = \lambda^{new}/\sqrt{1-(\lambda^{new}/(2a))^2}) \tag{47}$$

These changes will alter all the electrical dimensions of the guide. As a consequence of this, the slot array is no longer standing-wave fed (i.e., the slots are not spaced $\lambda_g/2$). In this case, starting from the load, it is necessary to transform each admittance and sum it with the previous one in order to obtain the input admittance of the wavelength and therefore the input reflection coefficient.

- **Model improvement: Optimization process**

The theoretical description of the waveguide used in this work is strongly based on the referred in [23], but with some variations. For this reason, a previous mathematical description of the different parameters involved in the optimisation process is mandatory.

A rectangular air-filled waveguide operating in the TE_{10} mode (Fig. 39) is used. The array is fed by a standing wave and the slot voltages V_n^s are in phase. Given the values l_n and x_n the self-impedances $Z_{nn,eq}$ of an array of equivalent dipoles with the same lengths and relative positions can be obtained from either theoretical models [24] or by empirical expressions [22]; the corresponding mutual impedances $Z_{nm,eq}$ can be calculated using standard formulae [22].

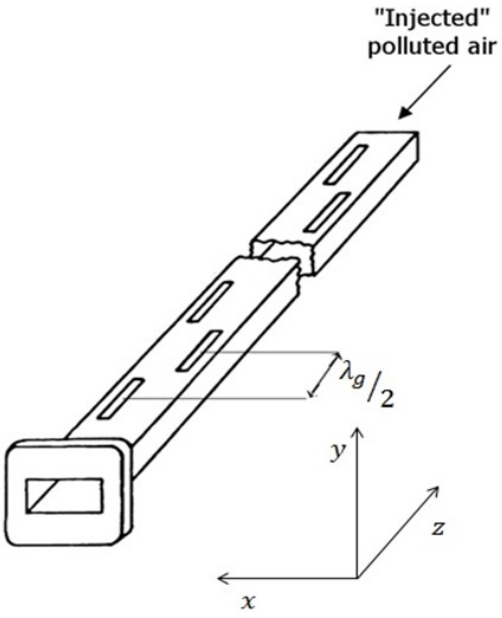

Figure 39: Waveguide-fed slot linear array.

The admittance of the slot Y_n^a is

$$\frac{Y_n^a}{G_0} = \frac{4ka}{\pi\beta b}\frac{\eta f_n^2}{Z_{n,eq}^a} \tag{48}$$

where

$$f_n = \frac{\sin(\pi x_n/a)}{\sin(kl_n)}[\cos(\beta l_n) - \cos(kl_n)] \tag{49}$$

(k, β) are the free-space and waveguide propagation constants, and (l/η,G_0) are the free-space and waveguide admittances, respectively. In (48), $Z^a_{n,eq}$ is the active impedance of the $n-$th equivalent loaded dipole

$$Z^a_{n,eq} = Z_{nn,eq} + Z^b_{n,eq} \tag{50}$$

where $Z^b_{n,eq}$ is the mutual coupling term, which depends on the mutual impedances and the slot voltages:

$$Z^b_{n,eq} = \sum_{\substack{m=1 \\ m\neq n}}^{N} \frac{V^s_m \sin kl_m}{V^s_n \sin kl_n} Z_{nm,eq} \tag{51}$$

The designed linear array consisted of N longitudinal shunt slots (Fig. 39) in the broad wall of an air-filled rectangular waveguide of dimensions a and b (Fig. 38). When it is immersed in vacuum ($\epsilon_r = 1$) the separation between the slots is $\lambda_g/2$ (standing-wave fed).

Now, we introduce the objective function in order to guarantee the impedance matching (when $\epsilon_r = 1.0$) and increase its sensibility to permittivity variations, i.e.,

$$C = c_1 \cdot \sum_{n=1}^{N} (X^a_{n,eq}/R^a_{n,eq})^2 + c_2 \cdot \sum_{n=1}^{N} |Y^a_n/G_0 - 1|^2 + c_3 \cdot 1/s_{min}. \tag{52}$$

In (52), $X^a_{n,eq}$ and $R^a_{n,eq}$ are, respectively, the imaginary and the real part of $Z^a_{n,eq}$; Y^a_n is the admittance of the slot calculated in (48) and s_{min} is the minimum slope of the interpolated function between neighbors in a point series created with different values of reflection coefficient in front of the permittivity of the dielectric introduced in the waveguide (a constraint in order to avoid negative values of this paramenter is used) in the range $\epsilon_r \in [1.00, \epsilon_{r,opt}]$ where $\epsilon_{r,opt}$ is related with the maximum pollutants concentration. Finally c_1, c_2 and c_3 are appropriate weights to the terms of the cost function. So, the objective function C is minimized by successively perturbing the l_n and x_n. In this process the Elliott-Kurtz method was performed because the electric field approximation, for the small values of the relative permittivity that will be considered in this optimization process, is in good agreement with the more realistic electric field distribution considered in the improved and generalized version of the Elliott-Kurtz method described by Elliott in 1983 [25]. Stern and Elliott showed than the standard model in which a longitudinal slot is represented by a shunt element on an equivalent transmission line is less justified at larger slots offsets and for smaller b dimensions [26]. Rengarajan [27] also showed these problems for a dielectric-filled waveguides. In addition the above

mentioned limitations, the shunt representation of the slot has been found to be poor also for higher permittivity values of the dielectric filling. Therefore, in this study, a full-height waveguide, offsets restrictions and small permittivity values of the dielectric filling were considered for correct modelling the longitudinal slot as a shunt element on an equivalent transmission line. Internal mutual coupling was not considered in this case, because the effects are ignorable for full-height guide [28].

5.2.3 Simulation results

In order to analyze the effect of the pollutants in terms of it can be considered a mean diameter of the particles of, approximately, $0.2\mu m$ [14, 29] a frequency of $9.4GHz$ ($\epsilon_i \approx 2.9$), air with a relative humidity of 60% as host material (see (44), $\epsilon_e \approx 1.00067$) and $f \approx 0.018$ [30, 31].

In [14], the resulting effective permittivity is $\epsilon_r = \epsilon_{eff} \approx 1.023$ (in this case, Bruggeman and Maxwell Garnett's (45) results match).

From [15], more concretely its value on Table 2, $f = 0.0068$ is obtained. And finally, by supposing again an air with a relative humidity of 60%, the resulting effective permittivity is $\epsilon_r = \epsilon_{eff} \approx 1.009$.

- **First approach**

  Attending to the typical values of the permittivity above calculated, an analysis of how some parameters of the antenna designed in [23] vary versus the effective dielectric constant in the range of $\epsilon_r \in [1, 1.05]$ was performed. The design frequency is $9.375GHz$. So, the considered array is a linear array of 16 longitudinal slots cut with an interslot spacing of $\lambda_g/2$ ($= 0.881in.$) in the broad wall of a standard X-band brass air-filled ($0.9 \times 0.4in.$) waveguide (WR90), see Fig. 39. The results are shown in Fig. 40 (reflection coefficient). The behavior of this array, when operated in an external dielectric medium, suffers appreciable alterations of the input reflection coefficient (and obviously of the standing-wave ratio) when the relative permittivity exceeded 1.01 (note that one of the values previously obtained was of 1.023). It is remarkable that the antenna used was not previously optimized for this purpose. The design of an *ad hoc* waveguide-fed linear array antenna will improve the sensitivity [32].

- **Optimized devices scenario**

  For a better performance of the device versus a tiny variation of the permittivity of the medium in what it is immersed, an optimization process is necessary following the procedure described in section 5.2.2: 'Model improvement: Optimization process'. Here, a collection of different minimum slopes of the reflection coefficient interpolated functions are shown (see Table 18). A total of 3 optimization processes (varying $\epsilon_{r,opt}$ from 1.01 to 1.05) were performed. The reason for that is to maximize

the minimum slope to different intervals. Also, the slope was calculated (for each $\epsilon_{r,opt}$ case) for different upper limits of the interval. So, an analysis of this variation shows that the optimum value appears when the optimized value and the upper limit of the interval ($\epsilon_{r,max}$) are matching. In Table 18 different obtained results are shown and they are compared with the offered by the designed antenna in [21] (of course, in this process the same number of slots ($N = 16$) was chosen). As an example, for the optimization to the minimum obtained slope is 20.88 - a value that rapidly decreases if we increase the upper limit of the interval (it fades to –6.73 if we use the interval from 1.00 to 1.05 for the calculation). So, if the values of the pollution result in an effective dielectric constant greater than 1.01, it is preferable to use an optimized antenna to a greater interval. This will offer a notably increasing of the sensibility of the device to the interval of interest on each case.

Moreover, a graphical representation of the results is shown in Fig. 40.

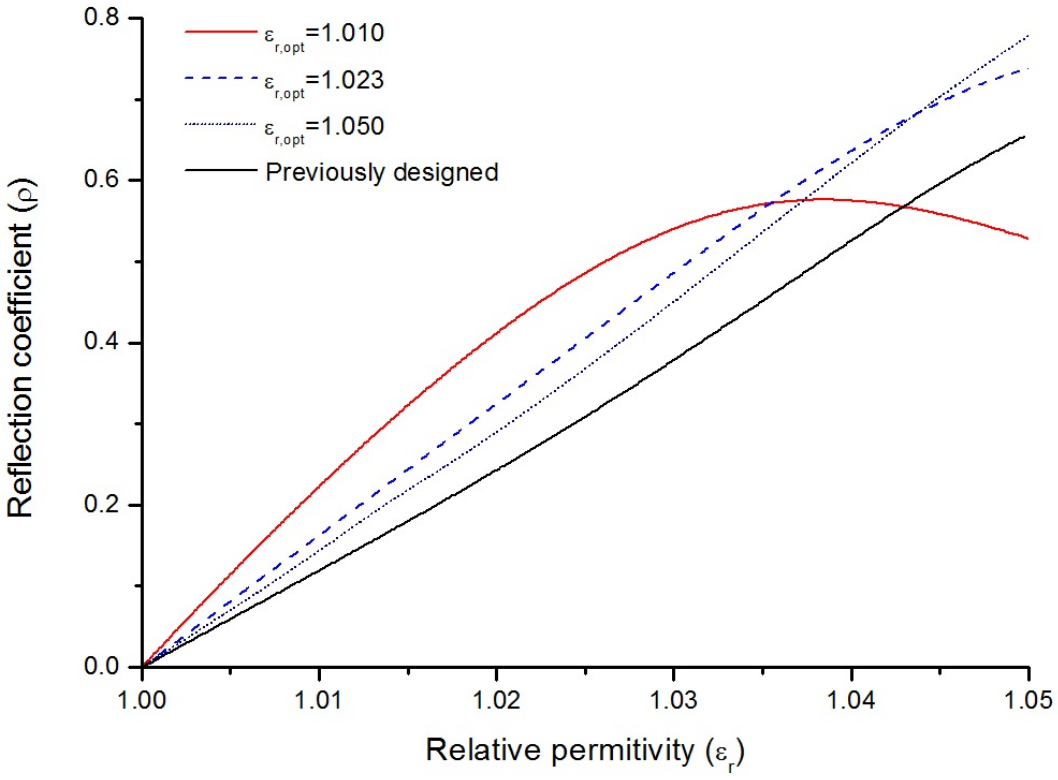

Figure 40: Dependence of reflection coefficient of different optimized antennas and of the antenna described in sect. 5.2.2: 'First approach' (designed in [23]) on the relative permittivity of the effective medium in which it was inmersed.

Table 18: Minimum slope of the reflection coefficient versus relative permittivity in the range $\epsilon_r \in [1.00, \epsilon_{r,max}]$

$\epsilon_{r,opt}$	$\epsilon_{r,max} = 1.01$	$\epsilon_{r,max} = 1.023$	$\epsilon_{r,max} = 1.05$
1.01	20.88	14.57	-6.73
1.023	16.23	16.05	6.33
1.050	13.85	13.74	13.74
Designed in [23]	10.81	10.81	10.74

- **Discussion about the attainable precision of the device**

  Now we can discuss about the attainable precision, in the measurement of the dielectric constant ϵ_r, of the air where the antenna is inmersed.

  Fig. 40 shows the reflection coefficient $\rho(\epsilon_r)$ vs. the above mentioned relative permittivity for different antennas of the section 5.2.2. These four graphics can be classified by the index n, from 1 to 4 from top ($n = 1$) to bottom ($n = 4$). By inspection of the plots we can determine that $\rho(\epsilon_r)$ essentially changes linearly with ϵ_r (with the exception of the case $n = 1$, where the linear dependence is limited to lower values of ϵ_r). Accordingly:

  $$\rho(\epsilon_r) = K_n(\epsilon_r - 1) = K_n \Delta\epsilon_r \tag{53}$$

  where the linear dependence of the reflection coefficient vs. the increments of the relative permittivity with respect to vacuum space ($\epsilon_r = 1$) has been highlighted. The constant K_n can be easily evaluated: it equals 20; 16.25; 12.5; 11.25, for n going from 1 to 4, respectively.

  Let us analyze the effect of the measurement error of the reflection coefficient, $\delta\rho$, on the corresponding error on the relative permittivity increments, $\delta[\Delta\epsilon_r]$, i.e., the quantity of our interest.

  So, from eq. (53):

  $$\delta[\Delta\epsilon_r] = \frac{\delta\rho}{K_n} = \frac{\delta\rho/\rho}{K_n}\rho. \tag{54}$$

  Substituting the value of ρ, from eq. (53) into eq. (54), we get:

  $$\delta[\Delta\epsilon_r] = \frac{\delta\rho/\rho}{K_n} K_n \Delta\epsilon_r = (\delta\rho/\rho)\Delta\epsilon_r, \tag{55}$$

  thus implying that the relative errors on the increments of the relative permittivity, $\delta[\epsilon_r]/\Delta\epsilon_r$, and on the reflection coefficient, $\delta\rho/\rho$, coincide. This result should have

been anticipated, due to the linear relation, eq. (53), between the two parameters. Assuming a reasonable 10% error in the reflection coefficient measurement, i.e., $(\delta\rho/\rho) = 0.1$, we get the same 10% error on the relative permittivity increments: these increments are in 10^{-2} range, while the error does not exceed the 10^{-3} limit: these expectations are reasonable, and furnish a full support to the presented feasibility study for the measurement of the particulate matter pollution in the atmosphere.

5.3 Relative humidity level: Polyimide coated Yagi-Uda antenna

In the previous section we described a feasibility study of a novel system for measurement of airborne particulate matter, (PM) an atmospheric pollutant of major concern. This system will measure PM through the influence of the latter on the relative dielectric constant of air and thereby on the reflection coefficient of a microwave slot array antenna that is introduced into the polluted air mass and acts as sensor. It is envisaged that, since the performance of this sensor is not affected by movement, and the whole system can in principle be made compact and portable, it will be an attractive alternative to current PM measurement systems in certain situations. Portable versions would allow rapid assessment of transient pollution episodes at ground level, while versions borne by manned or unmanned aircraft would be able to monitor larger-scale atmospheric episodes. Systems mounted on drones might be of special utility for following the evolution of PM clouds.

The PM measurement system described above requires knowledge of the relative humidity of the air mass being probed. While there are numerous existing methods of humidity measurement, from the classical psychrometer to miniaturized devices based on gravimetry or the alteration of thermal conductivity, optical parameters, or electrical resistivity or capacitance, we decided to investigate whether, in the present context there might be advantages in using an instrument based on a similar principle to the proposed PM sensor, namely humidity-induced alteration of the properties of an antenna. For example, one possibility would be to use the same antenna to transmit data to ground from an airborne vehicle.

The class of antennas chosen for investigation was the Yagi-Uda [22], a linear array of parallel dipoles, only one of which is fed directly by a power source; the others are parasites excited through near-field coupling to the driven dipole (Fig. 41). Yagi-Uda antennas are robust, inexpensive and moderately directional, are relatively easily matched to a feed network, and for the working frequencies envisaged are of a convenient size. The antenna characteristic via which it is intended to measure relative humidity is the resonant frequency, and to increase the sensitivity of this characteristic to humidity we propose to coat the dipoles with a hydrophilic polyimide with an humidity-sensitive dielectric constant. In this we follow *Chang et al.* [33], who developed this dielectric

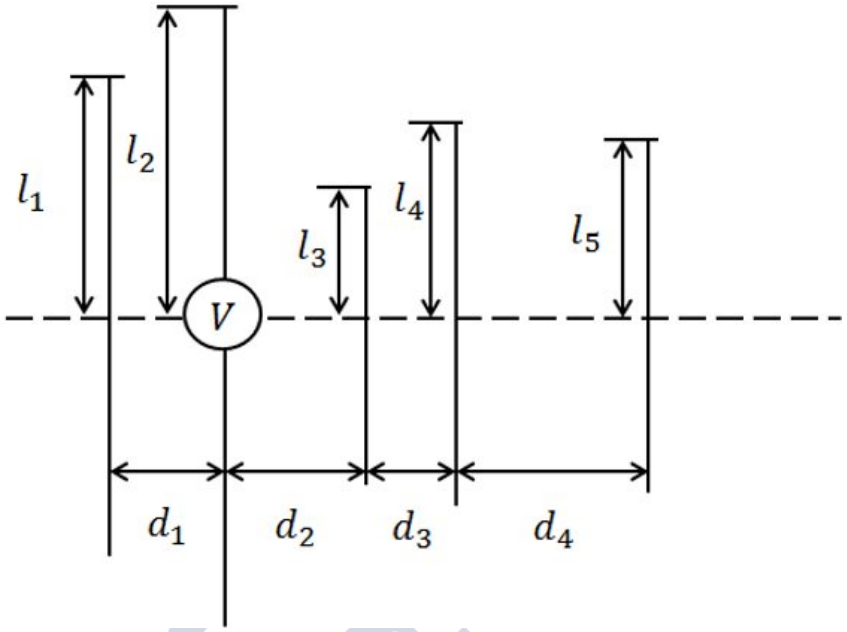

Figure 41: Schematic Yagi-Uda antenna. Dipole i is of length $2l_i$ and is located a distance d_{i-1} from dipole $i-1$. Dipole 2 is the active element.

for use in an radio-frequency identification (RFID) tag designed to report on relative humidity.

In what follows we describe the design of three Yagi-Uda antennas with resonant frequencies near $5GHz$, and we report the results of simulations in which their resonant frequencies were calculated in a series of atmospheres of different relative humidities. In all cases we assumed for simplicity that the polyimide layer and its dielectric constant had the thickness and the humidity response reported by *Chang et al.* [33].

5.3.1 Theoretical basis

The input impedance of a Yagi-Uda antenna with N dipoles, the second of which is the active element, is given by [22]:

$$Z_{in} = Z_{22} + \left(\frac{I_1}{I_2}\right) Z_{21} + \frac{I_3}{I_2} Z_{23} + \ldots + \frac{I_N}{I_2} Z_{2N} \tag{56}$$

where Z_{22} is the self-impedance of the active dipole, Z_{2j} is the mutual impedance between the active dipole and dipole j ($j \neq 2$), I_2 is the current in the active element, and I_j is the current induced in dipole j ($j \neq 2$) due to electromagnetic coupling with the other dipoles. For thin, cylindrical, uncoated metallic dipoles, the self-impedance can be determined using the corrected second-order version of the King-Middleton solution [34], and the effect of a dielectric coating can be taken into account using the equivalent radius defined

by *Popovic et al.* [35]. The mutual impedances of an array of dielectric-coated dipoles can be calculated by the method of moments (MoM); in this study, MoM calculations were performed using the electromagnetic simulation package FEKO [36].

5.3.2 Method

We designed Yagi-Uda antennas with cylindrical dipoles $0.6mm$ in diameter and input impedances that would match a 50Ω feed line under the driest conditions considered by *Chang et al.* [33] (atmospheric temperature $30°C$, atmospheric relative humidity 20%), and assuming that the thickness and relative permittivity of the polyimide coating on the dipoles were respectively $1.96\mu m$ and 2.5, the values reported by *Chang et al.* [33]. The design process employed a modified version of the method described by *Jones et al.* [37]: whereas these authors used a genetic algorithm to maximize gain, we used particle swarm optimization (PSO) as implemented in FEKO to optimize the impedance match between the antenna and a 50Ω feed line. The cost function C employed in the optimization process was

$$C = c_1 \cdot |Re(Z_{in}) - Z_0| + c_2 \cdot |Im(Z_{in})| \tag{57}$$

where Z_0 is the impedance of the feed line (50Ω) and c_1 and c_2 are weights controlling the relative importance of deviations in resistance and reactance. The overall procedure is summarised in Fig. 42. With the antenna designs in hand, we then used the FEKO software to simulate their behavior in atmospheres with a temperature of $30°C$ and relative humidities ranging from 20% to 90%, again relying on the data reported by *Chang et al.* [33] for the dependence of polyimide relative permittivity on the relative humidity.

5.3.3 Examples

- **Example 1**

  The passive dipoles of a Yagi-Uda antenna are divided into two classes: on one side of the active element are the reflectors, which are at least as long as the active element itself; on the other side are the directors, which are shorter than the active element. We first designed a Yagi-Uda with one reflector and three directors, the lengths and spacing of which are listed in Table 19. In simulations of its behavior at $30°C$ in atmospheres with relative humidities of $20-90\%$, its resonant frequency ranged from 5000.67 to 4972.58 MHz (Fig. 43).

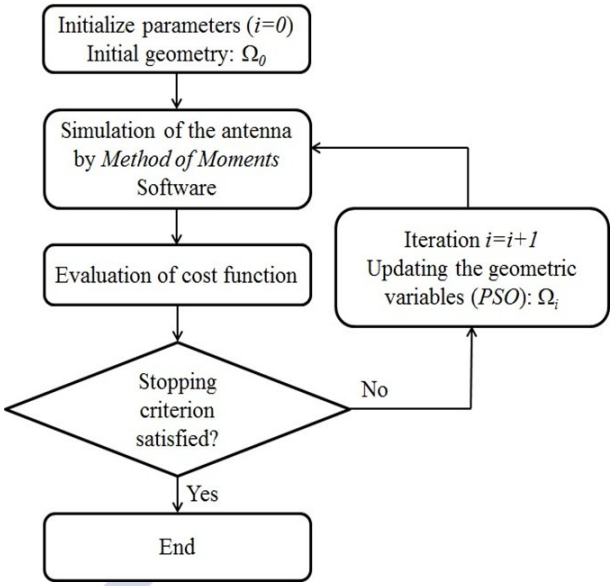

Figure 42: $\Omega_i \equiv$ Parameters of the *i-th* iteration (dipole lengths and between-dipole distances).

Table 19: Lengths and spacings of the example 1

# Element	Length	Spacings[a]
1	0.755λ	-
2[b]	0.435λ	0.351λ
3	0.403λ	0.324λ
4	0.476λ	0.276λ
5	0.930λ	0.835λ
Z_{in}	$49.95 - j0.18$	

[a] d_{i-1} in Fig. 41. [b]Active element.

- **Example 2**

  Table 20 lists the lengths and spacing of the dipoles of an antenna with two reflectors and two directors. As designed, its resonant frequency is 5002.01 MHz; as the relative humidity of its environment increased from 20% to 90% in simulations, its resonant frequency fell to 4971.24 MHz (Fig. 43).

Table 20: Lengths and spacings of the example 2

# Element	Length	Spacings[a]
1	0.629λ	-
2	0.437λ	0.247λ
3[b]	0.436λ	0.321λ
4	0.290λ	0.263λ
5	0.417λ	0.532λ
Z_{in}	$50.38 - j0.01$	

[a] d_{i-1} in Fig. 41. [b]Active element.

- **Example 3**

Like example 2, our final example had two reflectors and two directors, but was also endowed with an infinite ground plane parallel to and $\lambda/4$ from the plane of the dipole array. In the PM measurement system described in the Introduction, the primary function of this ground plane would be to prevent interference between the PM- and humidity-measuring antennas. In the event, we found that it also increased the response of the latter to changes in atmospheric relative humidity (Fig. 43). The geometry of the dipole array is summarized in Table 21.

Table 21: Lengths and spacings of the example 3

# Element	Length	Spacings[a]
1	0.942λ	-
2	0.777λ	0.523λ
3[b]	0.430λ	0.165λ
4	0.317λ	0.240λ
5	0.694λ	0.618λ
Z_{in}	$49.37 - j0.15$	

[a] d_{i-1} in Fig. 41. [b]Active element.

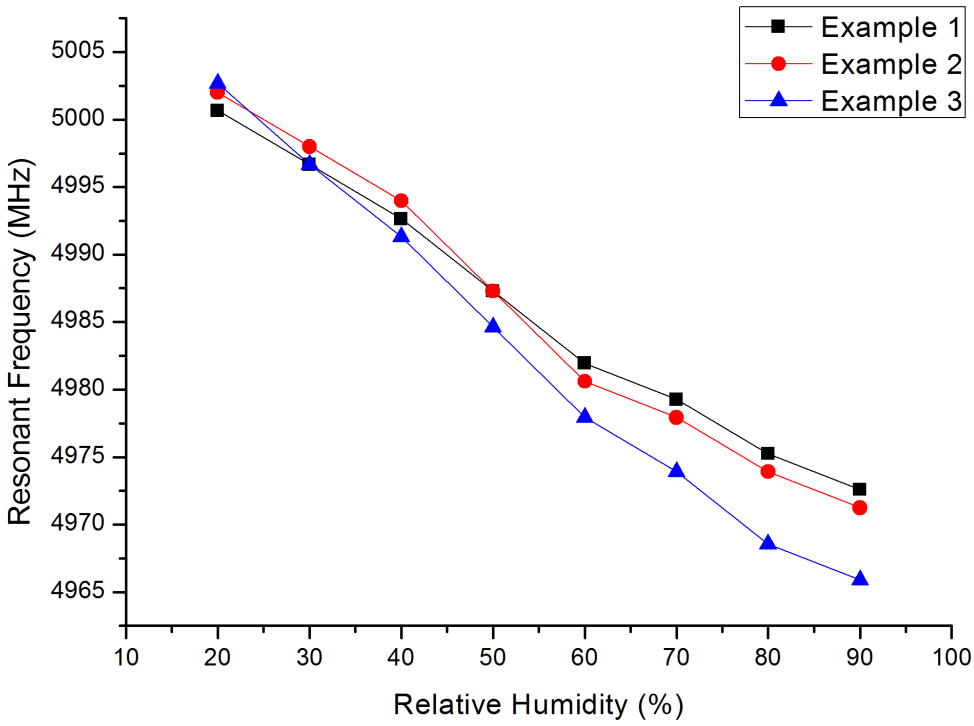

Figure 43: Resonant frequency of different polyimide-coated Yagi-Uda antennas vs. atmospheric relative humidity (simulation results).

References

[1] A.A. Salas Sánchez, M.E. López Martín, J.A. Rodríguez González, F.J. Ares Pena, "Technique for Determination of Particulate Matter Pollution in the Atmosphere Using Waveguide Slot Linear Array Antennas: A Feasibility Study," *IEEE Geosci. Remote Sens. Lett.*, vol. 13, no. 10, Oct. 2016.

[2] Aarón Ángel Salas-Sánchez, María Elena López-Martín, Juan Antonio Rodríguez-González, and Francisco José Ares-Pena, "Design of Polyimide Coated Yagi-Uda Antennas for Monitoring the Relative Humidity Level," *IEEE Geosci. Remote Sens. Lett.*, vol. 14, No. 6, pp. 961-963, Jun 2017.

[3] World urbanization Prospects, 2014.

[4] O. Hänninen, and A. Knol (eds.), *European perspectives on environmental burden of disease. Estimates for nine stressors in six European countries.* Helsinki, Finland: Nat. Inst. Health Welfare, 2011.

[5] M. Vrijheid *et al.*, "European birth cohorts for environmental health research," *Environ, Health Perspect.*, vol. 120, Nº 1, pp. 29-37, 2012.

[6] K. E. Nachman and J. D. Parker, "Exposures to fine particulate air pollution and respiratory outcomes in adults using two national data sets: a cross-sectional study," *Environ. Health*, pp. 11-25, 2012.

[7] Current knowledge of particulate matter (PM) continuous emission monitoring. Office of Air Quality, United States Environmental Protection Agency, Ref. EPA-454/R-00-039, Sep. 2000.

[8] Integrated Science Assessment for Particulate Matter (full report). United States Environmental Protection Agency, Federal Register Notice, Dec. 2009.

[9] A. V. Donkelaar, R. V. Martin, M. Brauer, R. Kahn, R. Levy, C. Verduzco, P. J. Villeneuve, 'Global Estimates of Ambient Fine Particulate Matter Concentrations from Satellite-Based Aerosol Optical Depth: Development and Application', *Environ, Health Perspect.*, vol. 118, pp. 847-855, 2010.

[10] Q. Zhang, D. R.Worsnop, M. R. Canagaratna and J. L. Jimenez, 'Hydrocarbon-like and oxygenated organic aerosols in Pittsburgh: insights into sources and processes of organic aerosols', *Atmos. Chem. Phys.*, vol. 5, pp. 3289–3311, 2005.

[11] G. V. Grusha, 'Antennas for the Remote Measurement Systems of the Gaseous Pollution Concentration', *International Conference on Antenna Theory and Techniques*, pp. 574-576, 2003.

[12] M. Tonouchi, 'Cutting-edge terahertz technology', *Nature Photonics*, vol. 1, pp. 97 – 105, 2007.

[13] C. Mazzoleni, H. D. Kuhns and H. Moosmüller, 'Monitoring Automotive Particulate Matter Emissions with LiDAR: A Review', *Remote Sens.*, vol. 2, pp. 1077-1119, 2010.

[14] R. P. Michel, R Baican, E. Schubert, 'Soot particle properties in the microwave range', 23rd European Microwave Conference, pp. 959-960, Madrid 1993.

[15] C. D. Koven, and I. Fung, 'Inferring dust composition from wavelength-dependent absorption in Aerosol Robotic Network (AERONET) data', *J. Geophys. Res.*, vol. 111, Nº D14, 2006.

[16] D. M. Pozar, *Microwave Engineering*, 2nd Ed., Wiley, 1998.

[17] T. Oguchi et al., 'Measurement of dielectric constant of volcanic ash erupted from five volcanoes in Japan', *IEEE Trans. Geosci. Remote Sens.*, vol. 45, Nº 4, 2009.

[18] A. H. Sihvola, 'How Strict are theoretical bounds for dielectric properties of mixtures?', *IEEE Trans. Geoscience and Remote Science*, vol. 40, Nº 4, pp. 880-886, 2002.

[19] K. K. Kärkkäinen, A. H. Sihvola, K. I. Nikoskinen, 'Effective Permittivity of Mixtures: Numerical Validation by the FDTD Method', *IEEE Trans. Geosci. Remote Sens.*, vol. 38, Nº 3, pp. 1303-1308, 2000.

[20] K. Kärkkäinen, A. Sihvola, K. Nikoskinen, 'Analysis of a Three-Dimensional Dielectric Mixture with Finite Difference Method', *IEEE Trans. Geosci. Remote Sens.*, vol. 39, Nº 5, pp. 1013-1018, 2001.

[21] R. S. Elliott, L. A. Kurtz, 'The design of small slot arrays', *IEEE Trans. Antennas Propag.*, pp. 214-219, 1978.

[22] R. S. Elliott, *Antenna theory and design*, Rev. Ed., IEEE Press, 2003.

[23] J. A. Rodríguez, F. Ares, E. Moreno, and G. Franceschetti, 'Design of shunt slot arrays without weak excitations', *Electron. Lett.*, vol. 35, pp. 1396-1397, 1999.

[24] T. V. Khac, and C. T. Carson, 'Impedance properties of longitudinal slot antenna in the broad face of rectangular waveguide', *IEEE Trans.*, 1973, AP-21, (5), pp. 708-710.

[25] R. S. Elliott, "An Improved Design Procedure for Small Arrays of Shunt Slots", IEEE Trans. Antennas Propag., vol. 31. Nº 1, pp. 48-53, 1983.

[26] R. S. Elliott, G. J. Stern, "Resonant Length of Longitudinal Slots and Validity of Circuit Representation: Theory and Experiment", IEEE Trans. Antennas Propag., vol. Ap-33, Nº. 11, 1264-1270, 1985.

[27] S. Rengarajan, M. Steinbeck, "Longitudinal Slots in Dielectric-Filled Rectangular Waveguides", Microw. Opt. Technol. Lett., vol. 6, Nº 11, pp 649-652, 1993.

[28] R. S. Elliott, W. R. O'Loughlin, "The Design of Slot Array Including Internal Mutual Coupling", IEEE Trans. Antennas Propag., vol. 34, Nº 9, pp 1149-1154, 1986.

[29] W. S. Kim, Y. H. Park, J. Y. Shin, and D. W. Lee, "Size Determination of Diesel Soot Particles Using Flow and Sedimentation Fiel-Flow Fractionation", Anal. Chem., vol. 71, pp. 3265-3272, 1999.

[30] Diesel Exhaust particle size, www.dieselnet.com, Rev. 2002.11

[31] D. B. Kittelson, W. F. Watts, and M. Arnold, "Review of Diesel Particulatte Matter Sampling Methods" University of Minnesota, Dept. Mechanical Engineering, Center for Diesel Research, 1998.

[32] A. A. Salas-Sánchez, M. E. López-Martín, J. A. Rodríguez-González, F. J. Ares-Pena, "A Novel Method for Determination of Suspended Particulate Matter in the Atmosphere Using Array Antennas", 1st URSI Atlantic Radio Science Conference, Gran Canaria, 2015.

[33] K. Chang, Y.H. Kim, Y.J. Kim and Y.J. Yoon, "Functional antenna integrated with relative humidity sensor using synthesised polyimide for passive RFID sensing," Electron. Lett., vol. 43, no.5, pp. 7-8, Mar. 2007.

[34] R.W.P. King, E.A. Aronson, C.W. Harrison, Jr., "Determination of the Admittance and Effective Length of Cylindrical Antennas," Radio Science, vol. 1, pp. 835-850, 1966.

[35] B.D. Popovic, and A. Nesic, "Generalisation of the concept of equivalent radius of thin cylindrical antennas," IEE Proc., Vol. 131, Pt. H, No. 3, June 1984.

[36] EM Software and Systems, FEKO Suite 6.3, (www.feko.info), 2014.

[37] E.A. Jones, W.T. Joines, "Design of Yagi-Uda Antennas Using Genetic Algorithms," IEEE Trans. Antennas Propagat., vol. 45, no. 9, pp. 1386-1392, Sept. 1997.

6 Monitoring of the electromagnetic field in a urban scenario.

Along this chapter we will described a simple and economical method for monitoring the electromagnetic field intensity in built-up areas. This method is based on the measurement of the field level over a discrete number of points at street level in the city and their transmission to an operative control center, where the field values all over the city are correctly interpolated in real time. Citizens might obtain these values at their sites, via Internet, or by connecting with a dedicated call center. Numerical evaluations of the electromagnetic field intensity via the new developed model and confirming experimental results are finally presented. All this work is published in [1].

6.1 Introduction

In this section, we examine one relevant problem among those concerning the quality life improvement of the citizens: simple and cheap evaluation of the electromagnetic field intensity (EMFI), aimed to control the exposure level of the citizens in the city environment. In the media the electromagnetic (EM) field is usually addressed as a pollutant, the electromagnetic smog, which is absolutely not appropriate: it is clear that if this smog is eliminated, the transmitted signal is eliminated, too, and the wireless transmission of information disappears. The right way to address the problem consists of monitoring the EMFI all over the city and checking that its level does not exceed the exposure limits.

However, the above measure does not provide the full solution to the problem. In fact, the periodic (usually wrongly documented) media's campaigns on the EM polluting smog issue generate unreasonable fever, fears, and worries within the population, who should be reassured, according to the following citation from the World Health Organization [2]: *Health is a state of complete physical, mental, and social well-being, and not merely the absence of disease or infirmity.* To this aim, informing each requesting citizen of their EMFI exposure level, at exactly the site where he/she is permanently or occasionally located, must be implemented.

We conclude that the EMFI must be continuously monitored, in space and time, and its value should be accessible to all requesting citizens.

Evaluation of several (real) pollutants in the cities has been already widely implemented, for instance, by measuring the particulate content of many substances in the atmosphere. However, very few attempts to systematically and continuously measure and map the EMFI in built-up areas have been experimented. Maps of the electromagnetic field coverage are provided by some web applications, e.g., [3]: they are obtained by collecting the received signal strength detected by mobile phones of cellular network users. However, the accuracy of these data is unknown, and often a numerical value is

not even provided but only some qualitative (high, low, etc.) information is indicated. All other methods are very costly, should a high-resolution map of EMFI be required: a very large number of measuring sensors should be disseminated within the city area, with the consequence of an unreasonable overall cost of acquisition of the instruments and operational expenses. An interesting exception is the method described in *Hasenfratz et al.* [4], where a few sensors mounted on the top of some public transportation vehicles in Zurich allow obtaining a map of the electromagnetic exposure level in that city. The final resolution of the map is $100m$, and only areas along or near to the route of the vehicles can be monitored. Conversely, we want to produce very high resolution (say $5m$) maps, covering given built-up areas, by using just a few cheap sensors [5]- [6].

As already noted, the measurement of the EMFI in the city arena is very simple: conventional sensors may be used, whose measured data can be transmitted to the operative control center (OCC) for their evaluation. However, two relevant issues must be considered. First of all, the EMFI is usually fast varying in space: for instance, if we turn around a building which is illuminated from one side, the field present at the other side may be totally different from the previous one. In addition, the field measured at the street level is changing if we move vertically along the building walls, attaining different values at different floors, balconies, terraces, and roof. A measurement system, reasonable and convenient, should make use of conventional hardware for implementing a limited number of field measurements together with additional appropriate software, the latter devoted to the interpolation of the local measured data over the entire city environment.

To this aim, in this work we propose, and fully describe, a technical solution for the control of the EMFI in the city environment, whose implementation is simple, effective, accessible, and, last but not least, of limited cost. The rationale of the solution we suggest is briefly described in the following.

The proposed evaluation of the EMFI in the city, at any site and any time, is based on the presence of a few measuring sensors distributed all over the city and on the intelligent use of a numerical software [7]- [9] that allows computation of the EMFI in the built-up areas, when the three-dimensional (3-D) topography of the city is prescribed, as well as the features of the EM radiating sources: locations of the antennas, input powers, radiation patterns, and their orientations.

Note that the input powers to the antennas may change over time, due to the corresponding telecommunication traffic intensity: the EMFI will change accordingly. However, a basic parameter about the EMFI distribution in the considered built-up area is desirable: we can get it by assuming a unitary input power for all the antennas and compute (only once) the corresponding EMFI, all over the points of interest in the explored area, by employing the above mentioned software, described and validated in *Franceschetti et al.* [7]- [9]. We show in the following that once this information has

been acquired, the possible EMFI change over space and time may be easily taken under control: a novel solver for the problem at hand is now available. The basic philosophy of this solver is synthetically presented in the next few lines.

Imagine that we distribute a limited number of EMFI-measuring sensors in the controlled built-up area and continuously transmit, in real time, these measured values to the OCC, where all the city parameters are stored, in particular the previously introduced basic EMFI distribution. It is obvious that basic and measured values of the EMFI would not coincide at the positions of the measurement points: as shown under section 6.2, proper processing of this evaluated discrepancy allows estimating the actual input powers of the operating antennas. When these input powers versus time are known, the EMFI level, at any point and any time all over the considered section of the city, can be evaluated in real time. In addition, each citizen can get the values of the EM field level at his/her site, at any time, either via Internet or by calling a dedicated call center.

The validity of the proposed system is confirmed by numerical simulations based on the developed physical model, followed by real experimental results.

In summary, this work presents a novel measuring system, whose implementation is simple: the required hardware is standard and available on the shelf, as well as the software codes utilized in the solver, which are present in the literature. Its innovative part is the intelligent processing of the measured data, leading to the real-time evaluation of the EMFI everywhere and anytime in the city, as already stated: we believe that this easy and economical implementation of the EMFI measuring system may lead to a new age in the control of 'pollutants' in the smart cities arena.

6.2 Description of the Method

Consider a built-up area, for which a digital description of the buildings and of the terrain is available. Let us assume that in this area M transmitting antennas are present, whose locations are known, as well as the radiation patterns of the antennas and their orientations. Conversely, their input powers x_m ($m = 1, \ldots, M$) are unknown. We want to evaluate the EMFI at the P points of a regular grid of prescribed spacing, covering the considered area. Here the EMFI is defined as the mean square modulus of the electric field; by assuming ergodicity, the latter is estimated by performing a time average of the square modulus of the electric field over a time interval of about 1 min, so reducing the fast fading effect. In addition, we reasonably assume that the fields radiated by different antennas are uncorrelated, so that the overall EMFI at each space point is the sum of the EMFIs radiated at that point by the different antennas.

Let us define A_{pm} the EMFI produced at the p-th grid point by the mth antenna,

when its input power is set equal to 1: it can be computed by using the software code presented in *Franceschetti et al.* [7]- [9], so that A_{pm} can be considered known. Based on the above cited assumptions, the actual overall EMFI yp at the pth grid point turns out to be the sum of the field intensities radiated by the unit power antennas, A_{pm}, each one multiplied by its actual (unknown at the moment) input power, x_m. Accordingly, we can formally write

$$y_p = \sum_{m=1}^{M} A_{pm} x_m \tag{58}$$

Let us now assume that we distribute, over N of the P grid points, N sensors designed to measure the overall EMFI y_n at their locations, with $n = 1, \dots N$. For instance, sensors described in *Ioriatti et al.* [10] can be used. Proper time averaging (over about 1 min of measurement for each sensor) is performed to reduce fast fading effects.

By applying (58) at the locations of the sensors (i.e., at the measurement points), we can write the following linear system.

$$A \cdot x = y \tag{59}$$

of N equations in M unknowns: A is now the N-row, M-column matrix, whose element A_{nm} represents the EMFI radiated by the mth unit power antenna at the n-th measurement point; x is the M-row column vector whose element x_m coincides with the m_{th} antenna unknown input power; and y is the N-row column vector whose element y_n is the actual EMFI value, measured by the sensor located at the n-th site.

At this point it seems that the problem of evaluating the input power x_m of each antenna, therefore allowing the subsequent computation of the EMFI all over the city, is satisfactorily solved: we can choose the number of sensors coincident with that of the antennas, i.e., $N = M$; the linear system (59) can be easily inverted; and evaluation of the EMFI, all over the city, can be computed by using (58). However, this is not the case, because the statistical presence of errors has been ignored and should be accounted for, as described hereafter.

The measured EMFIs $\hat{y}_n$ differ from actual ones yn due to (inevitable) measurement errors; similarly, the computed entries $\hat{A}_{nm}$ of the matrix A are (reasonably slightly) different from actual ones A_{nm}, due to the used software code (also here inevitable) inaccuracies.

The best procedure for decreasing the resulting errors is to increase the number of measurements, thus letting $N \geq M$ (but always $N << P$): this implies the presence of additional sensors, whose locations could be optimized. The input power of the antennas estimates x_m can be then obtained by solving the linear system (59) in the minimum square sense, i.e., by implementing the minimization procedure

$$\hat{x} = argmin|\hat{A} \cdot x - \hat{y}| \tag{60}$$

where $|\cdot|$ stands for the quadratic norm in $\mathbb{R}^N$, with the constraint that its solution $\hat{x}$ does not exhibit negative entries. This last requirement can be implemented by using one of the available constrained minimization methods (e.g., the generalized reduced gradient method [11]) or by minimizing (60) with respect towm $w_m = \sqrt{x_m}$ (so that nonnegative values of $\hat{x}_m = \hat{w}_m^2$ are guaranteed) by using one of the available global optimization methods (e.g., simulated annealing [12]).

Once the input powers of the antennas have been computed, the field intensity at any grid point of the scene, i.e., the city, can be evaluated by using (58)

$$\hat{y} = \sum_{m=1}^{M} \hat{A}_{pm}\hat{x}_m \tag{61}$$

We conclude that a complete map of EMFI, at the requested space resolution, is available. Obviously, the attainable precision of the final EMFI evaluation must be assessed: this point is discussed in section 6.3.

Note that for a large scene with many buildings and many antennas (for instance, an entire city), the time needed by the ray-tracing software tool to compute the field radiated by each one of the M antennas in the whole area may be very large. However, this computation must be performed only once, in a preliminary phase, whereas computation of the input powers of the antennas via minimization of (60), and subsequent evaluation of the field level map via (61), requires a very short time. Accordingly, the field level map can be updated in real time, just following the change in the measurement of the sensors.

It is finally worth mentioning that the software code assumes sinusoidal signals at frequencies corresponding to the carriers' ones, whereas actually the signal power is spread over a finite bandwidth. However, the latter is very small with respect to the carrier frequency, so that for our purposes the pure sinusoid approximation is acceptable.

6.3 Sensitivity to Error Sources

We believe that the procedure, detailed in the previous sections, and leading to a novel measurement system aimed to control the EMFI level in built-up areas, is theoretically valid and applicable; however, its valuable use in the smart cities scenario requires an analysis of the effects generated by possible error sources, as anticipated under section 6.2. In fact, the measurements performed by the sensors distributed in the area under control are affected by errors; the accuracy of the numerical software model we use for computing the EMFI in built-up areas should be accounted for; and last, but certainly not least, the precision of our developed procedure, summarized by equation (60), must

be assessed. This is not an easy job: all these factors are strongly interlaced in our developed procedure, and the evaluation of their specific relevance requires some effort. In the following, we preliminarily perform a theoretical sensitivity analysis (section 6.3.1) and then we present some numerical results for simulated scenarios (section 6.4).

6.3.1 Theoretical Analysis

Let us first consider the effect of the measurement errors of the sensors. We define Δy the column vector of measurement errors, so that $\hat{y} = y + \Delta y$, and Δx the column vector of the corresponding errors on the transmitted powers, so that $\hat{x} = x + \Delta x$. Then, equation (59) can be modified as

$$A \cdot (x + \Delta x) = y + \Delta y \tag{62}$$

It can be shown that [see, e.g., *Franceschetti* [13], chapter 6; *Gander et al.* [14], chapter 6]

$$\frac{|\Delta x|}{|x|} \leq k_A \frac{\Delta y}{y} \tag{63}$$

where k_A is the condition number of the matrix A, i.e., the ratio of the maximum to the minimum singular value of A. This means that the relative error on the retrieved power is of the same order as the relative error on the measurements, unless the condition number of A is high, i.e., unless A is ill conditioned. We explicitly note that for a given environment, k_A depends on the positions of the sensors: this analysis then shows that an inappropriate choice of these positions may lead to large retrieval error even in the presence of very small measurement errors. As a worst case, for a very high condition number, i.e., for a totally inappropriate choice of the positions of the sensors, even in the absence of sensor measurement errors, very small machine rounding errors may lead to very large errors in the retrieved power. We will show an example of this in section 6.4.

Let us now consider the inaccuracy of the employed ray-tracing software model. The latter leads to errors on the elements of the matrix A, so that if we call ΔA the matrix of the errors, then equation (59) can be modified as

$$(A + \Delta A) \cdot (x + \Delta x) = y \tag{64}$$

If we define the norm $|A|$ of a matrix as its maximum singular value, then it can be shown that a result similar to (63) holds [13]- [14].

$$\frac{\Delta x}{x} \leq k_A \frac{\Delta A}{A} \tag{65}$$

so that the relative error on the retrieved power is of the same order as the relative error on the EMFI computed by the ray-tracing software, unless A is ill conditioned. Considerations on the role of the positions of the sensors similar to those made above

hold in this case, too.

In practice, the two kinds of inaccuracies are present at the same time. In this case, if both the correspondent relative errors are small (not larger than 0.1, i.e., 10%), then the relative error on the retrieved power is with good accuracy the sum of the two right-hand sides of (63) and (65). However, the error may be much larger than that if relative errors are not small. For instance, if the relative error on A (i.e., inaccuracy of the software model) is small but the one on y (i.e., inaccuracy of the measurements of the sensors) is not, then the relative error can be computed as [14].

$$\frac{|\Delta x|}{|x|} \leq \left(2k_A + k_A^2 \frac{|\Delta y|}{|y|}\right) \frac{\Delta A}{A} + k_A \frac{\Delta y}{y} \tag{66}$$

In conclusion, we theoretically expect that the relative errors on the retrieved transmitted power, and hence on the EMFI retrieved by our method, are of the same order as those on the measurements of the sensors and on the computations of the ray-tracing software, if the latter are sufficiently smaller than unity, provided that attention is paid to the choice of the positions of the sensors. These findings are substantially confirmed and better quantified by the simulations reported in section 6.4.

6.4 Result for Simulated Scenarios

We show in the following how valuable information can be gathered by implementing a simulated virtual scenario. For a prescribed topography of the city section under control, with assumed number and locations of radiating antennas and measuring sensors, we generate the EMFI values all over the city section by using the above mentioned ray-tracing software, with prescribed input power for each radiating antenna (the 'true' power values). We call these EMFI values, computed by the software at the locations of the sensors, virtually measured field (VMF) values; measurement errors due to the receiver noise of the sensors may be simulated by adding to them normally distributed random errors. These VMF values are then provided as inputs to our developed algorithm (see section 6.2). Finally, estimated antenna input powers are compared with the originally prescribed (true) ones, and the EMFI retrieved by the virtual measurements may also be compared with those computed at the beginning.

It is explicitly noted that the accuracy of the ray-tracing software model (see section 6.2) cannot be assessed in this process: the model is used to simulate the measurements, as well as to implement the procedure for both the input power retrieval of the antennas and the EMFI evaluation all over the city section. Accordingly, the same tool is behind the complete simulation, irrespective of its accuracy that must be accepted with no possible evaluation. This is at variance of the real experimentation (see section 6.5), where both measurements error and software model inaccuracy play their distinct roles.

In the following, we report the results of two simulated virtual experiments, referred to as two urban areas, A and B, in the same city but of very different extensions and geometrical distribution and heights of the buildings. The reason is to verify the validity of the solver in different surroundings and to individuate possible critical situations worthy of additional examination.

6.4.1 Scenario A

In this first scenario, we explore the relevance of the relative number of antennas, M, and (virtual) sensors, N, as far as the precision of the implemented solver is concerned. In addition, some preliminary observations about the choice for the (virtual) sensors locations are also included.

We consider an about $700 \times 700m^2$ urban area within the city of Napoli (downtown, see Fig. 44), Italy. Three transmitting dipole antennas (crosses) and five virtual sensors (dots), both shown in the map of Fig. 45, are assumed to be distributed in that area. The three maps of the field intensities produced by each one of the three antennas, as computed by the ray-tracing software code, are depicted in Fig. 46.B. Two successive cases are considered: absence or presence of errors in the measurements.

When measurements are error free, very small errors spoil the retrieved input powers of the antennas: these errors are substantially independent from the number of the virtual sensors, as illustrated in Table 22, and as theoretically expected, the reliability of our algorithm is validated. However, attention must be paid to the distribution of the virtual locations of the sensors. As a matter of fact, let us make reference to Fig. 45 and Table 22 and recall the virtual sensors by their reference numbers: let us make use of virtual sensors 1, 2, and 5 instead of 1, 2, and 3. Then, the completely wrong value of $23W$ is obtained for the retrieved input power of antenna 2. This unacceptable result can be easily explained: the EMFI radiated by antenna 2 at points 1, 2, and 5 is extremely low (compare Fig. 45 with Fig. 46), so that the field values at those points are substantially insensitive to the value of the input power of antenna 2. Accordingly, this lack of necessary information renders difficult the retrieval of this antenna input power.

It is noted that the above point does not imply a limitation of the innovative algorithm we present: as a matter of fact, the problem disappears if the number of sensors is slightly larger than the number of radiating antennas and/or the locations of the sensors are properly chosen. In addition, optimization of the locations of the sensors can be heuristically achieved by repeating the simulations while varying sensor locations. This does not imply that a theoretical analysis of the optimization process is impossible: an interesting road to pursue is presented in the chapter of 'Conclusions'.

The presence of measurement errors is now considered by adding zero-mean normally distributed random errors, with prescribed standard deviation, to the computed (i.e.,

'error-free') fields at the virtual locations of the sensors. Results of this simulated experiment, in terms of retrieved antenna input powers, are summarized under Table 23, for different values of the measurement error standard deviation σ. Power values reported in this table are obtained by averaging over 20 VMF values, obtained by using 20 different realizations of the random VMF linear vector. In the considered scenario, the retrieved power values are in reasonable agreement with the actual ones, even with values of the measurement error standard deviation as high as 0.01 V/m. In particular, the relative mean errors (i.e., the estimation biases) are not larger than about 10%,and standard deviations of the retrieved power values are smaller than 0.1 W in all cases, so that also the relative uncertainty is not larger than about 10%.

For lower values of the measurement error standard deviation, results are almost independent of the latter, and they are coherent with values of Table 22, thus suggesting that in those cases the main sources of retrieval error are the minimization algorithm inaccuracies.

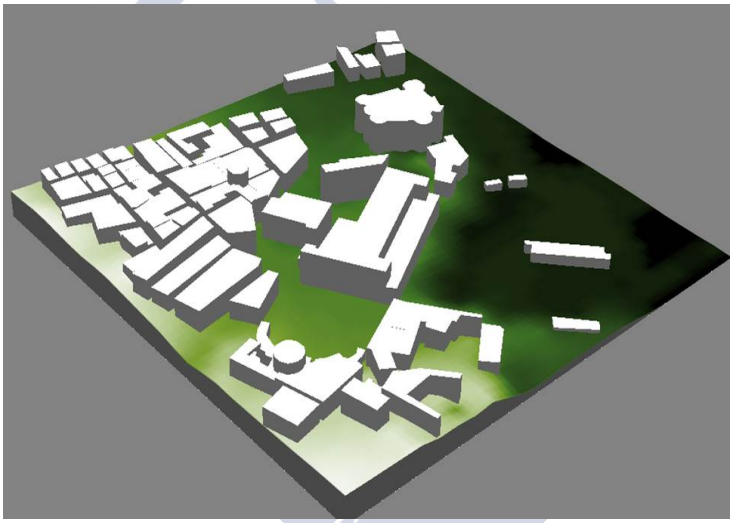

Figure 44: 3-D coarse prospect of the considered scene (section of Naples downtown area).

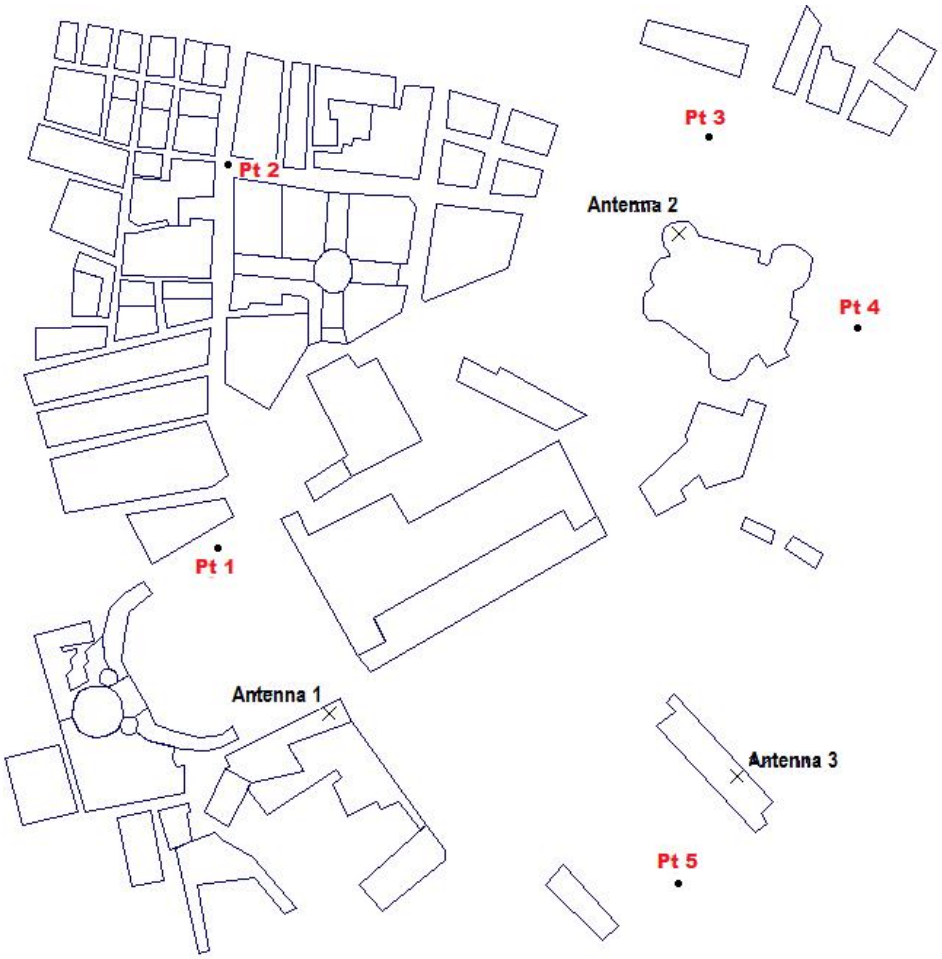

Figure 45: Location of antennas (crosses) and virtual measurement sensors (dots), in the same area depicted in Fig. 44.

Table 22: Actual and retrieved antenna input powers for different number of virtual sensors[a]

	Actual	Retrieved Input Powers		
# Antenna	**Input Powers** W	**Sensors 1-3** W	**Sensors 1-4** W	**Sensors 1-5** W
1	5.00	4.90	4.80	4.90
2	0.80	0.81	0.81	0.81
3	2.50	2.30	2.40	2.30

[a] Location of the virtual sensors is depicted in Fig. 45

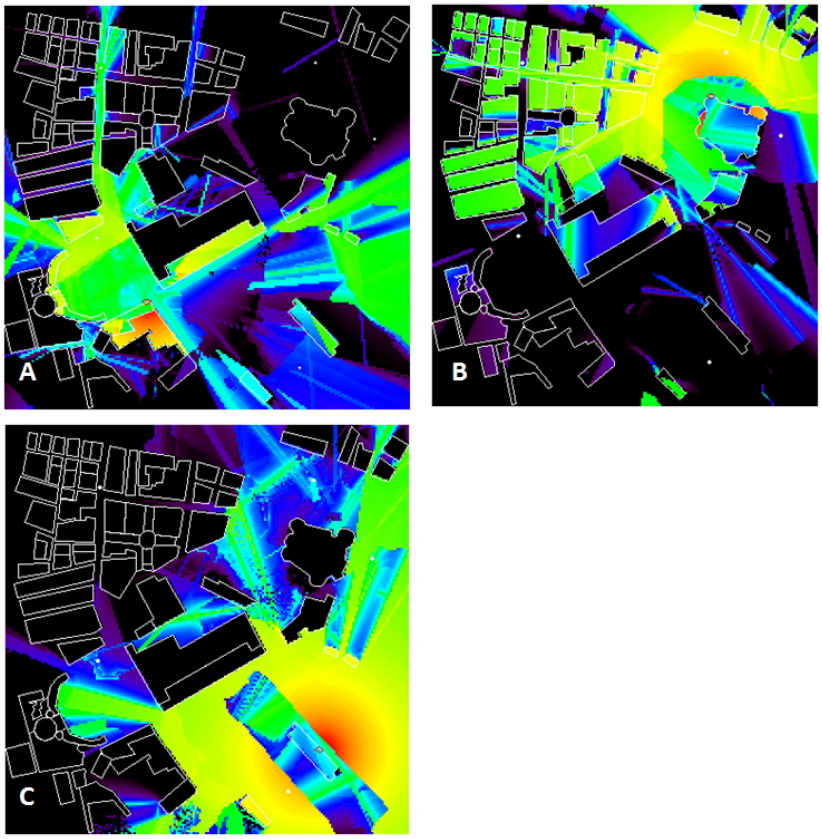

Figure 46: Maps of the EMFI radiated by antennas 1 (A), 2 (B) and 3 (C). False color logarithmic intensity scale increasing from black to red. The area is the same as depicted in Figs. 44 and 45. Virtual sensors are indicated by white dots.

Table 23: Scenario of Fig. 44: Actual and retrieved antenna input powers for different values of the measurement error standard deviation σ^a.

	Actual	Retrieved Input Powers		
# Antenna	**Input Powers**	$\sigma = 0.0001\ V/m$	$\sigma = 0.001\ V/m$	$\sigma = 0.01\ V/m$
1	$5.000\ W$	$4.840 \pm 0.001\ W$	$4.840 \pm 0.002\ W$	$5.400 \pm 0.100\ W$
2	$0.800\ W$	$0.810 \pm 0.001\ W$	$0.810 \pm 0.001\ W$	$0.710 \pm 0.090\ W$
3	$2.500\ W$	$2.340 \pm 0.001\ W$	$2.330 \pm 0.002\ W$	$2.000 \pm 0.050\ W$

[a] The error-free amplitude of the (virtually measured) electric field at the five sensors sites are $0.145V/m$, $0.059V/m$, $0.052V/m$, $0.143V/m$, and $0.087V/m$.

6.4.2 Scenario B

As a second case, we consider another almost 6 times larger urban area (about 1700×1700 m^2) in the city of Napoli (see Fig. 47, Napoli Central Station), with the same number of radiating antennas (three) and (virtual) measurement sensors (five). As already anticipated, this is to confirm the results of section 6.4.1, and explore the dependence of the results with reference to the spacing between antennas and sensors, including the relevance of the additional parameter signal-to-noise ratio (SNR, where noise is measurement noise).

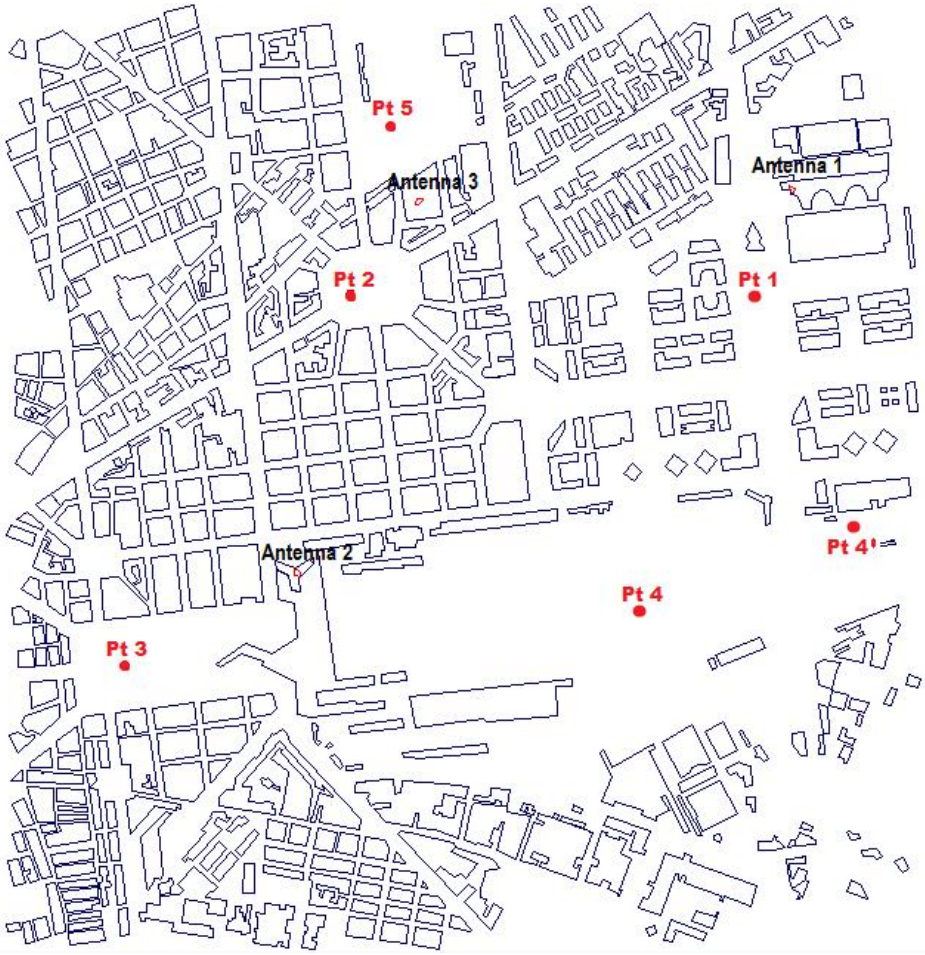

Figure 47: Map of the other city area, Napoli Central Station. Location of antennas and virtual measurement sensors are indicated. The alternative virtual sensor at point Pt 4' is also added, for an additional experiment described in this sub-Section.

The EMFI map generated by the joint presence of all the three antennas is depicted under Fig. 48. As in the previous case, let us first consider error-free measurements. The retrieved antenna input powers are in this case very accurate, independently of the

considered number of sensors: obtained errors are always not larger than 0.02 W, and they are reported in Table 24.

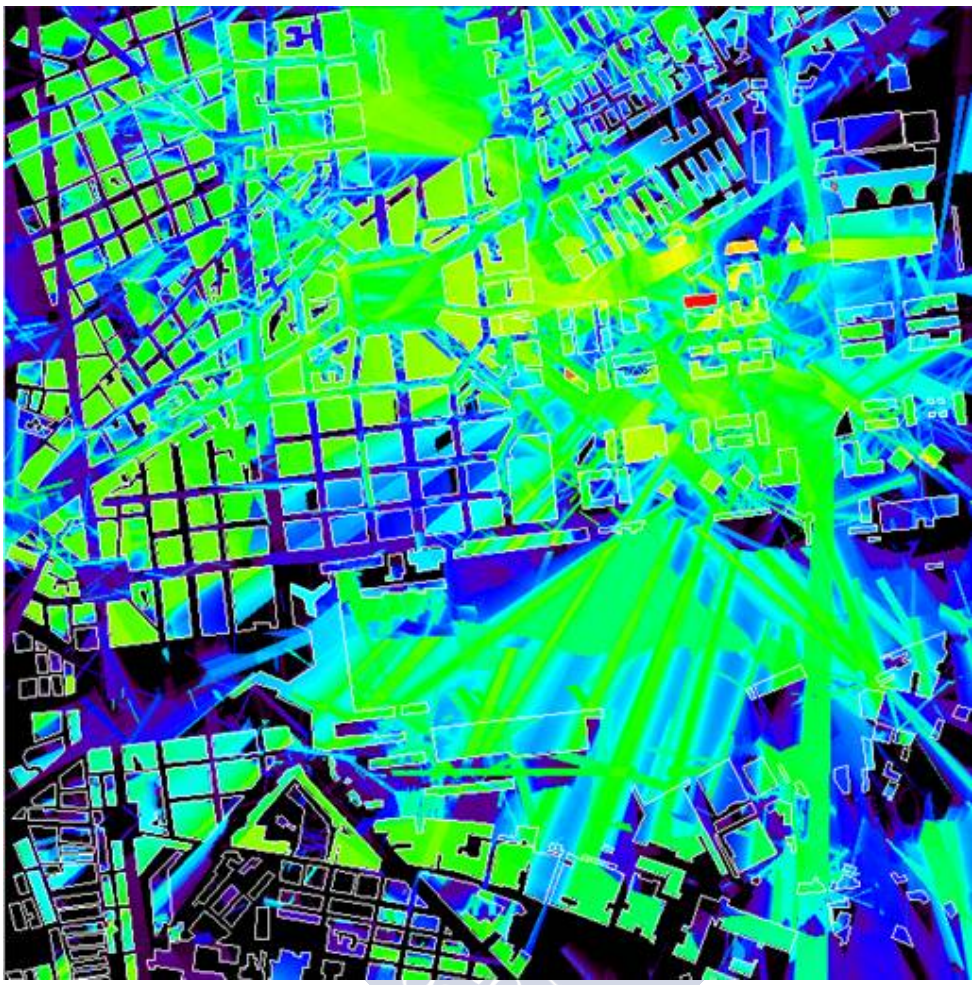

Figure 48: Map of the other city area, Napoli Central Station. Location of antennas and virtual measurement sensors are indicated. The alternative virtual sensor at point Pt 4' is also added, for an additional experiment described in this sub-Section.

By moving to the inclusion of measurement errors, we consider all the five virtual sensors of Figure 47 and analyze the behavior of the method for different values of the measurement error standard deviation σ. Actual and retrieved antenna input powers are compared in Table 25.

As in the previous case, power values reported in Table 25 have been obtained by averaging over 20 different realizations of the random VMF linear vector. Standard deviations of the retrieved power values are smaller than 0.1 W in all cases, except for the measurement error standard deviation equal to 0.1 V/m. For this high value of the

standard deviation, comparable to the error-free field values, retrieved antenna input powers are not in agreement with the actual ones, as expected. However, for lower values of the measurement error standard deviation, retrieved values are in good agreement with the actual ones, with relative errors not larger than 10%, and conclusions similar to those achieved in the previous scenario can be drawn.

Results obtained by varying position and number of sensors can be now considered: these are illustrated in Fig. 49, for the assumed measurement error standard deviation $\sigma = 0.01\ V/m$. This plot shows that the retrieval error rapidly converges to a very small value for a number of sensors slightly larger than the number of antennas. This small error limiting value is about 0.025 W (see Fig. 49.D), in agreement with the results obtained for error-free measurements.

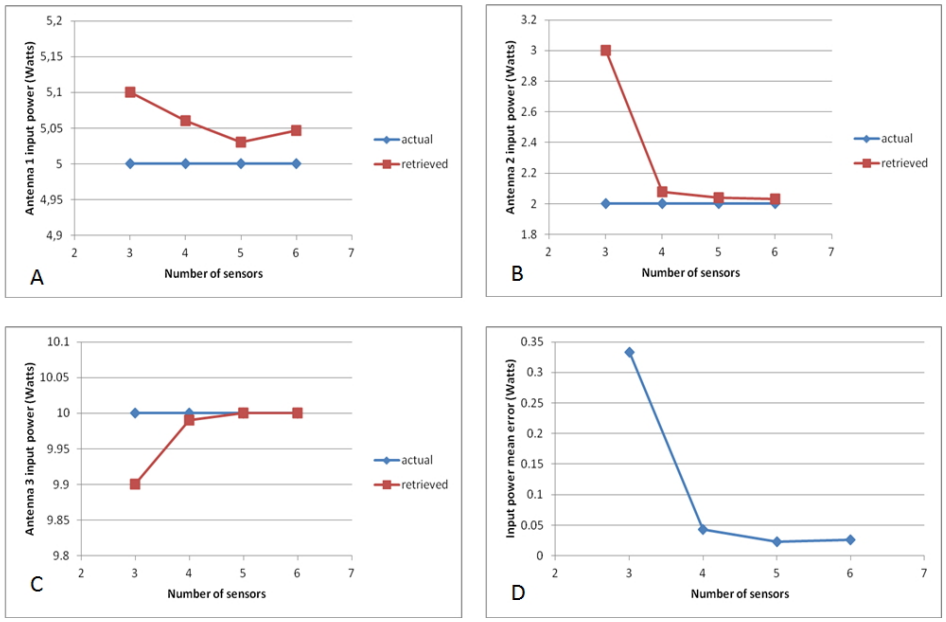

Figure 49: True and retrieved input powers, for the three antennas of Fig. 47, vs. the numbers of (virtual) measurement sensors (A-C). For the same scenario, overall mean error on the retrieved input power vs. number of virtual sensors (D). Measurement error standard deviation σ is equal to 0.01 V/m.

The relevance of the signal-to-noise ratio (SNR, where noise is measurement noise) has been also explored: it should be sufficiently large for a sufficient number of sensors, in order to get acceptable results. To show this, in the case of five virtual sensors and $\sigma = 0.01\ V/m$, let us move the fourth virtual sensor from point 4 to point 4' (see Fig. 47), so that its error-free (virtually) measured field decreases from 0.134 V/m to 0.008 V/m: only for sensors 1, 2, and 5 the SNR is higher than 10 dB, whereas for sensors 3 and 4 the measurement error is of the same order as the error-free field value. The comparison

of results obtained with these two different positions of the fourth sensor is reported in Table 26: the retrieved values of the input powers for the three antennas are clearly worse if the fourth sensor is moved to point 4'. This and similar virtual experiments, combined with the previous ones (see Tables 23 and 24), seem to suggest that very accurate results are obtained as long as the signal-to-noise ratio is larger than 10 dB for at least 4 sensors (i.e., the number of antennas plus one). As expected, the result is that the considerations on the spatial distribution of the sensors, made for the case of error-free measurements (see section 6.4.1), remain valid also when noisy measurements are considered.

As a conclusion for section 6.3, the results of the simulated experiments are very satisfactory: retrieved input powers of the operating antennas are very good. And it is very comfortable that in wide areas with intense space variations of the EMFI distribution (as in the example of Fig. 48), the electromagnetic field intensity can be monitored and taken under control by using a number of sensors slightly larger than those of the operating antennas. With more details, we can summarize the results of this section as follows.

1. In the case of error-free measurements, errors of the algorithm are very small (relative errors smaller, often much smaller, than 5%), provided that at least one sensor is included in the coverage area of each transmitting antenna.

2. Errors due to measurement inaccuracies are small (relative error not large than 10%), provided that SNR is larger than 10 dB for a number of sensors slightly larger than those of the operating antennas.

3. For very high SNR, very small errors (relative errors smaller, often much smaller, than 5%) may be still present, probably due to the minimization algorithm inaccuracies.

4. By increasing the number of (virtual) sensors, the errors rapidly converge to a very small value for a number of sensors slightly higher than the number of antennas.

With regard to the effect of the accuracy of the numerical software model, no information can be obtained from the simulated experiments. However, it is known in literature that for the ray-tracing prediction tools, root-mean-square (RMS) errors on the computed electric field ranging from about 2–3 dB to about 7–10 dB may be expected, according to the accuracy of the description of the buildings (see, e.g., *Franceschetti et al.* [8], *Bertoni* [15], *Rizk et al.* [16], *Yun et al.* [17]). Accordingly, accuracies of the same order should be expected for the proposed monitoring method, when other sources of errors are taken under control as explained above. This is verified in the next section, where a real scenario is considered. Note that the error on the electric field reported above is defined as the difference between the values in $dB\ V/m$ of estimated and true fields, so that it is expressed, as usually done, in decibels. It is also worth mentioning that in the wireless telecommunication technical jargon, the field level is often directly expressed in terms of

the corresponding received power (i.e., the 'received signal strength', RSS), so that it is measured in dBm (i.e., decibels with respect to 1 mW). However, the difference between field numerical values in $dB\ V/m$ and dBm is a constant, so that the relative error in decibels is independent from the choice of the field measurement unit.

Table 24: Actual and retrieved antenna input powers for different numbers of virtual sensors[a].

		Retrieved Input Powers		
# Antenna	**Actual Input Powers**	3 virtual sensors (Numbers 1-3)	4 virtual sensors (Numbers 1-4)	5 virtual sensors (Numbers 1-5)
1	5.00 W	4.99 W	4.99 W	5.00 W
2	2.00 W	1.98 W	1.98 W	1.98 W
3	10.00 W	10.01 W	9.99 W	10.00 W

[a] Location of the virtual sensors is depicted in Fig. 47

Table 25: Scenario of Fig. 47: Actual and retrieved antenna input powers for different values of the measurement error standard deviation σ[a].

	Actual	Retrieved Input Powers		
# Antenna	**Input Powers**	$\sigma = 0.001\ V/m$	$\sigma = 0.01\ V/m$	$\sigma = 0.1\ V/m$
1	5.000 W	$5.000 \pm 0.001\ W$	$5.00 \pm 0.02\ W$	$9.2 \pm 2.6\ W$
2	2.000 W	$1.950 \pm 0.002\ W$	$2.1 \pm 0.1\ W$	$28.1 \pm 22\ W$
3	10.000 W	$10.000 \pm 0.001\ W$	$10.00 \pm 0.02\ W$	$11.7 \pm 2.5\ W$

[a] The error-free amplitude of the (virtually measured) electric field at the five sensors sites are $0.322V/m$, $0.245V/m$, $0.025V/m$, $0.134V/m$, and $0.991V/m$.

Table 26: Scenario of Fig. 47: Actual and retrieved antenna input powers for two different positions of the fourth sensor.

	Actual	Retrieved Input Powers for $\sigma = 0.01V/m$	
# Antenna	**Input Powers**	Fourth sensor un Point 4	Fourth sensor un Point 4'
1	5.000 W	$5.00 \pm 0.02\ W$	$7.35 \pm 1.15\ W$
2	2.000 W	$2.1 \pm 0.1\ W$	$15.4 \pm 9.7\ W$
3	10.000 W	$10.00 \pm 0.02\ W$	$10.02 \pm 0.18\ W$

6.5 Results for a Real Scenario

Full validation of the proposed technique requires a comparison of the obtained EMFI map with results of a real (and not virtual) measurement campaign. A first experiment is described in the following.

Another $1100 \times 1100m^2$ urban section of the city of Napoli (Fuorigrotta area) has been selected, and the 1800–1880 MHz band has been considered: locations and properties of cellular system base stations, present in the area and operating in this band, have been provided by the locally operating mobile telephone companies. The map of the area, with the current base stations, is depicted in Fig. 50. Each base station may host one, two, or three transmitting antennas: in the latter cases, antenna pointing directions are different. The total number of transmitting antennas is equal to 11.

Unfortunately, our available number of measurement (real, not virtual) sensors was not sufficient to perform all the measurements at the same time, as it should be in any operative phase. Instead, we were forced to make use of a single sensor (namely, an *Aaronia Spectran* spectrum analyzer [18]) located on a moving truck. Time intervals of some minutes between any couple of subsequent measurement points took place. These delays are clearly affecting results of the measuring solver and should be accounted for when evaluation of the experiment results is performed.

We have considered 11 measurement points: the EMFI values at these points have been used as input of our algorithm. We have also measured the EMFI in two more points (referred to as verification points), just for checking purposes. Locations of measurement and verification points for this campaign are shown in Fig. 51. The maximum value of the measured electric field has been equal to 0.36 V/m.

Comparison of measured and computed (via the procedure described in section 6.2) EMFI are reported in Fig. 52 for both measurement and verification points: the overall RMS error is 3.06 dB, whereas the RMS error in the verification points is 3.72 dB. In all the cases, the errors on electric field in linear and logarithmic units are below (often well below) 0.03 V/m and 6 dB, respectively. Results provided here have been obtained by using a simulated annealing algorithm, but similar results have been obtained by using the generalized reduced gradient method. All these results appear to be very promising.

We also tried to increase the number of measurement and verification points (up to 16 measurement and 7 verification points), but results turned out to be less accurate (overall RMS error was about 5 dB), which is seemingly inconsistent with results of the previous section. However, collecting this larger number of measurements required a much larger time interval with our sensor moving on a truck. Accordingly, the deviation from the operative configuration of measurements, all synchronized at the same time, is clearly higher, and deterioration of the obtained results is expected.

Figure 50: Map of the city (Fuorigrotta area) section with locations of transmitting antennas. Different colors refer to different telephone companies.

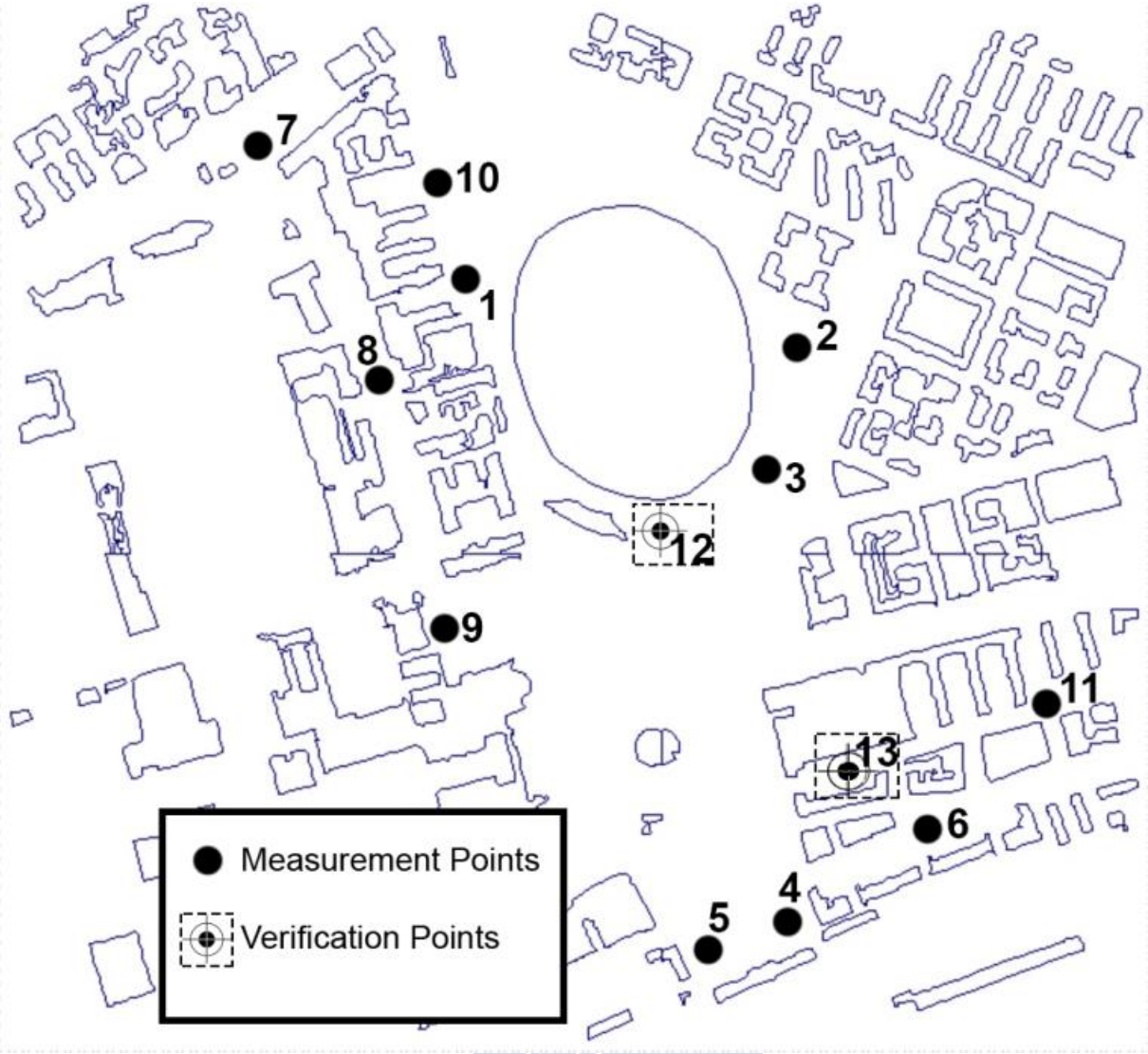

Figure 51: Map of the same city area depicted in Fig. 50, with the locations of measurement and verification points.

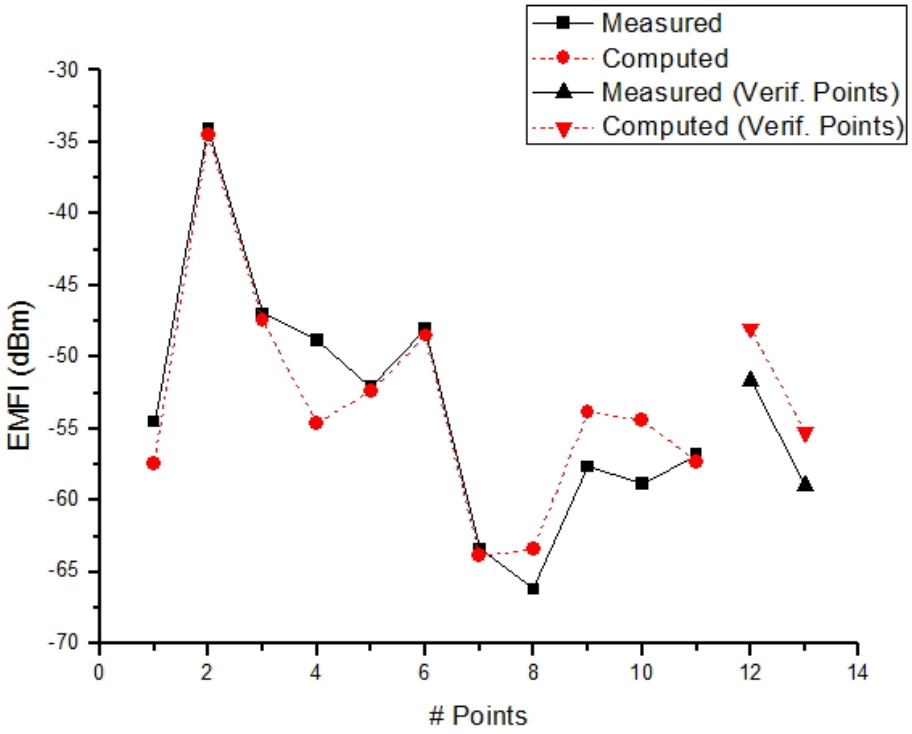

Figure 52: Measured and computed EMFI in measurement and verification points.

In conclusion, results of our measurement campaigns, combined with considerations on ray-tracing software accuracy at the end of section 6.3, suggest that full implementation of the proposed method would lead to RMS errors of the order of 3 dB over the EMFI. If the aim of the field monitoring is to check that its level does not exceed the EMFI exposure limits, this means that no further action is needed as long as all values in the output EMFI map are more than 3 dB below the required limits. On the other side, for points where the EMFI values range from 3 dB below to 3 dB over the exposure limit, i.e., they are within the $\pm$ dB RMS measurement error, some additional exploration is needed to check the actual value of the field therein. Finally, points for which the EMFI values are more than 3 dB over the limit require actions to reduce the field level, because they escape the security limits. It is worth noticing that exposure limits may significantly vary for different countries. In the European Union (EU), Recommendation 1999/519/EC prescribes a limit of 58 V/m at 1800 MHz band, but some EU countries enforced stricter limits, up to 10 times lower than EU recommendation. For instance, in Italy the limit for places where people stay for more than 4 h is 6 V/m.

References

[1] Francisco J. Ares-Pena, Giorgio Franceschetti, Antonio Iodice, and Aarón A. Salas-Sánchez, 'Simple and effective monitoring of the electromagnetic field in the smart cities arena,' *Radio Science*, vol. 51, pp. 1249-1262, Aug. 2016.

[2] World Health Organization, Preamble to the Constitution of the World Health Organization as adopted by the International Health Conference, New York, 19 June–22 July, 1946.

[3] OpenSignal. Available at http://opensignal.com/about/.

[4] D. Hasenfratz, S. Sturzenegger, O. Saukh, and L. Thiele, 'Spatially resolved monitoring of radio-frequency electromagnetic fields,' in Proceedings of SenseMine'13, pp. 1–6, ACM, Rome, Italy, 2013.

[5] G. Franceschetti, and A. Iodice, 'Electromagnetic propagation and field level control in smart cities,' in Proceedings of the Spanish URSI Meeting, pp. 1–4, URSI, Santiago de Compostela, Spain, 2013.

[6] G. Franceschetti, and A. Iodice, 'Measurement of electromagnetic field intensities in built-up areas,' in Proceedings of the Italian AMTA Node Conference, p. 1, AMTA, Salerno, Italy, 2015.

[7] G. Franceschetti, A. Iodice, D. Riccio, and G. Ruello, 'A tool for planning electromagnetic field levels in urban areas,' in Proceedings of the Antennas and Propagation Society International Symposium, vol. 3, pp. 2211–2214, IEEE, Monterey, California, USA, 2004.

[8] G. Franceschetti, R. Guida, A. Iodice, D. Riccio, and G. Ruello, 'Verifica di un software per la previsione della radiocopertura Atti della XVI Riunione Nazionale di Elettromagnetismo,' Genova (Italy), pp. 170-173 (in Italian), 2006.

[9] G. Franceschetti, P. Imperatore, A. Iodice, and D. Riccio, 'Radio-coverage parallel computation on multi-processor platforms,' in Proceedings of the 39th European Microwave Conference, pp. 1575–1578, IEEE, Rome, Italy, 2009.

[10] L. Ioriatti, M. Martinelli, F. Viani, M. Benedetti, and A. Massa, 'Real-time distributed monitoring of electromagnetic pollution in urban environments,' in Proceedings of the *IEEE International Geoscience and Remote Sensing Symposium*, V100–V103, IEEE, Cape Town, 2009.

[11] L.S. Lasdon, and A. D. Waren, 'Generalized reduced gradient software for linearly and nonlinearly constrained problems,' in Design and Implementation of Optimization Software, edited by H. Greenberg, Sijthoff and Noordhoff, pp. 363–396, Springer, New York, 1979.

[12] S. Kirkpatrick, C. D. Gelatt Jr., and M. P. Vecchi, 'Optimization by simulated annealing,' *Science*, vol. 220(4598), pp. 671–680, 1983.

[13] G. Franceschetti, Electromagnetics: Theory, Techniques, and Engineering Paradigms, Springer, Boston, Massachusetts, USA, 1997.

[14] W. Gander, M. J. Gander, and F. Kwok, Scientific Computing – An Introduction Using Maple and MATLAB, Springer, Switzerland, 2014.

[15] H. L. Bertoni, Radio Propagation for Modern Wireless Systems, Prentice Hall, Englewood Cliffs, New Jersey, USA, 2000.

[16] Rizk, K., J.-F. Wagen, and F. Gardiol, 'Influence of database accuracy on two-dimensional ray-tracing-based predictions in urban microcells,' *IEEE Trans. Veh. Technol.*, Vol. 49, No. 2, pp. 631–642, 2000.

[17] Yun, Z., S. Y. Lim, and M. F. Iskander, 'Use of geospatial resources for radio propagation prediction in urban areas,' *Antennas and Wireless Propag. Lett.*, Vol. 8, pp. 587–591, 2000.

[18] Aaronia (Spectrum Analyzer HF-60100 V4), technical data and information. Available at http://www.aaronia.com/products/spectrum-analyzers/HF-60100-V4-EMC-Spectrum-Analyzer/.

7 Simulation of Specific Absortion Rate problem in rats.

In this chapter different techniques for specific absortion rate (SAR) estimations will be discussed. All these procedures were developed by using the FDTD-based software SEMCAD [2]. This software was combined with the use of a Sprague-Dawley numerical (voxel) phantom rat, weighting $198.3g$ and composed of 60 different tissues assembled by slices $1.15mm$.

7.1 Experimental Setup

In both cases the experimental setup is quite similar. The difference between studies is on the number of frequencies used on each one. For the first, only one frequency is used and for the second, a simultaneous exposure of two different frequencies has been investigated.

Fig. 53 shows the experimental setup. Two vector signal generators, VSG1 and VSG2, generate pure sinusoidal signals of 2450 and 900 MHz, respectively, at the required power levels. Their outputs are combined in a signal mixer (SM), and the signal is then passed through an amplifier (AMP) and a directional coupler (DC) before entering the $125 \times 65 \times 35$ cm GTEM radiation chamber [3], where the rat (R), immobilized in a plexiglass holder (RH), is positioned in the region of maximum field uniformity (approximately $15 \times 15 \times 8$ cm for a maximum variation of 3 dB) [3]. Despite this position, since the EM wave hits the rat broadside (with E perpendicular and H parallel to its midline), its right side is to some degree shielded by its left side.

The DC enables measurement of incident power values (P_{IN}) by the power meter (PM) and of reflected power (P_{REF}) by the spectrum analyser (SA); the SA also enables observation of the wave configuration in the chamber and hence verification of spectral purity. An isotropic probe (IP) is used to map the field in the ratless chamber, which serves not only to identify the optimal position of the rat, but also to calibrate input power and the parameters of the simulations used for SAR estimation. It is preferable to use these measurements rather than the field formula recommended by the chamber manufacturer [3] because the latter, $E = \sqrt{\frac{Z_0 P_{TR}}{h^2 \zeta}}$ (where h is the height of the septum at the position of the rat, $P_{TR} = P_{IN} - P_{REF}$, $Z_0 = 50$ [Ω] is the GTEM input impedance, and ζ is a ripple-dependent coefficient that is taken equal to 2 [3]), fails to take into account the presence of more than one frequency.

The experimental rat (R) was immobilized in a methacrylate holder and placed in the region of maximum field uniformity inside the Gigahertz Transverse Electromagnetic (GTEM) chamber [3]. The animal was then exposed to radiation for one or two hours. The experimental system used for applying radiation to the rats is described in *López-Furelos et al.* [1] and a small explanatory diagram is provided here in Fig. 53. Direct

Current enables measurement of incident power values (P_{IN}) by the PM and of reflected power (P_{REF}) by the SA, making it possible to determine the power transmitted (P_{TR}) to the GTEM chamber as $P_{TR} = P_{IN} - P_{REF}$.

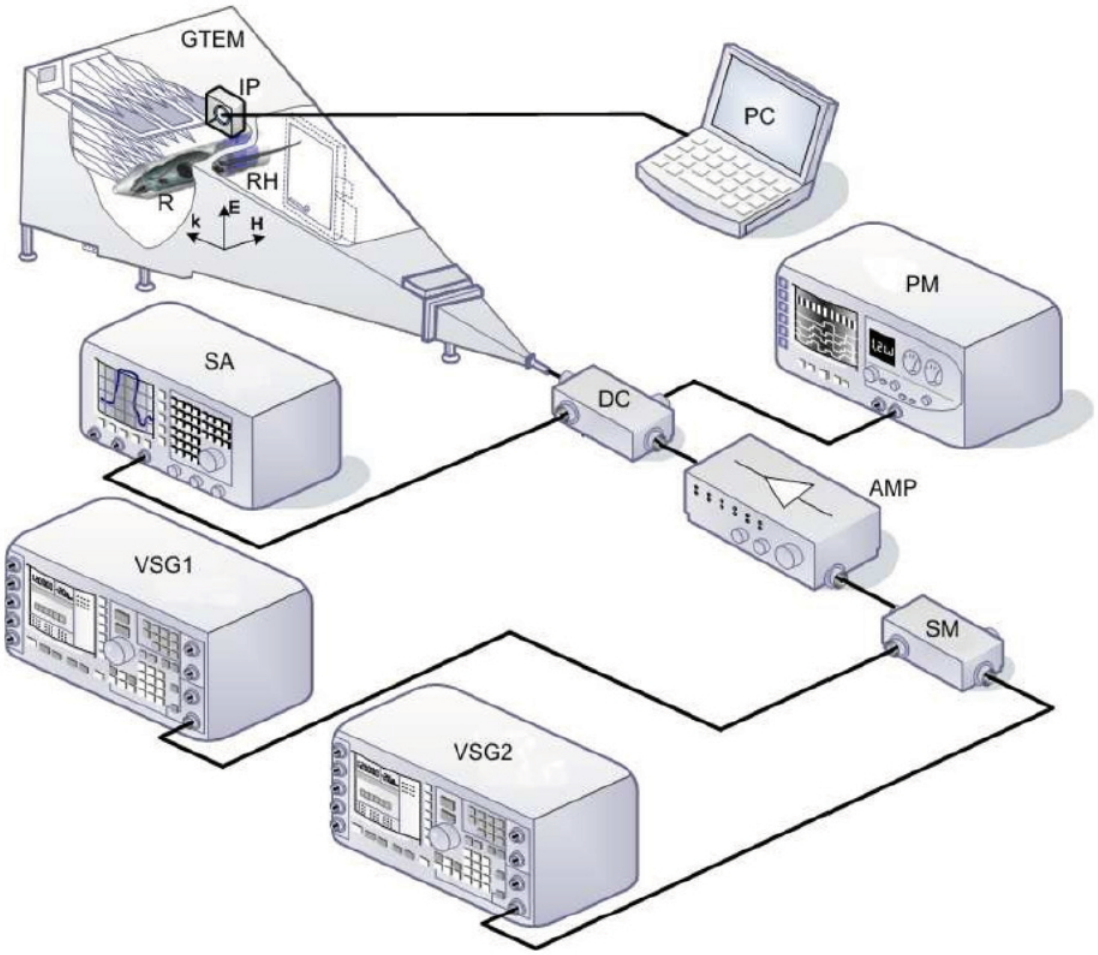

Figure 53: **Schematic of the system.** GTEM, Schaffner 250 GTEM chamber; VSG1, Agilent E8267D vector signal generator (250 KHz-20 GHz) operating at 2.45 GHz; VSG2, Agilent E4438C vector signal generator (250 KHz-4 GHz) operating at 900 MHz; AMP, research amplifier 15S1G3 (0.8−3 GHz); DC, NARDA 3282B-30 directional coupler (800 − 4000 MHz); SA, Agilent E4407B spectrum analyzer (9 KHz-26.5 GHz); PM, Agilent E4418B power meter; SM, Agilent 11636a signal mixer; RH, rat holder; IP, EF Cube isotropic probe; R, rat.

7.2 EMF radiation at 2450 MHz triggers changes in the morphology and expression of heat shock proteins and glucocorticoid receptors in rat thymus.

7.2.1 Description of the study.

Electromagnetic fields (EMFs) can act as inducers or mediators of stress response through the production of heat shock proteins (HSPs) that modulate immune response and thymus functions. In this study, we analyzed cellular stress levels in rat thymus after exposure of the rats to a 2.45 GHz radio frequency (RF) using an experimental diathermic model in a Gigahertz Transverse Electromagnetic (GTEM) chamber. So, therefore, only the VSG1 has been used.

In this experiment, we used H&E staining, the ELISA test and immunohistochemistry to examine Hsp70 and Hsp90 expression in the thymus and glucocorticoid receptors (GR) of 64 female Sprague–Dawley rats exposed individually to 2.45 GHz (at 0, 1.5, 3.0 or 12.0 W power). The 1 g averaged peak and mean SAR values in the thymus and whole body of each rat to ensure that sub-thermal levels of radiation were being reached.

The thymus tissue presented several morphological changes, including increased distribution of blood vessels along with the appearance of red blood cells and hemorrhagic reticuloepithelial cells. Levels of Hsp90 decreased in the thymus when animals were exposed to the highest power level (12 W), but only one group did not show recovery after 24 h. Hsp70 presented no significant modifications in any of the groups. The glucocorticoid receptors presented greater immunomarking on the thymic cortex in exposed animals.

Our results indicate that non-ionizing sub-thermal radiation causes changes in the endothelial permeability and vascularization of the thymus, and is a tissue-modulating agent for Hsp90 and GR.

7.2.2 Experimental Design

A total of 64 female Sprague–Dawley rats were distributed equally in the following groups:

Group A ($n = 32$): The rats were divided into 4 subgroups ($n = 8$), each of which was exposed to different levels of microwave radiation: 0 (control group), 1.5, 3.0 and 12 W for 30 min. The rats were kept alive for 90 min after radiation, then sacrificed and perfused with fixative.

Group B ($n = 32$): The rats were divided into 4 subgroups ($n = 8$), each of which was exposed to different levels of microwave radiation: 0 (control group), 1.5, 3.0 and 12 W, for 30 min. The rats were kept alive for 24 h after radiation, then sacrificed and perfused with fixative (see Fig. 54).

* The minimum timeexposure was tested previously.

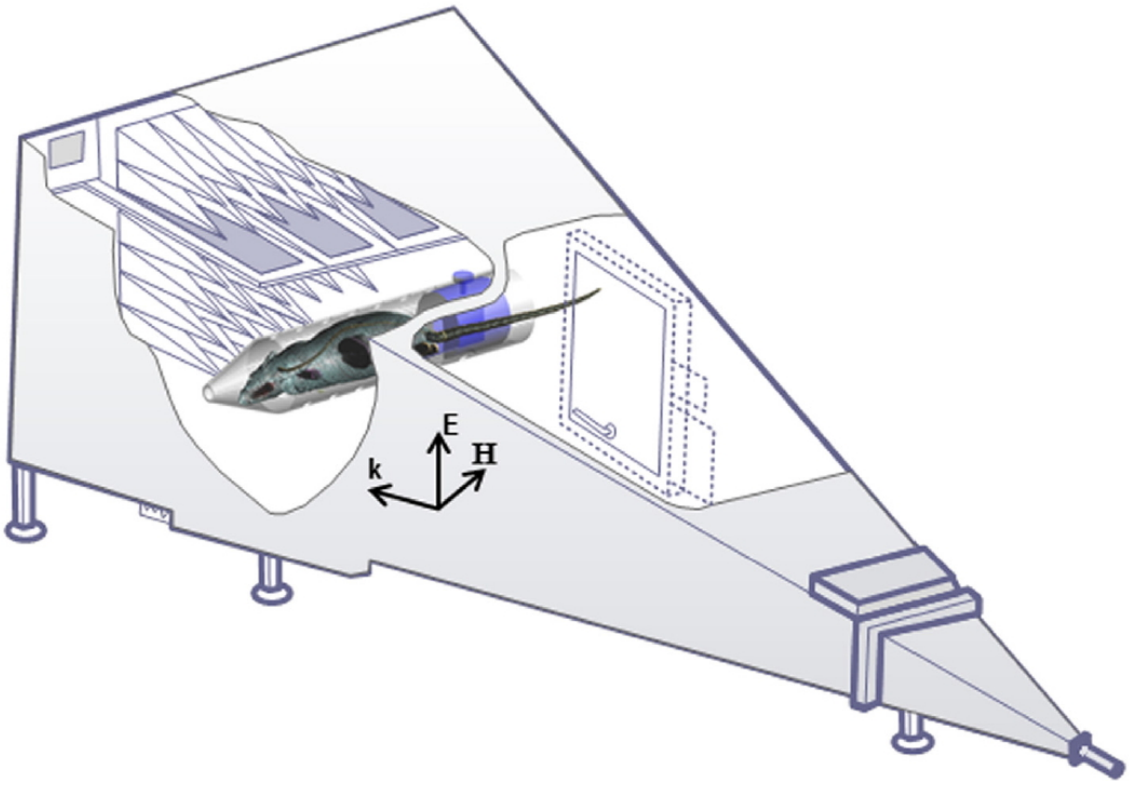

Figure 54: Representation of the position of the rat in the methacrylate holder. The left front leg is the point of maximum radiation.

7.2.3 Numerical Simulation

The specific absorption rate (SAR) values were estimated with the aid of SEM-CAD X [2] and FDTD-based software. A Sprague–Dawley numerical (voxel) phantom rat was used (model R8 [2]), weighing 198.3 g and composed of 60 different tissues assembled by slices 1.15 mm thick. Tissue morphologies were obtained bymagnetic resonance imaging. The phantom rat was radiated by a plane wave impinging on its left side, with the magnetic field H parallel to its main axis (see [2]). The field value E is specified by Eq. (67):

$$E = \sqrt{\frac{Z_0 P}{h^2 \zeta}} \tag{67}$$

where h is the septum height in the exposure zone (position of the rat), P is the input power on the GTEM cell, $Z_0 = 50\ \Omega$ is the input impedance of the cell, and ζ is a coefficient dependet on the field ripple, which was about 2 for the position of the rat.

The SAR_E values were estimated by applying a correction factor to the values obtained from the numerical simulations, in proportion to the ratio between the weight of the model rat and the weights of the experimental rats, as specified by Eq. (68):

$$SAR_E = SAR_S \times W_S/W_E \tag{68}$$

where SAR_E is the estimated value of the experimental SAR, SAR_S is the SAR obtained during the simulation, $W_S = 198.3$ $[g]$ is the weight of the model rat (see above), and W_E $[g]$ is the weight of the experimental rat.

7.2.4 Results

The mean power absorbed by the rats in the four groups (Eq. (68)) was determined, along with the average weight, mean SAR pm SEM in the brain and body, average peak SAR $\pm$ SEM for 1 g of the brain or body and 2.45 GHz frequency in a Shaffner GTEM cell. One-way ANOVA for different radiation power levels according to mean SAR in brain or body and average peak SAR for 1 g of brain or body, showed significant differences in all SAR values ($p < 0.001$), which are shown in Tables 27 and 28. Note that the increases in mean and peak SAR values are directly proportional to the input power for each subgroup.

Table 27: SAR values in thymus of experimental rats, calculated from power (P) and electric field (E). Results are expressed as Mean $\pm$ Standard Error of the Mean ($M \pm SEM$) obtained from mean SAR and average peak SAR in the animals. Values were compared by one-way ANOVA for the power applied during radiation $(0, 1.5, 3, 12W)$; followed by a Holm-Sidak test for multiple comparisons.

	FDTD-calculated specific absorption rate: experimental measurements	
	Mean SAR in thymus (W/kg)	**Peak SAR in 1g of thymus**
$P = 1.5W$ $(E = 28.48V/m)$	$0.046 \pm 1 \times 10^{-3}$	$0.041 \pm 2 \times 10^{-3}$
$P = 3.0W$ $(E = 40.28V/m)$	$0.104 \pm 5 \times 10^{-3}$	$0.076 \pm 4 \times 10^{-3}$
$P = 12.0W$ $(E = 80.56V/m)$	$0.482 \pm 12 \times 10^{-3}$	$0.340 \pm 10 \times 10^{-3}$

Table 28: SAR values in body of experimental rats, calculated from power (P) and electric field (E). Results are expressed as Mean ± Standard Error of the Mean ($M \pm SEM$) obtained from mean SAR and average peak SAR in the animals. Values were compared by one-way ANOVA for the power applied during radiation ($0, 1.5, 3, 12W$); followed by a Holm-Sidak test for multiple comparisons.

	FDTD-calculated specific absortion rate: experimental measurements	
	Mean SAR in body (W/kg)	**Peak SAR in 1g of body**
$P = 1.5W$ $(E = 28.48V/m)$	$0.0169 \pm 7 \times 10^{-4}$	$0.089 \pm 9 \times 10^{-3}$
$P = 3.0W$ $(E = 40.28V/m)$	$0.0364 \pm 19 \times 10^{-3}$	$0.180 \pm 9 \times 10^{-3}$
$P = 12.0W$ $(E = 80.56V/m)$	$0.161 \pm 4 \times 10^{-3}$	$0.795 \pm 2 \times 10^{-3}$

7.3 Evidence of cellular stress and casapse-3 resulting from a combined two-frequency signal in the cerebrum and cerebellum of Sprague-Dawley rats.

7.3.1 Description of the study.

Multiple simultaneous exposures to electromagnetic signals induced adjustments in mammal nervous systems. In this study, we investigated the non-thermal SAR (Specific Absorption Rate) in the cerebral or cerebellar hemispheres of rats exposed in vivo to combined electromagnetic field (EMF) signals at 900 and 2450 MHz.

Forty rats divided into four groups of 10 were individually exposed or not exposed to radiation in a GTEM chamber for one or two hours. After radiation, we used the Chemiluminescent Enzyme-Linked Immunosorbent Assay (ChELISA) technique to measure cellular stress levels, indicated by the presence of heat shock proteins (HSP) 90 and 70, as well as caspase-3-dependent pre-apoptotic activity in left and right cerebral and cerebellar hemispheres of Sprague Dawley rats.

Twenty-four hours after exposure to combined or single radiation, significant differences were evident in HSP 90 and 70 but not in caspase 3 levels between the hemispheres of the cerebral cortex at high SAR levels. In the cerebellar hemispheres, groups exposed to a single radiofrequency (RF) and high SAR showed significant differences in HSP 90, 70 and caspase-3 levels compared to control animals. The absorbed energy and/or biological effects of combined signals were not additive, suggesting that multiple signals act

on nervous tissue by a different mechanism.

7.3.2 Experimental Design

A total of 40 rats, divided into four groups of 10, were used in the study. The animals in three groups were individually exposed to radiation in the GTEM chamber:

Group I: Irradiation at $900MHz$ (power = $2W$ or $4W$).

Group II: Irradiation at $2450MHz$ (power = $2W$ or $4W$).

Group III: Simultaneous irradiation at $900MHz$ (power = $1W$ or $2W$) and $2450MHz$ (power = $1W$ or $2W$).

Group IV: The negative control group of 10 rats that were individually not irradiated (negative controls).

Two temporally separate experiments were done (all animal tissues were radiated and processed at different times) as follows:

Experiment 1: The three experimental groups (I-III) were exposed in the GTEM chamber for one hour at maximum power of $2W$.

Experiment 2: The three experimental groups (I-III) were exposed in the GTEM chamber for two hours at maximum power of $4W$.

All rats in all groups were immobilized in the holder for 1 or 2 hours, during which time the rats in Groups I-III were individually irradiated. Immobilized Group IV animals were placed in the GTEM chamber but were not irradiated. Rats in Groups I-IV were slaughtered 24 h after removal from the GTEM chamber.

7.4 Numerical simulations

The specific absorption rate (SAR) values were estimated with the aid of SEM-CAD X finite-difference time-domain (FDTD)-based software [2]. A Sprague-Dawley numerical (voxel) phantom rat was used [2], weighing 198.3 g and composed of 60 different tissues assembled into slices 1.15 mm thick. Tissue morphologies were obtained by magnetic resonance imaging. The phantom rat was radiated by a plane wave impinging on its left side, with the magnetic field H parallel to its main axis [2].

The electric field value in the simulation was measured experimentally for each case, using an isotropic probe located in the center of the area where the rat would be exposed.

The value of SAR_E in each case was estimated by scaling the SEMCAD [2] numerical model rat, taking into account the weight differences among the rats in the three experimental groups of radiated animals. In this way, we have made a uniform scaling (multiplying all the original dimensions of the numerical phantom rat with the same factor), according to the proportionality constant needed to effectively scale the model rat to the model weight [4].

7.5 Results

Each of the pure sinusoidal signals used in Group I (900 MHz) and II (2450 MHz), and the sum of both signals ($900 + 2450$ MHz) can be seen in Fig. 55A, which illustrates the simulations using MATLAB scientific software. The combination of signals obtained in the simulation was also validated at lower frequencies in the laboratory using the Agilent Infinium (600 MHz) oscilloscope to visualize the output signal that results from the sum of the two sinusoidal signals.

Tables 29 and 30 show how the SAR_E values in radiated rat groups I to III in the cerebrum, cerebellum and body correspond to the mean SAR value for each tissue type. Fig. 55B and 55C show the mean SAR distribution in vertical sections of the scaled numerical phantom rat when radiated with 900 MHz (power = $1W$ or $2W$) and 2450 MHz (power = $1W$ or $2W$) simultaneously.

Since the animals were exposed laterally in the GTEM chamber, the left side of the body (as seen from the door of the chamber) experienced a greater field than the right side. This is due to the fact that the electric field within the GTEM increases as the height of the septum decreases. For this reason, and to verify the data obtained in the biological study described here, we simulated the exposure of the numerical model rat (198.3 g) at different field levels on both sides, which were experimentally determined in the chamber with an isotropic probe in the position occupied by the two sides of the animal cerebrum. Once recorded and introduced into the simulation, a zone study was done for both sides of the cerebrum using the SEMCAD FDTD simulation program. Tables 31 and 32 show the results of this comparison, showing that the SAR on the left side of the cerebrum and cerebellum was always higher than on the right side.

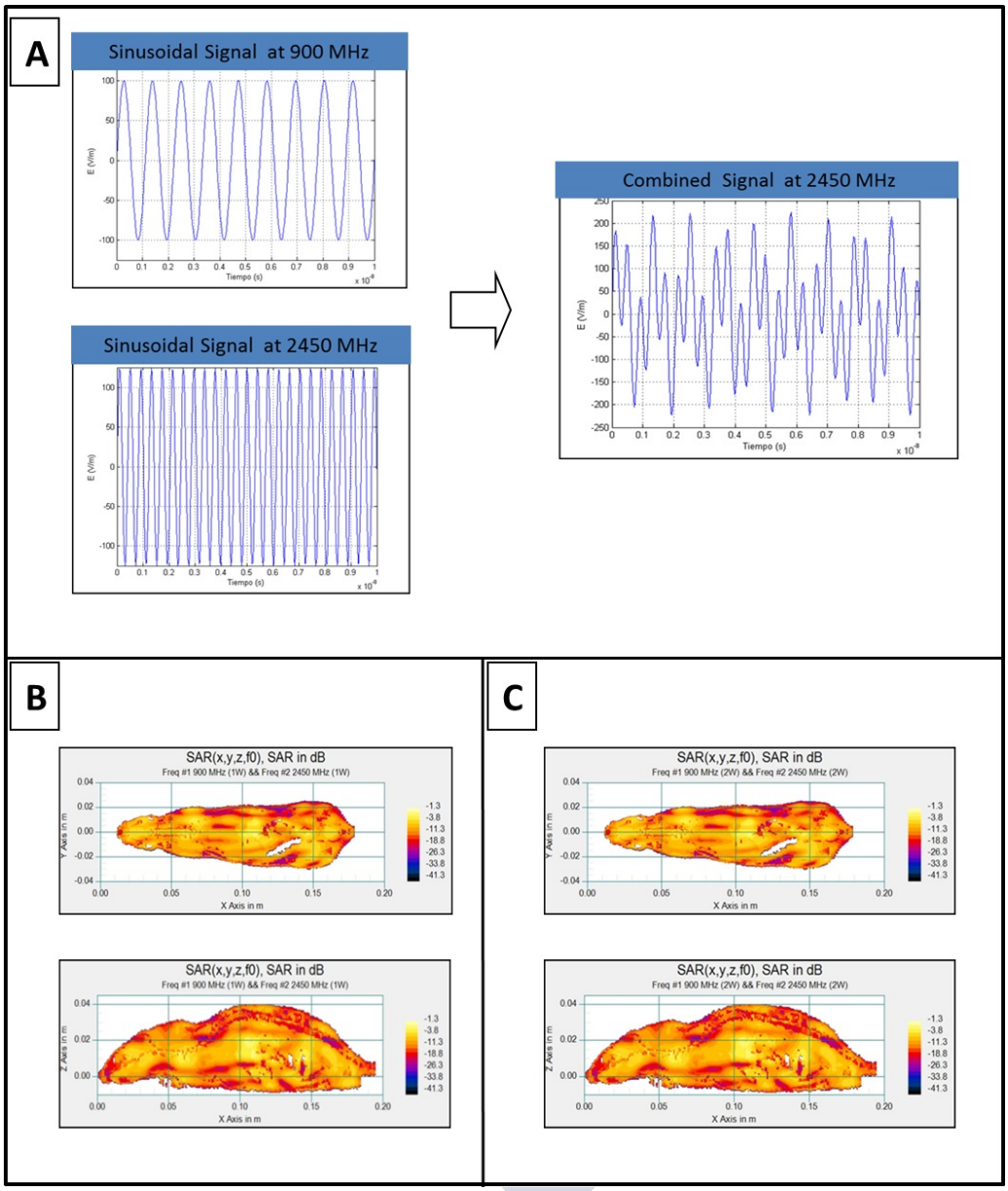

Figure 55: A. Representation of each of the pure sinusoidal signals used in Group I (900 MHz) and II (2450 MHz) and the sum of both signals (900+2450 MHz). B. Distribution of Mean SAR in vertical sections of the scaled numerical phantom rat when radiated simultaneously with 900 MHz ($P_{TR} = 1W$) and 2450 MHz ($P_{TR} = 1W$) for cases of minimum and maximum mass of the group. SAR is expressed relative to absorption of the entire local power density in the absence of the rat. C. Distribution of Mean SAR in vertical sections of the scaled numerical phantom rat when radiated simultaneously with 900 MHz ($P_TR = 2W$) and 2450 MHz ($P_TR = 2W$) for cases of minimum and maximum mass of the group. SAR is expressed relative to absorption of the entire local power density in the absence of the rat.

Table 29: SAR values in cerebrum, cerebellum and body of experimental rats, calculated from transmitted power ($P_{TR} = 2W$), electric field (E_m) and incident power density (P_D).

		FDTD-calculated specific absorption rate: experimental measurements		
	Weight(g)	Mean SAR of body (W/kg)	Mean SAR of cerebrum (W/kg)	Mean SAR of cerebellum (W/kg)
$f = 900MHz$				
$P_{TR} = 2W$	185.9	0.0541	0.0583	0.0212
$E_m = 48V/m$	198.4	0.0510	0.0513	0.0320
$P_D = 6.11W/m^2$				
$f = 2450MHz$				
$P_{TR} = 2W$	175.7	0.0723	0.2731	0.1590
$E_m = 50V/m$	193.9	0.0682	0.2344	0.1094
$P_D = 6.63W/m^2$				
$f = 900 + 2450MHz$				
$P_{TR} = 1 + 1W$	158.7	0.0478	0.0212	0.0678
$E_m = 39V/m$	201.7	0.0367	0.0183	0.0422
$P_D = 4.03W/m^2$				

Table 30: SAR values in cerebrum, cerebellum and body of experimental rats, calculated from transmitted power ($P_{TR} = 4W$), electric field (E_m) and incident power density (P_D).

		FDTD-calculated specific absorption rate: experimental measurements		
	Weight(g)	Mean SAR of body (W/kg)	Mean SAR of cerebrum (W/kg)	Mean SAR of cerebellum (W/kg)
$f = 900MHz$				
$P_{TR} = 4W$	191.9	0.0870	0.0732	0.0452
$E_m = 62V/m$	219.6	0.0829	0.0934	0.0822
$P_D = 10.20W/m^2$				
$f = 2450MHz$				
$P_{TR} = 4W$	186.7	0.0919	0.3274	0.1765
$E_m = 57V/m$	207.3	0.0838	0.2572	0.1224
$P_D = 8.62W/m^2$				
$f = 900 + 2450MHz$				
$P_{TR} = 2 + 2W$	192.0	0.0705	0.1590	0.0856
$E_m = 53V/m$	210.0	0.0776	0.1622	0.0894
$P_D = 4.03W/m^2$				

Table 31: SAR values in cerebrum and cerebellum and body of a Sprague-Dawley numerical phantom rat, calculated from transmitted power ($P_{TR} = 2W$), electric field (E_m) on both sides of the cerebrum (left and right).

	Side	E_m (V/m)	Mean SAR of cerebrum (W/kg)	Mean SAR of cerebellum (W/kg)
$f = 900MHz$	Left	50.63	0.0556	0.0411
$P_{TR} = 2W$	Right	50.06	0.0403	0.0251
$f = 2450MHz$	Left	53.32	0.0492	0.0907
$P_{TR} = 2W$	Right	41.30	0.0260	0.0859
$f = 900 + 2450MHz$	Left	43.27	0.0336	0.0567
$P_{TR} = 1 + 1W$	Right	39.60	0.0267	0.0358

Table 32: SAR values in cerebrum and cerebellum and body of a Sprague-Dawley numerical phantom rat, calculated from transmitted power ($P_{TR} = 4W$), electric field (E_m) on both sides of the cerebrum (left and right).

	Side	E_m (V/m)	Mean SAR of cerebrum (W/kg)	Mean SAR of cerebellum (W/kg)
$f = 900MHz$	Left	71.42	0.1119	0.0818
$P_{TR} = 4W$	Right	70.99	0.0802	0.0504
$f = 2450MHz$	Left	74.67	0.0965	0.1832
$P_{TR} = 4W$	Right	58.69	0.0596	0.1666
$f = 900 + 2450MHz$	Left	57.42	0.0628	0.1086
$P_{TR} = 2 + 2W$	Right	55.58	0.0495	0.0647

References

[1] A. López-Furelos, MdM. Miñana-Maiques, J. M. Leiro-Vidal, J. A. Rodríguez-Gonzalez, F. J. Ares-Pena, M. E. López-Martin, 'An Experimental Multi-frequency System for Studying Dosimetry and Acute Effects on Cell and Nuclear Morphology in Rat Tissues,' *PIER*, vol. 129, pp. 541-558, 2012.

[2] Schmid & Partner Engineering AG, Reference manual for the SEMCAD simulation plat-form for electromagnetic compatibility, antenna design and dosimetry," 2009, www.semcad.com

[3] Schaffner Electrotest Gmbh, GTEM Test Cells, Datasheet 2005.

[4] F. Schönborn, K. Pokovic, N. Kuster, 'Dosimetric Analysis of the Carousel Setup for the Exposure of Rats at 1.62 GHz,' *Bioelectromagnetics*, vol. 25, pp. 16-26, 2004.

8 Conclusions

- As it was described in chapter 2, radiation patterns with envelopes closely approximating those of circular Taylor patterns within a cone around the main beam can be achieved by uniformly excited concentric ring arrays with nonuniform ring spacing constrained to exceed 0.5λ so as to minimize mutual coupling. The directivities of these patterns are little less than those of the original Taylor patterns. The use of elements with $\cos^2(h\theta)$ power patterns, where h is a scaling factor, allows the main beam to be scanned 20° with minimal loss of directivity. Computational efficiency is improved, at the expense of controlled cone width, by building the antenna from annular subarrays, in each of which the between-ring spacing is uniform. Although in practical applications non-negligible mutual coupling may not be totally prevented by the 0.5λ ring spacing constraint, at least for wide scan angles, these arrays will be of interest to the multibeam satellite antenna community.

- Following appropriate adaptation as described in section 3, the classical density tapering method can be applied to multi-ring planar arrays without previously fixing either the number of radiating elements or the positions or number of the constituent rings. Both pencil beams and shaped beams can be obtained.
  Since this method depends on the choice of a suitable starting density $I(r)$, an understanding of the behaviour of the classical families (Taylor, Hansen, two-parameter, Gaussian, etc.), though not essential, is of some value in its application. It is seen above that its judicious use can afford results that approach those of methods involving stochastic optimization and custom-designed element factors. Furthermore, it can rapidly provide good starting points for stochastic optimization, thus allowing the solution of problems, the solution of which by direct optimization approaches, if at all possible, is much more lengthy. The complete solution of the ESA tender problem described in section 3.4 is a case in point. As far as we know, this solution represent the first approach for obtaining the directivity value

- In section 4, a planar array of parasitic elements fed by a single active element affords satisfactory performance. This array is more compact and robust than that previous prototypes developed by the Radiating Systems Group. The measurements performed on the constructed model show tolerable discrepancies with the simulated results. These differences are attributable to inaccuracy in the construction process, interactions of the materials used, and soldering imperfections, as well as to the assumption of an infinite ground plane in the calculations.

- In section 5, a novel technique for the measurement and characterization of PM pollution has been explored. This technique involves a linear array of shunt slots in the broad wall of an air-filled rectangular waveguide optimized to afford more sensitivity under variations of the dielectric constant of the immersed medium. In that way, the system will present a narrow beamwidth and, therefore, a much easier mismatch under tiny changes in its effective operational frequency. Assuming that

our device has a maximum error in the measurement of the reflection coefficient of about 10%, we have estimated from the values of the optimized curves an accuracy of 10^{-3} in ϵ_r values. Attending to the simulated results reported here, the idea of a microwave antenna for monitoring the air pollution level seems promising. It is necessary to note that, in each case, it is mandatory to obtain the value of the humidity level present in the atmosphere for calculating the pollution concentration. For that reason, a numerical study of the influence of atmospheric relative humidity on the resonant frequencies of a series of Yagi–Uda antennas, the constituent dipoles of which were coated with hydrophilic polyimide were carried out. It was found that the effect of changes in relative humidity was considerably greater than cases found in the previous literature: the resonant frequencies of our antennas fell by between 28 and 37 MHz as the relative humidity rose from 20% to 90% at 30°C. Although many details remain to be evaluated, such as the stability of the polyimide coatings and the influence of temperature, we conclude that, in principle, antennas of the type investigated in this work constitute a feasible alternative to existing methods of measuring relative humidity.
As a result, a measurement system these two devices in parallel seems the optimal solution for determining the level of particulate matter pollution. In addition, the antenna design objectives must include ensuring that the antenna is easily cleaned, because the degree to which the measurements made by an antenna may be influenced by the deposition of particles.

- In section 6 a simple and cheap procedure for implementing the measure of the EM exposure level was presented, for the benefit of citizens in the city environment. The method is based on the measurement of the field level over a limited number of points in the city, and on the intelligent use of a numerical novel solver that allows interpolation of EMFI all over the city. All citizens can request information about their EMFI exposure via internet, or connection with an appropriate Calling Centre. Consistency of the method has been first verified by numerical simulations, and then its accuracy has been evaluated by using a measurement campaign. It has turned out that rms differences between measured and estimated EMFI are of the order of few dB.

- In section 7 two studies involving different SAR calculation methods were described. In the first, the SAR was estimated by appliying a correction factor to the values obtained from the numerical simualtions, in proportion to the ratios between the weight of the rat model and the weights of the experimental rats. In the second, the SAR was estaimated by scaling the numerical model of the rat, taking into account the weight differences among the rats in the experimental groups.

9 Resumen de la Tesis

La presente tesis puede resumirse en términos generales de la siguiente manera:

En una primera parte se han realizado estudios sobre la síntesis de diagramas de radiación producido por agrupaciones o en adelante agrupaciones de antenas planas. Más concretamente se ha puesto el énfasis en antenas planas de tipo circular. Con ello se pretende alcanzar un control preciso del lóbulo principal de radiación y un aumento de la eficiencia, entre otras características. Además de esto, el estudio de agrupaciones se ha visto complementado con estudios de diseño y, en un caso concreto, construcción y medida de prototipos de antena. Dichos prototipos están enfocados para ser actores dentro del entorno urbano con el ánimo de ofrecer servicios a la ciudadanía. En clara relación a este bloque, el segundo de ellos presenta un trabajo sobre el testeo de un método de monitorización del campo electromagnético dentro una zona concreta de una ciudad cristalizado en un software de predicción de campo tras la introducción en el mismo de las fuentes de radiación existentes. Así mismo, en el último bloque temático, se plantean dos estudios numéricos asociados con la interacción de los campos electromagnéticos con los seres vivos y, más concretamente, con animales pequeños.

A continuación se realizará una descripción más pormenorizada de cada uno de los capítulos que la conforman la tesis doctoral.

9.1 Introducción

9.1.1 Agrupaciones de antenas

En la actualidad, las agrupaciones de antenas formados por elementos radiantes idénticos son utilizados tanto para aplicaciones radar como para aplicaciones satelitales. Estos sistemas radiantes conforman una solución con una gran cantidad de ventajas frente a la alternativa de utilizar un único elemento.

9.1.2 Monitorización de campo electromagnético en el entorno urbano

Un concepto que se está popularizando de manera importante, en particular en Europa, es el de las ciudades inteligentes, esto es, zonas urbanas en las cuales los ciudadanos disfrutan de una serie de beneficios: entorno más seguro, reducción de la contaminación, servicios de transporte más eficientes, reducción general del consumo energético, y muchos más. Para llegar a alcanzar esto, las autoridades competentes deben de dictar una serie de leyes apropiadas y deben de implementar una serie de herramientas apropiadas.

Un problema relevante entre todos los relacionados con una mejora de la calidad de vida de la ciudadanía podría ser el establecimiento de un método de evaluación simple y barato de la intensidad de campo electromagnético, dirigido a controlar el nivel de

exposición en el entorno urbano que sufre el ciudadano medio.

Este método podría pasar por el establecimiento de un conjunto limitado de sensores electromagnéticos ocultos que se posicionarían por todo el área bajo protección. Los valores detallados de campo electromagnético en cada punto de la ciudad se evaluarían mediante un riguroso algoritmo de interpolación, basado en la integración de dichos sensores y un software para la predicción del campo.

9.1.3 Cálculos dosimétricos de SAR en animales pequeños

En los últimos años, el uso de las tecnologías de comunicación *wireless* se han diseminado ampliamente en nuestro entorno. El uso de teléfonos móviles, las comunicaciones *Bluetooth*, *Wifi*, 4G, etc. suponen tecnologías con las que nosotros coexistimos y que están viendo incrementado su uso y son actores diarios en nuestra vida. Este hecho provoca que el estudio de los efectos de la radiación electromagnética en el día a día sea de gran interés. Además de ello, la población está actualmente preocupada sobre el posible daño que los campos de radiofrecuencia a los que está expuesta pueden provocarle.

9.2 Problema de síntesis de diagramas tipo Taylor con antenas planas isofóricas multiaro.

En el contexto de continua demanda de antenas de alta resolución, las ligaduras económicas actuales han potenciado el interés en agrupaciones de elementos radiantes con excitaciones que son iguales o que solamente difieren en su fase. Estas agrupaciones necesitarán redes de alimentación lo suficientemente simples y explotar en su totalidad la capacidad de potencia de todos sus elementos radiantes. Una geometría que ha atraído siempre la atención a este respecto son las agrupaciones de aros concéntricos.

La aparición de lóbulos laterales altos para valores angulares altos es característica de los patrones de radiación creados por agrupaciones no uniformemente espaciadas. Para las agrupaciones lineales, se sabe que el patrón creado por una agrupación con taper espacial simétrico con $2N$ elementos es una buena aproximación de su correspondiente agrupación con taper en amplitud hasta su lóbulo N-ésimo, y los resultados para agrupaciones de $2N$ aros también sugieren un buen comportamiento fuera del lóbulo lateral N-ésimo. En este trabajo se concluye que se puede imponer un control riguroso para ángulos de pequeños a medianos desde el lóbulo principal mediante la optimización de los radios de los aros para que los picos de los lóbulos laterales se encuentren lo suficientemente cerca de una función envolvente ajustada a los picos de los lóbulos laterales de la función objetivo.

Con el fin de sintetizar diagramas de radiación de tipo Taylor, en el segundo capítulo se han utilizado antenas circulares con elementos uniformemente excitados (esto es, isofóricos). El proceso de optimización involucrado ha tenido como objetivo aproximar

lo suficiente el diagrama bajo diseño a la curva envolvente del diagrama tipo Taylor utilizado como objetivo.

Además de ello, también se ha discutido un método en el cual se han utilizado subagrupaciones anulares como alternativa para obtener mejores resultados en términos de tiempo de cálculo. En esta reformulación del problema, se verán limitados el número de espaciados entre anillos, puesto que cada subagrupación de anillos contará con un espaciado fijo. Aunque en aplicaciones prácticas el acoplo mutuo no se puede evitar completamente con las condiciones de espaciado mínimo de 0.5λ entre anillos, al menos para ángulos de escaneo grandes, estas agrupaciones serán de interés para la comunidad de antenas de satélite multihaz. Dichas aplicaciones más concretamente se encuentran encuadradas en satélites multihaz de banda Ka.

9.3 Síntesis paramétrica de haces suma y haces perfilados de tipo flat-topped

En este tercer capítulo se abundará en el estudio de agrupaciones de antenas con aros concéntricos e isofóricos mediante la implementación de un método de cálculo de configuraciones de agrupaciones tanto de diagramas tipo suma como tipo shaped. Además de ello la utilización de este algoritmo ha dado lugar a un buen punto de partida para la resolución de un problema de síntesis relacionado con la cobertura multihaz de la Tierra mediante métodos de optimización. En este último caso, la utilización de sus resultados como punto de partido de una optimización estocástica ha dado pie a la solución de un problema de síntesis de alto nivel como puede ser el problema de multihaz mencionado.

El interés en agrupaciones de antenas uniformemente iluminadas (isofóricos) con taper espacial ha revivido recientemente. Para agrupaciones consistentes en elementos dispuestos en aros concéntricos presentamos un algoritmo no estocástico que calcula los radios de los aros para generar diagramas suma con la necesidad de especificar el número de anillos. Si se permite la variación de fases para los elementos, el algoritmo también será capaz de sintetizar agrupaciones con taper espacial que generarán huellas de haces perfilados axialmente simétricos (para los cuales se puede llevar a cabo modificaciones, mediante métodos ya conocidos en la literatura de antenas, de sus formas con el fin de dar respuesta a diferentes formas más allá de la huella circular).

9.4 Prototipado de antena plana.

Seguidamente, en el capítulo cuarto, se relata el diseño, optimización, construcción y medida de una antena basada en el uso de un dipolo activo posicionado sobre un plano de tierra y una agrupación de dipolos pasivos. La presencia de los dipolos parásitos se traduce en un aumento del tamaño eléctrico efectivo de la antena y en una significativa mejora de su directividad en comparación con el caso de un único dipolo frente a un plano de tierra. Además de ello, la utilización de un único elemento activo da lugar a una red

de alimentación tremendamente simple que reduce la complejidad de la antena a la hora de su construcción. Como aplicación de esta filosofía a la hora de diseñar, se presenta una agrupación plana de 48 dipolos parásitos que descansan sobre un material dieléctrico cuyo límite inferior viene dado por un plano conductor que actúa de plano de tierra, alimentado mediante un único dipolo activo cuya frecuencia de funcionamiento es 5 GHz. Como resultado de esto se obtiene un diagrama de tipo suma con ganancia y ancho de banda moderadamente elevadas. Las simulaciones han sido refrendadas mediante medidas experimentales realizadas en la cámara anecoica del Grupo de Sistemas Radiantes. Una vez refrendados los cálculos numéricos se realiza un estudio para evaluar la inclusión de un radomo protector que prevenga a la antena ante posibles agentes externos (inclemencias meteorológicas, golpes, etc.). La directividad obtenida finalmente ha sido 25.30 dB, su ganancia asciende a 14.78 dB, el nivel de lóbulos laterales corresponde con -6.15 dB, y cuenta con un ancho de banda en parámetros S a -10 dB de 12.7% y de ganancia ($< 3dB$) de 3.1%.

9.5 Estudios de viabilidad de soluciones basadas en antenas para la monitorización de parámetros ambientales.

El incremento de la concienciación acerca de la importancia de la calidad ambiental, en parte relacionada con el cambio climático, ha creado una necesidad de ofrecer una medida de múltiples variables ambientales lo suficientemente precisa y flexible. Esto se ejemplifica con la inclusión del desarrollo de nuevos sistemas de observación in situ para la sección de Acción climática, medio ambiente, eficiencia de los recursos y materias primas del programa Horizonte 2020 de la Unión Europea.

En la actualidad, un 54% de la población mundial vive en zonas urbanas, una proporción que se espera que aumente a un 66% en 2050. El material particulado (PM) (o aerosoles) es una de los polutantes más importantes que afectan a la calidad del aire tanto en entornos como urbanos o incluso rurales del mundo. La polución atmosférica supone un serio problema de salud. Los sistemas respiratorios de los niños y de las personas de tercera edad se ven particularmente afectados; para los más vulnerables, la polución atmosférica puede ser fatal. Los polutantes atmosféricos pueden causar síntomas alérgicos, pero cuando se ven asociados con granos de polen, su potencia alergénica se ve incrementada. Otros efectos ambientales incluyen la reducción de la capa de ozono (que a su vez favorece el cáncer de piel), y el daño de la estructura de edificios y monumentos. Las fuentes de la polución atmosférica incluye tanto las fuentes naturales (polvo suspendido en el viento, sal de los océanos y erupciones volcánicas) y antropogénicas (aerosoles producidos por la quema de biomasa, la combustión de automóviles y la emisión de plantas de energía) también juegan un papel importante en los procesos climáticos. Los componentes principales de la polución atmosférica son (dependiendo de la fuente) monóxido de carbono, dióxido de carbono, clorofluorocarbonos (CFCs), metales pesados (principalmente plomo), ozono, óxidos de mononitrógeno (NOx), dióxido de sulfuro, compuestos orgánicos volátiles (VOCs) y otros polutantes ambientales peli-

grosos (HAPs, generalmente asociados con actividades industriales específicas), y material particulado en el aire (PM). Cada uno de estos componentes constituye un daño a la salud.

Aunque las emisiones de polutantes aéreos han venido decreciendo de manera general en los últimos veinte años, en gran parte de los estados miembros de la Unión Europea (EU) continúan excediendo los límites que han sido establecidos internacionalmente para la protección de la salud humana y el entorno, y estudios epidemiológicos llevados a cabo en diferentes ciudades durante la última década han confirmado que la polución ambiental continúa afectando a la salud tanto de niños como de adultos.

La polución atmosférica particulada altera la constante dieléctrica de la atmósfera en sus inmediaciones. En principio, esto podría permitir que el nivel de polución sea determinado mediante la medición de sus efectos en el comportamiento de una antena. En este capítulo, se presenta una técnica novedosa para medir estos efectos. Esta técnica se basa en la utilización de una guía de ondas rellena de aire y formada por una agrupación lineal de ranuras. Además, se incluye el diseño de un prototipo de medidor de nivel de humedad relativa para asegurar un nivel de precisión aceptable de la técnica de medición. Recubriendo una antena con una capa de poliimida hidrofílica se demuestra como los efectos de la humedad relativa en las características de la antena se ven reforzados. Es por ello que en esta segunda parte del capítulo se ha diseñado una antena tipo Yagi-Uda con dipolos recubiertos de poliimida y se ha llevado a cabo un estudio simulado investigando la influencia de la humedad relativa en su frecuencia de resonancia. Se concluye que antenas de este tipo constituirían sensores viables para la medida de la humedad relativa atmosférica, e hipotetizar que en ciertas situaciones estos sensores pueden presentar una ventaja frente a otras alternativas existentes.

9.6 Monitorización del campo electromagnético es un escenario urbano.

En esta sección se ha examinado un problema relevante relacionado con la mejora de la calidad de vida de la ciudadanía: evaluación mediante un sistema de medida simple y barato de la intensidad de campo electromagnético, dirigida a controlar el nivel de exposición de los ciudadanos en el entorno urbano. En el medio, el campo electromagnético se ve generalmente identificado como polución ("nube tóxica" electromagnética) lo que no es apropiado en absoluto: puede ponerse de manifiesto claramente que si esta "nube tóxica" fuera eliminada, la señal transmitida sería eliminada también y la transmisión de información mediante redes sin hilos desaparecería. La manera adecuada de enfrentar este problema consiste en monitorizar la intensidad de campo electromagnético a lo largo de toda la ciudad y comprobar que su nivel no excede en modo alguno los límites de exposición marcados por la legislación.

Sin embargo, esta medida anteriormente mencionada no supone una solución ante el problema. De hecho, las campañas de toma de datos periódicas generan de manera

general (debido en gran medida a su mala documentación) una preocupación, miedo y fiebre irracional entre la población de cara al problema de la "nube tóxica" de polución electromagnética. En este sentido cabe hacer citar a la *Organización Mundial de la Salud*: *La Salud es un estado de bienestar físico, mental y social, y no una mera ausencia de dolencia o enfermedad*. Caminando hacia este ideal, se debe implementar un sistema de información directa a cada uno de los ciudadanos que lo deseen, donde se les dé cuenta del nivel de intensidad de campo electromagnético al que están expuestos. Este debería de ser un sistema al que él/ella pudiera estar permanentemente u ocasionalmente conectado.

Se puede concluir que la intensidad de campo electromagnético debe de ser entonces continuamente monitorizado, tanto en espacio como en tiempo, y sus niveles deben de ser accesibles a cualquier ciudadano que desee conocerlos.

La evaluación de diferentes polutantes (reales) en las ciudades ya ha sido ampliamente implementada mediante la medición del contenido particulado de muchas substancia presentes en la atmósfera. Sin embargo, se han experimentado muy pocos intentos en la dirección de desarrollar un sistema de medida sistemático y continuo para la intensidad de campo electromagnético o de implementar un mapa de intensidad de campo electromagnético en zona urbana. Algunos intentos en este sentido pueden ser mapas de cobertura de campo electromagnético ofrecidos por ciertas aplicaciones web: estas obtienen sus niveles mediante la recolección de datos de la intensidad de la señal recibida por teléfonos móviles de los propios usuarios de la red móvil. Sin embargo, la precisión de estos datos es desconocida, y a menudo no es facilitado un valor numérico de la intensidad sino que se da una idea cualitativa de la misma (alta, baja, etc.). Intentos más serios en este sentido serían estudios llevados a cabo en Zurich, donde se ha establecido un mapeado del campo electromagnético gracias al posicionamiento de sensores en los vehículos de transporte público de la ciudad. Sin embargo en cuanto a la resolución obtenida, nos estaríamos moviendo entorno a unos 100m y evidentemente, solamente ofrece datos de las zonas en donde las rutas de transporte intervienen. Por lo tanto, este último ejemplo, a pesar de ser lo suficientemente relevante, tendría problemas con su resolución.

Por consiguiente, atendiendo a todo lo anteriormente descrito, en este capítulo sexto de la tesis se ha descrito un método simple y económico de monitorización de la intensidad de campo electromagnético en áreas urbanas. Este método está basado en la medición del nivel de campo en puntos discretos de la ciudad y su transmisión a un centro de control operativo, donde los valores de campo en la totalidad de la misma se determinan mediante interpolación en tiempo real. Los ciudadanos tendrían así, por tanto, la oportunidad de obtener los niveles de campo a los que se encuentran en su zona de residencia, vía Internet, o conectándose con una centralita diseñada para atender a estas peticiones. A lo largo de este capítulo sexto de la tesis se presentan estudios numéricos de la intensidad de campo electromagnético en la ciudad implementados mediante este método novedoso y estudios

experimentales para contrastar estos valores obtenidos.

9.7 Simulación del problema de Tasa de Absorción Específica en ratas.

La cantidad física básica de energía electromagnética que determina los efectos biológicos es el campo electromagnético inducido en el organismo expuesto a la radiación incidente. La dosimetría por lo tanto se puede definir como la determinación de la energía absorbida por un cuerpo expuesto a campos eléctricos y magnéticos provocados por una señal de radiofrecuencia.

La absorción de energía electromagnética en organismos vivos depende fundamentalmente de:

- Parámetros del campo incidente (frecuencia, polarización, etc.).
- Características del elemento bajo exposición como la geometría interna y externa o las propiedades dieléctricas de los tejidos (conductividad y permitividad).
- Efectos de tierra, reflexión o refracción y de otros objetos que puedan interactuar entre la fuente y el objeto. La energía incidente es reflejada a nivel de las diversas interfases tisulares. El coeficiente de reflexión, que viene dado por la relación entre la intensidad incidente y la reflejada, es muy elevado en la interfase aire-piel, lo que indica que gran parte de la energía incidente es reflejada sin llegar a penetrar en el tejido.

Para determinar la interacción de la radiofrecuencia con los tejidos resulta imprescindible describir los siguientes parámetros físicos:

- La densidad de corriente inducida en los tejidos (J).
- La intensidad de campo eléctrico interno (E).
- El SAR.

La magnitud básica que se emplea para dosimetría de radiofrecuencia-microonda es la Tasa de Absorción Específica (TAE ó SAR acrónimo en inglés Specific Absortion Rate), que ha sido definida como la cantidad de potencia electromagnética absorbida por un tejido por unidad de masa. Su unidad de medida es el watio por kilogramo (W/Kg).

En este capítulo séptimo se presentarán dos estudios de simulación para determinar la tasa de absorción específica (SAR) en ratas. Estas simulaciones están enfocadas a cubrir las necesidades que presentan estudios de efectos biológicos donde se busca correlacionar la incidencia de los campos electromagnéticos con la actividad de diferentes proteínas.

USC
UNIVERSIDADE
DE SANTIAGO
DE COMPOSTELA

A Author's publications

A.1 Journal Papers

1. **Aarón Ángel Salas-Sánchez**, Juan Antonio Rodríguez-González, Eduardo Moreno-Piquero, and Francisco José Ares-Pena, 'Synthesis of Taylor-like patterns with uniformly excited multi-ring planar antennas,' *IEEE Transactions on Antennas and Propagation*, vol. 62, no. 4, pp. 1589-1595, Apr. 2014.

2. R. Eirey-Pérez, **A. A. Salas-Sánchez**, J. A. Rodríguez-González, and F. J. Ares-Pena, 'Pencil Beams and Flat-Topped Beams with Asymmetric Sidelobes from Circular Arrays,' *IEEE Antennas and Propagation Magazine*, vol. 56, no. 6, pp. 153-161, Dec. 2014.

3. M.J. Misa-Agustiño, J.M. Leiro-Vidal, J.L. Gomez-Amoza, M.T. Jorge-Mora, F.J. Jorge-Barreiro, **A.A. Salas-Sánchez**, F.J. Ares-Pena, E. López-Martín, 'EMF radiation at 2450 MHz triggers changes in the morphology and expression of heat shock proteins and glucocorticoid receptors in rat thymus,' *Life Sciences*, vol. 127, pp. 1-11, Feb. 2015.

4. **Aarón A. Salas-Sánchez**, Javier Fondevila-Gómez, Juan A. Rodríguez-González, and Francisco J. Ares-Pena, 'Measured characteristics of a planar array of parasitic elements fed by one active element,' *Microwave and Optical Technology Letters*, vol 57, no. 12, pp. 2807-2809, Dec. 2015.

5. Francisco J. Ares-Pena, Giorgio Franceschetti, Antonio Iodice, and **Aarón A. Salas-Sánchez**, 'Simple and effective monitoring of the electromagnetic field in the smart cities arena,' *Radio Science*, vol. 51, pp. 1249-1262, Aug. 2016.

6. Alberto López-Furelos, José Manuel Leiro-Vidal, **Aarón Ángel Salas-Sánchez**, Francisco José Ares-Pena and María Elena López-Martín, 'Evidence of cellular stress and caspase-3 resulting from a combined two-frequency signal in the cerebrum and cerebellum of Sprague-Dawley rats,' *Oncotarget*, vol. 7, no. 40, pp. 64674-64689, Aug. 2016.

7. **Aarón Ángel Salas-Sánchez**, María Elena López-Martín, Juan Antonio Rodríguez-González, and Francisco José Ares-Pena, 'Technique for determination of particulate matter pollution in the atmosphere using waveguide slot linear array antennas: a feasibility study,' *IEEE Geoscience and Remote Sensing Letters*, vol. 13, no. 10, pp. 1502-1506, Oct. 2016.

8. **A. A. Salas-Sánchez**, J. Fondevila-Gómez, J. A. Rodríguez-González, and F. J. Ares-Pena, 'Parametric synthesis of well-scanning isophoric pencil beams,' *IEEE Transactions on Antennas and Propagation*, vol. 65, no.3, pp. 1422-1427, Mar. 2017.

9. **Aarón Ángel Salas-Sánchez**, María Elena López-Martín, Juan Antonio Rodríguez-González, and Francisco José Ares-Pena, 'Design of Polyimide Coated Yagi-Uda Antennas for Monitoring the Relative Humidity Level,' *IEEE Geoscience and Remote Sensing Letters*, vol. 14, no. 6, pp. 961-963, Jun. 2017.

10. **Aarón Ángel Salas-Sánchez**, Juan Antonio Rodríguez-González, and Francisco José Ares-Pena, 'Parametric Synthesis of Isophoric Phase-Shaped Flat-Topped Beams,' Under Review for publication in the Journal *IEEE Transactions on Antennas and Propagation*.

11. Alberto López-Furelos, **Aarón Ángel Salas-Sánchez**, Francisco José Ares-Pena, Jose Manuel Leiro-Vidal, Elena López-Martín, 'Exposure to radiation from single or combined radio frequencies provokes macrophage dysfunction in the RAW 264.7 cell line,' Under Review for publication in *International Journal of Radiation Biology*.

A.2 Book Chapters

1. Elena López-Martín, **Aarón A. Salas-Sánchez**, Alberto López-Furelos, Francisco J. Jorge-Barreiro, Eduardo Moreno-Piquero, Francisco J. Ares-Pena (2017). Calculation of Dosimetry in Small Animals Combining the FDTD Method and Experimental Measures: Application for Three Radiation Systems. In Austin D. Russel (Ed.), *Radioactive Wastes and Exposure: Fundamentals, Management Strategies and Environmental Implications* (pp. 127-145), Hauppauge, NY: Nova Science Publishers.

A.3 Conference Proceedings

A.3.1 International

1. R. Eirey-Pérez, **A. A. Salas-Sánchez**, J. A. Rodríguez-González, E. Moreno-Piquero, and F. J. Ares-Pena, 'Pencil Beams and Flat-Topped Beams with Asymmetric Side Lobes from Circular Arrays,' in *The 8th European Conference on Antennas and Propagation (EuCAP 2014)*, The Hague, The Netherlands, 2014, pp. 3615-3619.

2. **A.A Salas-Sánchez**, J. Fondevila-Gómez, J. A. Rodríguez-González, E. Moreno-Piquero, F. J. Ares-Pena, 'Pencil and Shaped Beams Obtained by Planar Density Tapering,' in *The 8th European Conference on Antennas and Propagation (EuCAP 2014)*, The Hague, The Netherlands, 2014, pp. 3620-3624.

3. **A. A. Salas-Sánchez**, J. Fondevila-Gómez, J. A. Rodríguez-González, and F. J. Ares-Pena, 'Experimental Results of a Planar Array Composed by an Active Dipole above a Ground Plane with Parasitic Elements,' in *2015 9th European Conference on Antennas and Propagation (EuCAP)*, Lisbon, Portugal, 2015, pp. 1-3.

4. J. Fondevila-Gómez, **A. A. Salas-Sánchez**, J. A. Rodríguez-González, and F. J. Ares-Pena, 'Density-Tapered Planar Arrays for Multibeam and Shaped Beam Coverage in Satellite Communications,' in *2015 9th European Conference on Antennas and Propagation (EuCAP)*, Lisbon, Portugal, 2015, pp. 1-5.

5. **Aarón A. Salas-Sánchez**, Javier Fondevila-Gómez, Juan A. Rodríguez-González, and Francisco J. Ares-Pena, 'Optimization of the Directivity of Sum and Shaped Patterns using Circular Taylor and Ludwig Distributions,' *2015 1st URSI Atlantic Radio Science Conference (URSI AT-RASC)*, Gran Canaria, Spain, 2015.

6. **Aarón A. Salas-Sánchez**, Maria Elena López-Martín, Juan A. Rodríguez-González, and Francisco J. Ares-Pena, 'A Novel Method for Determination of Suspended Particulate Matter in the Atmosphere Using Array Antennas,' *2015 1st URSI Atlantic Radio Science Conference (URSI AT-RASC)*, Gran Canaria, Spain, 2015.

7. Alberto López-Furelos, José M. Leiro-Vidal, **Aarón A. Salas-Sánchez**, Juan A. Rodríguez-González, Francisco J. Ares-Pena, María E. López-Martín, 'Multiple Simultaneous Exposures to Electromagnetic Signals Induce Changes in Heat Shock Proteins and Caspase-3 on the Rat Brain Hemispheres,' *2015 1st URSI Atlantic Radio Science Conference (URSI AT-RASC)*, Gran Canaria, Spain, 2015.

8. Maria J Misa-Agustiño, Jose M Leiro-Vidal, Jose L Gomez-Amoza, Maria T Jorge-Mora, Francisco J Jorge-Barreiro, **Aarón A Salas-Sánchez**, Francisco J Ares-Pena, M. Elena López-Martin, 'Electromagnetic Field Radiation at 2450 MHz Induces Morphological and Expression Changes in Heat Shock Proteins and Glucocorticoid Receptors on the Rat Thymus,' *2015 1st URSI Atlantic Radio Science Conference (URSI AT-RASC)*, Gran Canaria, Spain, 2015.

A.3.2 National

1. L. López Vila, **A. A. Salas Sánchez**, J. A. Rodríguez González, F. J. Ares Pena, M. E. López Martín, E. Moreno Piquero, 'Análisis comparativo de SAR y estrés en animales pequeños en dos sistemas de radiación de onda viajera y de onda estacionaria a 900 MHz,' in *XXVIII Simposium Nacional de la Unión Científica Internacional de Radio*, Santiago de Compostela, 2013.

2. **A. A. Salas Sánchez**, J. A. Rodríguez González, E. Moreno Piquero, M. E. López Martín, F. J. Ares Pena, 'Estudio de viabilidad para la medición de la humedad relativa mediante antenas de dipolo con recubrimiento de poliimida,' in *XXVIII Simposium Nacional de la Unión Científica Internacional de Radio*, Santiago de Compostela, 2013.

3. **A. A. Salas Sánchez**, J. A. Rodríguez González, E. Moreno Piquero, F. J. Ares Pena, 'Síntesis de diagramas de tipo Taylor utilizando arrays planos con aros

concéntricos y alimentación uniforme' in *XXVIII Simposium Nacional de la Unión Científica Internacional de Radio*, Santiago de Compostela, 2013.

4. **A. A. Salas Sánchez**, F. J. Ares Pena, 'Contribuciones del profesor Eduardo Moreno Piquero en el ámbito de la docencia en Electromagnetismo,' in *XXVIII Simposium Nacional de la Unión Científica Internacional de Radio*, Santiago de Compostela, 2013.

5. A. López Furelos, J. M. Leiro Vidal, **A. A. Salas Sánchez**, J. A. Rodríguez González, F. J. Ares Pena, M. E. López Martín, 'Dosimetría y efectos biológicos en el cerebro de rata por exposición multifrecuencia en una cámara GTEM,' in *XXIX Simposium Nacional de la Unión Científica Internacional de Radio*, Valencia, 2014.

6. **A. A. Salas Sánchez**, J. Fondevila Gómez, J. A. Rodríguez González, F. J. Ares Pena, 'Resultados experimentales de un array plano de parásitos alimentado por un elemento activo,' in *XXIX Simposium Nacional de la Unión Científica Internacional de Radio*, Valencia, 2014.

7. E. López Martín, A. López Furelos, **A. A. Salas Sánchez**, E. Moreno Piquero, J. A. Rodríguez González, F. J. Ares Pena, 'Cálculo de la dosimetria en animales pequeños combinando el método de fdtd y medidas experimentales: aplicación para tres sistemas de radiación,' in *XXX Simposium Nacional de la Unión Científica Internacional de Radio*, Pamplona, 2015.

8. **Aarón A. Salas Sánchez**, Javier Fondevila Gómez, Juan A. Rodríguez González, Francisco J. Ares Pena, 'Síntesis de diagramas suma con un buen comportamiento en barrido de haz y de diagramas de haz conformado utilizando agrupaciones planas de antenas con excitación uniforme en amplitud.,' in *XXX Simposium Nacional de la Unión Científica Internacional de Radio*, Pamplona, 2015.

9. **Aarón Ángel Salas Sánchez**, María Elena López Martín, Juan Antonio Rodríguez González, Francisco José Ares Pena, 'Antena de guía de ondas ranurada para uso como medidor de concentración de polutantes en el ambiente: Estudio de viabilidad y optimización numérica,' in *XXXI Simposium Nacional de la Unión Científica Internacional de Radio*, Madrid, 2016.

10. **Aarón Ángel Salas Sánchez**, María Elena López Martín, Juan Antonio Rodríguez González, Francisco José Ares Pena, 'Diseño de antenas Yagi-Uda con recubrimiento de poliimida para la monitorización del nivel de humedad relativa,' in *XXXI Simposium Nacional de la Unión Científica Internacional de Radio*, Madrid, 2016.

11. Alberto López Furelos, José Manuel Leiro Vidal, **Aarón Ángel Salas Sánchez**, Juan Antonio Rodríguez González, Francisco José Ares Pena, María Elena López Martín, 'Validación del protocolo experimental de radiación para la línea celular RAW 264.7 con frecuencias combinadas en cámara GTEM,' in *XXXI Simposium Nacional de la Unión Científica Internacional de Radio*, Madrid, 2016.